Iron, Cobalt and Nickel-Based Metal Borides as Low-Cost Nanocatalysts for Highly Efficient Hydrolysis of Sodium Borohydride

by

Aybike PAKSOY

A Dissertation Submitted to the
Graduate School of Sciences and Engineering

in Partial Fulfillment of the Requirements for

the Degree of

Master of Science

in

Materials Science and Engineering

January 18, 2022

Iron, Cobalt and Nickel-Based Metal Borides as Low-Cost Nanocatalysts for Highly Efficient Hydrolysis of Sodium Borohydride

Koç University

Graduate School of Sciences and Engineering

This is to certify that I have examined this copy of a master's thesis by

Aybike PAKSOY

and have found that it is complete and satisfactory in all respects,

and that any and all revisions required by the final

examining committee have been made.

Committee Members:

Assoc. Prof. Özge BALCI ÇAĞIRAN (Advisor, Koç University)

Assoc. Prof. Uğur ÜNAL (Koç University)

Assoc. Prof. Duygu AĞAOĞULLARI (Istanbul Technical University)

Date: 18.01.2022

To my precious family…

ABSTRACT

Iron, Cobalt and Nickel-Based Metal Borides as Low-Cost Nanocatalysts for Highly Efficient Hydrolysis of Sodium Borohydride

Aybike PAKSOY

Master of Science in Materials Science and Engineering

January 2022

In today's world, fossil fuels, commonly known as non-renewable energy sources, provide 80 percent of the energy required. Toxic gases such as CO, SO_2, and NO_x are produced as a result of the combustion of these fuels. These gases have a wide range of harmful consequences for the environment and human health, particularly in terms of climate change. Environmentally friendly solutions are being researched to meet the energy needs. Hydrogen energy, in particular, has received a lot of interest in recent years. Hydrogen could be extracted from a variety of substances. In terms of high gravimetric hydrogen density, controllable reaction kinetics, non-toxicity, non-combustibility, and ease of storage in the open air, sodium borohydride ($NaBH_4$) is a good choice. However, the activation energy of the $NaBH_4$ hydrolysis reaction is 217 kJ/mol, which is a relatively high value. In order to reduce this activation energy value and to obtain hydrogen more effectively, the reaction should be carried out in the presence of a suitable catalyst. Although traditionally known noble metal catalysts such as platinum, iridium, rhodium, and ruthenium show excellent performance, alternatives should be developed due to their limited reserves and very high costs. Due to their high strength, high hardness, high chemical stability, magnetic qualities, and superior wear/corrosion resistance, transition metal borides can be used in a variety of applications. Transition metal borides, which are less expensive and durable, are emerging as a viable alternative catalyst.

In this thesis, among transition metal borides, iron, cobalt and nickel-based metal borides (Fe–Ni–B and Co–Ni–B systems) were chosen to investigate as promising catalysts for the hydrolysis reaction of $NaBH_4$. Catalyst powders with varied mole ratios were synthesized using a mechanochemical method (followed by a wet milling step) in the Fe–Ni–B system, while inorganic molten salt technique was used in the Co–Ni–B system. Utilized methods enabled to prepare the powders with nanoscale size and a uniform particle distribution, and pure composition. In the Fe–Ni–B system, the powder having Ni_3B and FeB semi-crystalline phases, homogenous shape, 70 nm particle size, and 41.8 m^2/g surface area displayed a remarkable catalytic performance in this direction. The availability of active iron, nickel and boron species on the surface was contributed to the enhancement of catalytic activity. It was able to produce 758 ml H_2 min^{-1} g_{cat}^{-1} of hydrogen at room temperature and reduce the activation energy of the reaction to 40.8 kJ/mol. In the Co–Ni–B system, the powder with CoB–Ni_4B_3 crystalline phases, which had a homogeneous morphology, approximately 60 nm particle size and pure content, exhibited an enhanced catalytic performance with a very low activation energy of the reaction of 32.7 kJ/mol. According to the recyclability tests, nanocatalyst powders in both systems exhibited catalytic activity even when used for 5 consecutive cycles. As-prepared catalysts that can compete with noble metals can be considered as recyclable, stable and low-cost materials for highly efficient hydrolysis of sodium borohydride.

ÖZETÇE

Yüksek Verimli bir Sodyum Borhidrür Hidrolizi için Ucuz Nanokatalizörler Olarak Demir, Kobalt ve Nikel Bazlı Metal Borürler

Aybike PAKSOY

Malzeme Bilimi ve Mühendisliği, Yüksek Lisans

Ocak 2022

Günümüz şartlarında ihtiyaç duyulan enerjinin %80'i yenilenemeyen enerji türü olarak da bildiğimiz fosil yakıtlardan elde edilmektedir. Bu yakıtların yanması sonucunda CO, SO_2 ve NO_x gibi toksik gazlar oluşmaktadır. Bu gazların başta iklim değişikliği olmak üzere çevre ve insan sağlığı üzerinde bir çok negatif etkileri bulunmaktadır. Enerji ihtiyacını karşılayabilmek için çevre dostu alternatifler araştırılmaktadır. Bunlar arasından hidrojen enerjisi son yıllarda özellikle dikkat çekmektedir. Hidrojenin elde edilebileceği birçok bileşik bulunmaktadır. Bunlar arasından sodyum borhidrür ($NaBH_4$) yüksek gravimetrik hidrojen yoğunluğu, kontrol edilebilir reaksiyon kinetiği, toksik olmaması, yanmaz ve açık havada muhafaza edilmesi kolay olması açısından iyi bir alternatif olarak görülmektedir. Ancak, $NaBH_4$ hidroliz tepkimesinin aktivasyon enerjisi 217 kJ/mol'dür ve görece yüksek bir değerdir. Bu aktivasyon enerjisi değerini düşürebilmek ve daha efektif bir şekilde hidrojen elde edebilmek için tepkime uygun bir katalizör eşliğinde gerçekleştirilmelidir. Geleneksel olarak bilinen platinyum, iridyum, rodyum, rutenyum gibi soymetal katalizörler mükemmel performans sergilese de kısıtlı rezervleri ve yüksek maliyetlerinden dolayı alternatifleri geliştirilmelidir. Geçiş metali borürler, yüksek mukavemet, yüksek sertlik değeri, yüksek kimyasal kararlılık, manyetizasyon özellikleri, iyi aşınma/korozyon dirençleri sayesinde birçok alanda kullanılabilmektedirler. Daha düşük maliyete sahip ve dayanıklı olan geçiş metali borürleri alternatif katalizörler olarak ön plana çıkmaktadırlar.

Bu tezde, geçiş metali borürler arasından demir, kobalt ve nikel bazlı metal borürler (Fe–Ni–B ve Co–Ni–B sistemleri) $NaBH_4$'ün hidroliz reaksiyonu için umut vaat eden katalizörler olarak araştırılmak için seçilmiştir. Fe–Ni–B sisteminde, mekanokimyasal yöntem (ardından ıslak öğütme aşaması) ile farklı mol oranlarına sahip katalizör tozlar sentezlenirken, Co–Ni–B sisteminde inorganik ergimiş tuz tekniği kullanılmıştır. Kullanılan yöntemler, nano ölçekli boyutta, homojen parçacık dağılımına ve saf bileşime sahip tozların hazırlanmasına olanak sağlamıştır. Fe–Ni–B sisteminde, Ni_3B ve FeB yarı kristalin fazlara, homojen şekle, 70 nm partikül boyutuna ve 41.8 m^2/g yüzey alnına sahip olan toz, dikkate değer bir katalitik performans sergilemiştir. Yüzeyde aktif demir, nikel ve bor türlerinin bulunması, katalitik aktivitenin artmasına katkıda bulunmuştur. Oda sıcaklığında 758 ml H_2 min^{-1} g_{cat}^{-1} hidrojen üretilebilmiş ve reaksiyonun aktivasyon enerjisi 40.8 kJ/mol'e indirilmiştir. Co–Ni–B sisteminde, homojen morfolojide, yaklaşık 60 nm partikül boyutuna ve saf içeriğe sahip CoB–Ni_4B_3 kristalin fazlı toz, reaksiyonun aktivasyon enerjisini 32.7 kJ/mol'e düşürerek gelişmiş bir katalitik performans sergilemiştir. Geri dönüştürülebilirlik testlerine göre, her iki sistemdeki nanokatalizör tozlar, 5 ardışık döngü için kullanıldıklarında bile katalitik aktivite sergilemiştir. Soy metallerle rekabet edebilen sentezlenmiş bu katalizörler, yüksek verimli bir $NaBH_4$ hidrolizi için geri dönüştürülebilir, kararlı ve düşük maliyetli malzemeler olarak kabul edilebilir.

ACKNOWLEDGEMENTS

First and foremost, I would like to express my gratitude to my advisor, Assoc. Prof. Özge Balcı, for her trust and encouragement. She not only guided me through my research with her patience and knowledge, but she also inspired me when I was discouraged and showed me the light at the end of the tunnel. Her investigative spirit motivated me and helped me realize what I wanted to do with my life. There are no words that can describe the value of having the chance to be her student. The first day we met and her warm welcome will stay with me always.

I also want to thank the members of my jury committee, Assoc. Prof. Uğur Ünal and Assoc. Prof. Duygu Ağaoğulları, for their valuable time. Your words of encouragement and insightful, comprehensive criticism have meant a lot to me.

I would also like to thank Asst. Prof. Umut Aydemir. He was always supportive whenever I needed help during my research and my lectures. I would like to thank Dr. Yeliz Utku Konca for not only helping me how to learn and teach professionally but also for always being understanding and motivating during my time as her assistant. I also would like to thank Dr. Barış Yağcı for taking care of all my SEM and XPS analysis, as well as for patiently handling my questions and confusions. I would like to thank Assoc. Prof. Alper Uzun, for his contributions, he increased my interest in my research field and enabled me to think in a wider window. I would like to especially thank dear Dr. Samira Fatma Kurtoğlu-Öztulum, for sharing her experience and knowledge in the field of catalyst with me, and for not turning me down whenever I asked for help.

I would like to thank all my colleagues in the KUBAM laboratory, which I am happy to be a part of, for always helping, supporting and creating a cheerful working environment when I needed it. I'd like to express my gratitude to my dear friend and colleague Dilara Arıbuğa by creating a special parenthesis here. She is one of the most motivating and helpful people I have ever met, and without her, I would not have been able to finish this thesis. Thank you for not only our work, but also for your invaluable friendship. During these tough 2 years, I had lots of laughter, countless good memories, some bad news, traces of tears, and you were by my side through it all. I feel very lucky that we have so much more to achieve together and that we will remain friends for life. I would like to open a parenthesis for my dear laboratory friend İlayda Terzi. I believe that

music has a unifying power and I am very happy to be able to share it with you. Thank you for understanding my feelings, my thoughts and expressing them with me through the songs. We won't rest until the world knows the name Isadore. My dear lab neighbour, classmate, friend Tuğba Yalçın, thank you for being a role model for me with your work discipline and determination. Your understanding, appreciation, help and support is very important to me. I am so lucky that we got to know each other.

A part of this thesis was supported by “The Scientific and Technological Research Council of Turkey (TUBITAK)” with the project name "Novel Low Temperature Synthesis of Cobalt–Metal–Boron (Metal=Ni, Fe, Ti) Based Ternary Metal Borides from Metal Chlorides: Characterization and Application Oriented Investigations on Catalyzer/Magnet/Hybrid Composite Fabrication" and number of 117F178. I would like to thank Graduate School of Sciences and Engineering and Koç University Surface Science and Technology Center (KUYTAM) for providing me support during my thesis studies.

My dear friends at ITU, you have perfected every moment of my life over my five years of university, and you have made your presence felt throughout my master's degree. Even though we are all on our own paths right now, I have walked every path I go with you. You're the ones that helped me fall in love with my job and encouraged me to continue on this path with a master's degree. I have no doubt that we will always find a way to get together and sing out loud.

Last but not least, my most sincere gratitude goes to my precious parents Handan & Ali Haydar Paksoy and my lovely brother Ayberk Paksoy. You have been by my side in every moment of my life and supported me to be myself. You made me feel proud in everything I did. Even in the most difficult times, you put my future above everything else. If I stated this thesis is truly yours, I don't think I'd be wrong. No words will cover the depth of having your unconditional love and support. Thank you, mom, dad and Ayberk, always. Mischief managed.

TABLE OF CONTENTS

LIST OF TABLES

LIST OF FIGURES

ABBREVIATIONS

E_a	Activation Energy
HGR	Hydrogen Generation Rate
CP	Commercially Available Powder
XRD	X-Ray Diffraction
XRF	X-Ray Fluorescence
FE-SEM	Field Emission Scanning Electron Microscopy
SEM	Scanning Electron Microscopy
EDX	Energy Dispersive X-Ray
BET	Brunauer–Emmett–Teller
DLS	Dynamic Light Scattering
XPS	X-Ray Photoelectron Spectroscopy

Chapter 1:
INTRODUCTION

Energy has become a necessary aspect of life, and the demand for it is growing by the day. Currently, fossil fuels have provided for 4/5 of global energy use [1]. When fossil fuels are burned for use, they release various gases such as nitrogen oxide (NO_x), sulfur oxide (SO_2), and carbon monoxide (CO) into the atmosphere. In addition to having harmful effects on human and environmental health, they also cause the formation of methane gas. All of these toxic gas emissions cause air pollution, water pollution, soil pollution, cardiovascular disorders, cancer, and climate change in society [2]–[4].

Research into alternative energy has improved as a result of both an increase in demand and the tangible effects of harmful consequences. These alternatives can be listed as wind, solar, nuclear, ocean, biofuels and hydrogen [5], [6]. Hydrogen can be obtained from many sources, including fossil fuels. When hydrogen energy is obtained from sources other than fossil fuels, then, we can argue that it is fully environmentally friendly. In addition, the fact that it can be obtained from a wide variety of sources is an advantage as it provides accessibility. Hydrogen can be obtained from many sources, including fossil fuels. However, it can be said that it is completely environmentally friendly for hydrogen energy when it is obtained from outside of fossil fuels. In addition, the fact that it can be obtained from a wide variety of sources is an advantage as it provides accessibility. It is a renewable energy type and does not emit harmful gases to the environment, it is possible to obtain it with many new methods developed, including electrochemical decomposition [7]. The most optimal and efficient production method is an important question that still awaits an answer. Despite these, the efficiency of hydrogen energy is one of the factors that makes it so attractive. The chemical energy per mass of hydrogen (142 MJ/kg) is nearly three times that of the liquid fuels we now utilize (47 MJ/kg) [8].

Hydrides, such as $LiBH_4$, $NaBH_4$, and KBH_4, have attracted attention in the search for an optimal hydrogen source. For a variety of reasons, $NaBH_4$ is regarded as one of the best options. In equation 1, the hydrolysis reaction of $NaBH_4$ is given [9].

$$NaBH_4 + 2H_2O \rightarrow NaBO_2 + 4H_2 + Q\ (217\frac{kj}{mol}) \qquad \textit{Eq. (1)}$$

According to this reaction, $NaBO_2$ is formed as a by-product besides hydrogen as a result of $NaBH_4$ hydrolysis. Since this $NaBO_2$ by-product is non-toxic and recyclable,

$NaBH_4$ can be specified as an environmentally friendly source [9]. $NaBH_4$ solutions are non-flammable and could be stored out in the open air for months. These features make it a secure option for transportation and usage [10]. In addition, when compared to other options, $NaBH_4$ has a gravimetric hydrogen density of 10.6 percent, which can be seen as the most crucial factor in its selection. Table 1.1 lists the features of various hydrogen storage materials. Although $LiBH_4$ has a higher capacity in terms of gravimetric hydrogen density, $NaBH_4$ takes the lead in preference because it is a more stable material [11].

Table 1.1 Physical properties of selected complex hydrides, adapted from [11]

Formula	***M (g mol^{-1})***	***ρ (g cm^{-3})***	***T_m (°C)***	***T_{dec} (°C)***	***x (mass%)***
$LiBH_4$	21.784	0.66	268	380	18.4
$NaBH_4$	37.83	1.074	505	400	10.6
$LiAlH_4$	37.95	0.917	>125	125	9.5
KBH_4	53.94	1.178	585	500	7.4
$NaAlH_4$	54.0	1.27	178	210	7.4
Mg_2NiH_4	111.3	2.72		280	3.6
Mg_2FeH_6	110.5	2.72		320	5.4
Mg_3MnH_7	134.9	2.30		280	5.2
$BaReH_9$	332.5	4.86		<100	2.7

Although, the activation energy of the $NaBH_4$ hydrolysis reaction stated in equation 1 is 217 kJ/mol, which is a high value to satisfy the supplied demand [12]. As a result, the usage of catalysts becomes an indispensable point. Catalysts are materials that accelerates the rate of a chemical reaction without consuming energy in the process [13]. It creates a new reaction pathway with a lower activation energy (E_a) value. Nonetheless, at the same temperature, the reaction rate of a catalyzed reaction is faster than that of an uncatalyzed reaction due to its lower E_a. Because a catalyst lowers the energy barrier, it enhances the rate of forward and reverse reactions by the same amount. Since the activity of a catalyst is directly related to the particle size and degree of dispersion, small particle size and well-dispersed catalysts may cause sufficient contact with the reagent; which is very important in enhancing the reaction rate and saving catalyst quantitatively [14], [15]. As a result, the relevance of producing nanocatalysts with the smallest possible particle size has grown, and research has focused to this area. Due to the limited availability and high cost of traditional catalysts such as Pt, Ir, Pd, Rh, and Ru, alternative catalysts are required [16]. These alternatives must be easily available and affordable, while still providing comparable performance to traditional catalysts. Transition metal boride materials have begun to be created and demonstrated as an alternative under these conditions. Boron, which has a wide range of applications due to its high temperature

resistance, high wear/corrosion resistance, high chemical stability and high hardness value, has also played a key role in the development of catalysts.

In this thesis, two different transition-metal boride nanocatalyst systems have been developed. The first few chapters will be about metal borides and catalysts in general, followed by a literature review on the effects of these catalysts on the hydrolysis reaction of $NaBH_4$. The following chapters will detail the experimental procedure and characterization methods. In the following section, the results and discussions will be explained in detail. As for the last part, the effects of the synthesized Co–Ni–B and Fe–Ni–B nanocatalyst materials on the $NaBH_4$ hydrolysis will be explained.

Chapter 2:
LITERATURE REVIEW

It is possible to claim that the transition metals history that we are familiar with is relatively old. Iron was used by the Egyptians approximately 5000 BC, despite not being classified as a "transition metal" [17]. Different synthesis processes have permitted the fabrication of improved and superior materials as technological and scientific advancements have increased. 'Transition-metal borides' are one of them. In 1835, the term "catalyst" was first used in the literature, and it quickly established a benchmark. These two ideas were the foundations of the energy field, and they drew greater attention throughout time [18].

2.1 Transition-Metal Borides

Any element in the d-block of the periodic table, which includes groups 3 to 12, can be described as a "transition metal." In fact, the lanthanide and actinide series of the f-block are also considered transition metals and are referred to as "inner transition metals" [19]. 'Transition-metal borides,' on the other hand, have risen in importance as a result of their several outstanding properties. By its particular properties, boron could create huge groups of phases with metals (M): semiborides (M_2B), monoborides (MB), diborides (MB_2), tetraborides (MB_4), hexaborides (MB_6), and dodecaborides (MB_{12}) [20]. High melting temperatures, high hardness values, high electrical and thermal conductivity, superior corrosion and wear resistance, and thermal shock resistance are the most remarkable qualities of metal borides. For the refractory transition metal borides, melting temperatures range from 2800 to 3250°C. The melting point of boron-rich metal borides is the highest. Hardness ratings for diborides range from 1100 to 2600, hexaborides from 1650 to 2100, and dodeca and hexaborides from 2300 to 2600 (Knoop Hardness - 0.1 kg) [21]. Metal borides have different conductivity qualities depending on their electrical properties. Metallic conductivity can be found in most borides, for instance TiB_2 and ZrB_2. The resistance to oxidation is provided by the oxide layer generated on the surface by boron and transition metal. Because of their strong covalent bonds, most transition metal borides have high melting temperatures, high hardness values, high strength, and chemical resistance [22], [23]. Furthermore, metal borides' magnetic

properties are very noteworthy. Because they only have magnetic characteristics when they are present in a compound [24]. The compound $Nd_2Fe_{14}B$ is the most important among them because it is the strongest magnetic material yet discovered [25], [26]. These superior properties have diversified the application areas of transition metal borides. Examples of these application areas are speakers, hard drives, electronics, aerospace technologies, NMR (Nuclear Magnetic Resonance) and MRI (Magnetic Resonance Imaging) devices, super magnets, semiconductors, superconductors, and refractory materials [27]–[31].

Transition-metal borides are also utilized as energy materials since they have a catalytic effect in addition to all of these properties. Noble metals such as platinum, rhodium, iridium, palladium, and ruthenium are encountered when introducing the catalyst issue. While these noble-metal-based catalysts provide high activity in all environments including acidic and alkaline environments, they can also maintain their chemical stability [16]. However, because these noble metals are prohibitively expensive, alternatives with comparable performance are sought. As a result, research into the use of more cost-effective transition metals as catalysts, such as cobalt, nickel, copper, manganese, and iron, has begun. The fact that certain metals are both catalytic and cost-effective lends credence to their employment as catalysts. The prices of these metals are compared in Figure 2.1 and 2.2. Generally, transition metal borides have the desirable attributes such as low synthesis cost, easy processing, and metal-like conductivity which makes them interesting materials [32]. In this thesis, synthesis, characterization and catalytic performance analysis were carried out on two different transition-metal boride systems such as Fe–Ni–B and Co–Ni–B.

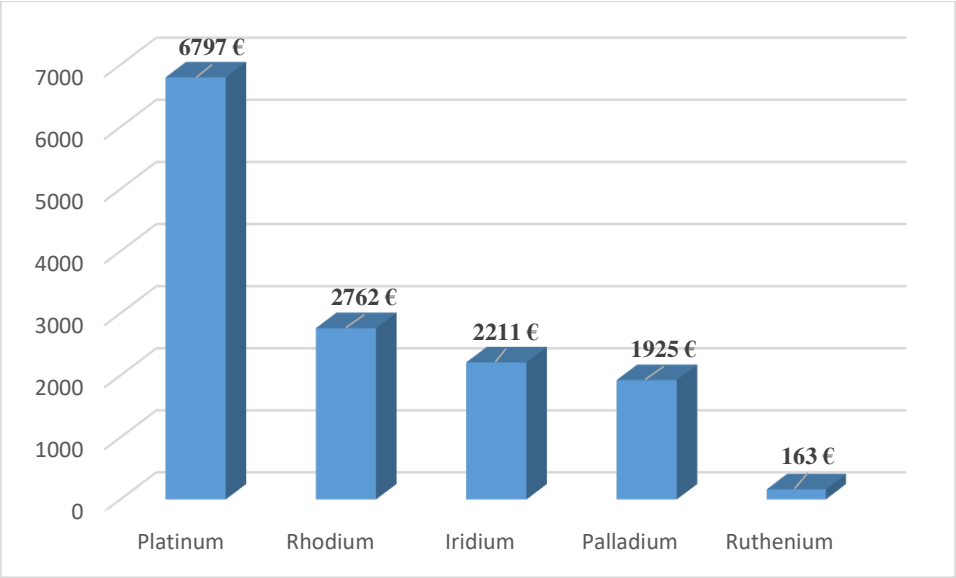

Figure 2.1 Selected noble metal prices (per mol), adapted from [33].

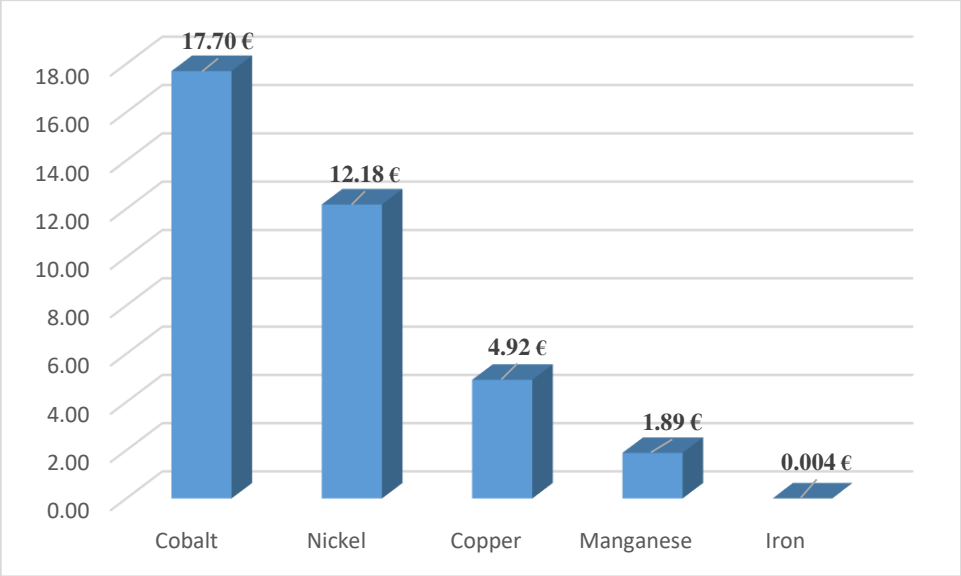

Figure 2.2 Selected transition metal prices (per mol), adapted from [33].

2.1.1 Fe–Ni–B System

Fe, Ni and B elements can form binary and ternary phases with various compositions like, FeB, Fe_2B, Ni_2B, Ni_3B, FeNiB, Fe_2NiB and $Fe_3Ni_3B_2$ (Appendix, Figure A.1-2) [34]–[36]. Magnetism, electrical conductivity, corrosion resistance, and high hardness are all common features of iron boride compounds [37]. Iron borides exhibit both ceramic and metallic material features, such as excellent hardness and thermal and electrical conductivity. For these characteristics, they have become prominent and commonly

utilized materials in a wide range of applications. Although various methods have been reported for the synthesis of Fe–B or Ni–B binary systems in the literature, research for the Fe–Ni–B ternary system is limited.

There are few studies in the literature on the iron- and nickel-containing borides which have been synthesized using different methods: Nie et al. first prepared 0.3 molar $NiCl_2$ and $FeCl_3$ solutions. Then, they formed a mixture by choosing different ratios for both solutions. They added $NaBH_4$ with a concentration of 0.2 molar to this mixture as a reducing agent and placed the flask containing the mixture in a water bath. They synthesized at low temperatures by preparing different water baths at 281K, 298 K, 323 K and 348 K temperatures. They determined the ratio between metal ion and reducer as 1:2. The formed ions such as Na^+, Cl^- were removed by washing with distilled water and the remaining powder was dried under vacuum. In this way, different Fe–Ni–B catalysts were obtained. To obtain the Ni–B binary phase, the same process was repeated without $FeCl_3$ solution [38].

Regmi et al. used $NiCl_2.6H_2O$ and $FeCl_3.6H_2O$, as starting materials. They obtained the FeNi alloy by heating the 0.3 molar solution they prepared at 75 °C. By adding $NaBH_4$ to the heated solution, they were able to utilise this chemical as a boron source. The suspension they obtained was purified from impurity ions by filtering and dried in a vacuum oven. Fe–Ni–B, Fe–B and Ni–B phases were synthesized by preparing solutions with different molarities [39].

Liang et al., on the other hand, used a two-stage synthesis technique to create the $NiB/NiFe_2O_4$ powder. They began by synthesizing the $NiFe_2O_4$ chemical. Nickel nitrate and ferric nitrate were dissolved in distilled water, followed by the addition of EDTA acid and citrate acid. They obtained a substance in gel form after entirely evaporating the water in the solution, and the resultant gel was then combusted in an electric stove to eliminate partial organic components. The red-brown $NiFe_2O_4$ ferrite particles were obtained by treating the gray powders in a muffle furnace at high temperature for 6 h. In the second step, after mixing the $NiCl_2.6H_2O$ solution and the $NiFe_2O_4$ powders they obtained, they were dried under vacuum. They used $NaBH_4$ as a boron source by immersing the dried powders in $NaBH_4$ solution and eventually switched to $NiB/ NiFe_2O_4$ powder [40]. It should be noted that the powders obtained in these studies have an amorphous structure and are in nanoscale sizes.

2.1.2 Co–Ni–B System

Co–Ni–B elements, like Fe–Ni–B elements, can form binary and ternary compounds with each other (Appendix, Figure A.3). When looking through the literature, it is clear that numerous methods have been used in the synthesis studies of Co–Ni–B systems. Fernandes et al. added $NaBH_4$ as the reducing agent to the aqueous solution consisting of $CoCl_2$ and $NiCl_2$, which they selected as the raw material. The resulting powder was separated from Cl^- and Na^+ ions by washing with distilled water and ethanol. All these processes were carried out at room temperature without giving extra heat. The washed powders were dried under nitrogen flow at 50 °C. They obtained different Co–Ni–B powders by changing the molar ratios of the precursors [15].

Zhao et al., on the other hand, utilized ultrasonic stirrer to mix the metal salts of $CoCl_2.6H_2O$ and $NiCl_2.6H_2O$ with $NaBH_4$ solution, which they selected as the starting material. Calcined the dry powders for 1 and 3 h at 400 and 450 °C, respectively, yielded powders with distinct phases [41].

Yi-Jing et al. produced solutions comprising $CoCl_2.6H_2O$ and $NiCl_2.6H_2O$ in various molar ratios in a similar manner. Instead of using $NaBH_4$, they employed KBH_4 as a reductant. KBH_4, like $NaBH_4$, serves as both a reducing agent and a boron supply in this case [42].

Instead of cobalt and nickel chloride compounds, Hu et al. selected the $Co(NO_3)_2.6H_2O$ and $Ni(NO_3)_2.6H_2O$ precursors. As a reducing agent and boron source, sodium borohydride was utilized. The impregnation-chemical reduction approach was used to prepare the catalysts. The powders were calcined at 200°C under a nitrogen environment after being washed with distilled water. This procedure was used to create a variety of powders [43].

Similarly, when examined the literature, it was reported that Li et al., Qiu et al., Wei et al., Bozkurt et al. synthesized various Co–Ni–B powders [44]–[47]. Here, it is important to state that the synthesized Co–Ni–B powders are in amorphous structure.

2.2 Catalysts

The first use of the term catalyst was proposed by Jöns Jakob Berzelius in 1835. Catalysts, as well as the established technologies, have a wide range of applications in various industrial areas, including chemistry, fuel, medicine, energy, and textiles. They were also awarded the Nobel Prize in 1909 and 1912 [48]. Catalysts enable reactions that

do not have enough reaction rates under present activation conditions while also increasing the pace of an existing reaction, which is why they are so appealing. Catalysts can be divided into homogeneous and heterogeneous. Heterogeneous catalysts contain more than one different phase, while homogeneous catalysts contain only one kind of phase [49], [50].

As stated in the introduction part, there is a global energy shortage. Obtaining hydrogen and using it as energy is one of the ideas offered as a solution to this problem. Catalysts play an essential role in this field because they lower the activation energy of the process in which they are used, shorten the reaction time, and improve the efficiency of the reaction. Many materials with a catalytic effect are currently being developed. Transition metals, in particular, perform admirably in reactions involving hydrogen and hydrocarbons [49].

One of the important reasons why catalysts increase the reaction efficiency is that they are placed in the reaction medium as small particles and increase the area of the surface where the reaction will take place. In this way, the activity on the surface will increase and the yield will increase. One of the popular methods used to increase this surface area is to disperse the catalyst on a suitable support material. Common support materials consist of refractory oxides such as SiO_2, Al_2O_3, or TiO_2 [51]. These materials exhibit high specific surface areas, high porosities, and high thermal and mechanical stability and come in a variety of pore sizes, while they are mostly chemically inert. Carbon is also widely used, while zeolites are often applied in many oil-refining and petrochemical applications [52]. However, another alternative to increase the surface area is to reduce the grain size of the material selected as the catalyst and thus to obtain a larger surface area. To have wider active surface area and the improved absorption ability in the catalyst, ternary phases could obtain with a second metal addition, which has made the metal–metal–boron systems to be more desirable in the catalytic field [53]. In this thesis, un-supported catalyst materials were examined and studies were carried out to develop them.

Safe storage and efficient release of hydrogen at ambient conditions remains a major obstacle for its widespread use. Recently, more efforts have been made to discover hydrogen storage materials. Among the hydrides, sodium borohydride ($NaBH_4$) stands out due to its high theoretical hydrogen content of 10.8 wt.%, nontoxicity, excellent stability of its solution at room temperature under high pH value and harmless product ($NaB(OH)_4$) of the hydrolysis reaction [54]–[56]. Regarding these properties, sodium

borohydride can be considered as a material that safely produces a significant amount of hydrogen when undergoing the hydrolysis reaction. High purity hydrogen can be controllably released from the hydrolysis of $NaBH_4$ alkaline solution in the presence of certain catalysts [10]–[12]. Due to their distinctive redox chemistries and catalytic activities, transition metal and metal oxide nanocrystals have previously been investigated as promising heterogeneous catalysts for enhancing $NaBH_4$ hydrolysis processes under basic medium [57]. Combining some transition metals (such as Fe, Co, or Ni) with metalloid atoms (such as P or B) modifies the intrinsic electronic states of transition metals, resulting in improved catalytic activity [58], [59]. For example, as can be determined from the studies of Zhao et al. and Liang et al, the use of catalysts consisting of Ni–B and Co–B particles, respectively, reduced the activation energy of the sodium borohydride hydrolysis reaction to 57.8 and 72.52 kJ/mol [14], [60]. As can be demonstrated from these values, the use of catalysts can decrease the activation energy by almost four-times. Therefore, the choice of catalyst is the key factor affecting the hydrogen production performance for the hydrolysis of $NaBH_4$. Traditionally known catalysts are noble metal catalysts such as Pt-, Ir-, Pd-, Rh-, and Ru-based ones. While these noble-metal-based catalysts provide high activity in all environments including acidic and alkaline environments, they can also maintain their chemical stability. However, they are very expensive due to their rarity which is a major disadvantage and that limits commercialization [16]. Recently, to obtain pure hydrogen, some non-noble metals and their alloys have been identified to catalyze the hydrolysis of $NaBH_4$. In this thesis, as mentioned before, iron, cobalt and nickel were examined among the transition metals.

There are studies in the literature on the use of non-supported binary and ternary metal boride compounds as catalysts in the hydrogen storage and fuel cell technology, thus the compounds were used to study catalytic performance for the hydrolysis of $NaBH_4$. Patel et al. were able to reduce the activation energy of the $NaBH_4$ hydrolysis reaction to 34 kJ/mol by using catalysts consisting of Co–Ni–B binary and ternary phases that they synthesized using cobalt chloride and nickel chloride solutions [15]. Xu et al., on the other hand, were able to decrease up to 55.7 kJ/mol with Co–Ni–B catalysts, which they synthesized from a mixture of cobalt nitrate, nickel nitrate and $NaBH_4$, and then made carbon support and obtained large surface area [43]. With an energy value of 57 kJ/mol, Nie et al. were able to perform the hydrolysis reaction with binary and ternary metal boride catalysts in the Fe–Ni–B system, which they synthesized from a mixture of

nickel chloride, iron chloride, and $NaBH_4$ with various molarities [38]. After examining the different studies reported in the literature, catalyst powders containing Fe, Co, Ni, and B were synthesized by unique production processes, characterized and measured their performances in the $NaBH_4$ hydrolysis reaction. The hydrogen generation rates (HGR) values and activation energies of $NaBH_4$ hydrolysis reactions with Fe, Co, Ni, B-containing catalysts reported in the literature are detailed in Table 2.1.

Table 2.1 Comparison of hydrogen generation rate (at room temperature) and activation energy of catalysts containing Fe, Co, Ni, and B that are reported in literature.

Catalyst Powder	**Hydrolysis Conditions**	**Hydrogen generation rate (ml H_2 min^{-1} g_{cat}^{-1})**	**Activation energy (kJ/mol)**	**References**
Ni–Fe–B	5 wt.% $NaBH_4$ 4 wt.% NaOH	2910	57.8	[38]
Ni	20 ml NaOH solution pH 9 0.5 g $NaBH_4$	255	69.7	[54]
Commercially Ni powder	20 ml solution: 1 wt% $NaBH_4$ 10 wt% NaOH	19.5	62.7	[61]
Raney Ni	100 ml solution: 1 wt% $NaBH_4$ 10 wt% NaOH	228.5	50.7	[61]
Ni_3B	15 ml solution: 10 wt% $NaBH_4$ 5 wt% NaOH	1298 (60°C)	-	[62]
$Ni_{73.6}B_{26.4}$	0.28 wt% $NaBH_4$ 0.04 wt% NaOH	-	64.9	[63]
$NiB/NiFe_2O_4$	50 ml solution: 0.5 wt% $NaBH_4$ 1 wt% NaOH	299.88	72.5	[40]
NiB	50 ml solution: 0.5 wt% $NaBH_4$ 1 wt% NaOH	146.14	-	[40]
Ni-B/Ni-foam	80 ml solution: 20 wt% $NaBH_4$ 5 wt% NaOH	130	61.8	[64]
Co–B	0.75 wt.% $NaBH_4$ 8 wt.% NaOH	1127	57.8	[14]
Co–B	0.01 wt.% $NaBH_4$ 0.01 wt.% NaOH	681	45.0	[15]
Ni–B	0.01 wt.% $NaBH_4$ 0.01 wt.% NaOH	100	-	[15]
Co(0.85)–Ni–B	0.01 wt.% $NaBH_4$ 0.01 wt.% NaOH	1175	34.0	[15]

Co–B nanoalloy	5 wt.% $NaBH_4$ 2 wt.% NaOH	7450	26.85	[65]
Co–B–O@Co_2B	1 wt.% $NaBH_4$ 5 wt.% NaOH	3850	29.3	[56]
Co–Ni–B	2.7 wt.% $NaBH_4$ 15 wt.% NaOH	2608	62.0	[66]
Co–Ni–B/Cu sheet	5 wt.% $NaBH_4$ 1 wt.% NaOH	14778	42.8	[47]
Co–B–10CNT	5 wt.% $NaBH_4$ 5 wt.% NaOH	12000	23.5	[55]

Chapter 3:
EXPERIMENTAL METHODS & CHARACTERIZATION

Catalyst powders in this study are synthesized through mechanochemical synthesis and inorganic molten salt techniques. In both techniques, anhydrous metal chloride and sodium borohydride mixtures were used as precursor to perform the reactions at room or low temperatures. Catalyst powders with varied mole ratios were synthesized using a mechanochemical method (followed by a wet milling step) in the Fe–Ni–B system, while inorganic molten salt technique was used in the Co–Ni–B system. The different systems will be investigated under two different headings in this chapter.

The catalytic performance of all the synthesized particles was investigated for hydrogen production from the $NaBH_4$ solution. The catalytic performance measurements were made by charging the $NaBH_4$ solution and catalysts into reactors, and then measuring the amount of hydrogen that is released over time. The hydrogen production rates of the catalysts were compared with each other and the effect of the structural factors affecting their catalytic performances were investigated. In the last heading, catalytic hydrolysis of $NaBH_4$ will be explained in this chapter.

3.1 Fe–Ni–B System

3.1.1 Materials

Starting materials for Fe–Ni–B catalyst powders and some of their related properties are listed in Table 3.1.

Table 3.1 Starting materials used in the Fe–Ni–B system.

Chemical Name	Formula	Physical State	Purity	Melting Point	Brand
Iron Chloride	$FeCl_3$	Powder	99.7 %	304 °C	Alfa Aesar
Nickel Chloride	$NiCl_2$	Powder	99 %	1009 °C	Alfa Aesar
Magnesium	Mg	Powder	99 %	648 °C	Alfa Aesar
Sodium Borohydride	$NaBH_4$	Powder	98 %	>300 °C	Alfa Aesar

3.1.2 Sample Preparation Method

Mechanochemical synthesis is a powder metallurgy technology that involves repeated cold welding, rupture, and re-welding in a high-energy ball mill to generate regulated and fine-structured composite powders [67]. Various Fe-Ni-B powders could be synthesized using this process without the requirement for additional heat from the outside [67]. For the synthesis of catalyst powders, the anhydrous iron chloride ($FeCl_3$, Alfa Aesar, 99.7 % purity) and nickel chloride ($NiCl_2$, Alfa Aesar, 99 % purity) powders as the metal chlorides and sodium borohydride ($NaBH_4$, Alfa Aesar, 98% purity) as the boron source and magnesium (Mg, Alfa Aesar, 99 % purity) powder as a reducing agent were used in the experiments. The theoretical reaction between $FeCl_3$, $NiCl_2$ and $NaBH_4$ results in Fe/Ni boride, $NaCl_{(s)}$ and $H_{2(g)}$ as reaction products. In addition, $MgCl_2$ by-product occurs, as Mg is added to the initial mixture. The powder mixtures were prepared according to the mole ratio of metal chlorides to $NaBH_4$ as 1:1 and 1:2. In case of using Mg reducing agent, the ratio of metal chlorides, $NaBH_4$ and Mg was used as 1:1:1 and 1:1:2, respectively. All the preparation and handling steps were carried out under Ar atmosphere in an MBraun™ glove box.

In order to obtain the desired microstructure, chemical composition, and particle size, the reactions were carried out via a mechanochemical route followed by a wet milling step. In the synthesis step, powder mixtures were mechanically milled for 1 or 2 h using a Spex™ 8000D high energy ball mill with a rate of 1200 rpm and a ball to powder ratio of 10:1. All the reactions were carried out at room temperature in one-step under mechanochemical conditions, no extra heating step was done. The as-synthesized powders were leached with hot distilled water using an ultrasonic bath for 15 min, for the elimination of NaCl and $MgCl_2$ by-products. The leached solution was then introduced to a Sigma centrifuge device for precipitation of the powders at 3500 rpm for a duration of 15 min. The obtained solution was dumped, and precipitated powder was extracted and dried overnight under vacuum at 80 °C. After mechanochemical synthesis and leaching, the purified powders were wet ball milled in ethanol (high purity, 99.99 %) for 1.5 hours using 1:10 ball to powder ratio. Wet ball milling enabled to distribute the agglomeration of the powders and obtain well-dispersed nanoparticles in the hydrolysis solution. Figure 3.1 shows the milling vial with stainless steel balls and the high energy ball milling device (Spex™ 8000D). Table 3.2 summarizes the synthesis conditions and their corresponding sample names for Fe–Ni–B catalysts. The flowchart of the synthesis process of the

catalysts is illustrated in Figure 3.2.

(a) **(b)**

Figure 3.1 (a) Milling vial with stainless steel balls and (b) high energy ball milling device.

Table 3.2 Synthesis conditions for the Fe–Ni–B based catalysts.

	Synthesis conditions		
Sample Name	**Starting powders**	**Ratio of powders(mmole)**	**Reaction Time**
A1@1	$FeCl_3$–$NiCl_2$–$NaBH_4$	1:1:1	1 h
A1@2	$FeCl_3$–$NiCl_2$–$NaBH_4$	1:1:1	2 h
A2@1	$FeCl_3$–$NiCl_2$–$NaBH_4$	1:1:2	1 h
A2@2	$FeCl_3$–$NiCl_2$–$NaBH_4$	1:1:2	2 h
A3@1	$FeCl_3$–$NiCl_2$–$NaBH_4$-Mg	1:1:1:2	1 h
A3@2	$FeCl_3$–$NiCl_2$–$NaBH_4$-Mg	1:1:1:2	2 h
A4@1	$FeCl_3$–$NiCl_2$–$NaBH_4$-Mg	1:1:1:1	1 h
A4@2	$FeCl_3$–$NiCl_2$–$NaBH_4$-Mg	1:1:1:1	2 h

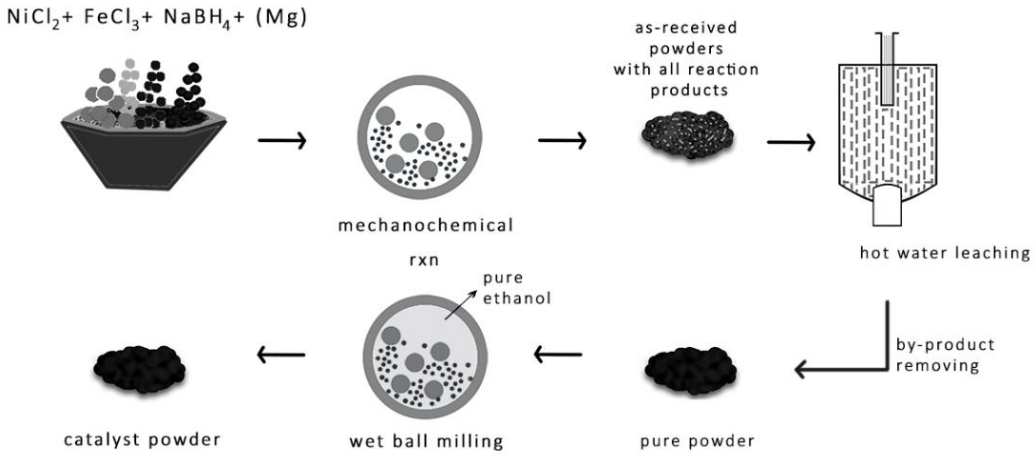

Figure 3.2 Flowchart of the synthesis process in the Fe–Ni–B system.

3.2 Co–Ni–B System

3.2.1 Materials

Starting materials for Co–Ni–B catalyst powders and some of their related properties are listed below in Table 3.3.

Table 3.3 Starting materials used in the Co–Ni–B system.

Chemical Name	**Formula**	**Physical State**	**Purity**	**Melting Point**	**Brand**
Cobalt Chloride	$CoCl_2$	Powder	99.7 %	724 °C	Alfa Aesar
Nickel Chloride	$NiCl_2$	Powder	99 %	1009 °C	Alfa Aesar
Sodium Borohydride	$NaBH_4$	Powder	98 %	>300 °C	Alfa Aesar
Lithium Chloride	LiCl	Powder	99 %	605 °C	Alfa Aesar
Potassium Chloride	KCl	Powder	99.5 %	773 °C	Merck

3.2.2 Sample Preparation Method

In order to synthesize the catalyst nanoparticles, the anhydrous cobalt chloride ($CoCl_2$) and nickel chloride ($NiCl_2$) powders as the metal chlorides and sodium borohydride ($NaBH_4$) as the boron source were used in the experiments. To induce the

reaction through the liquid phase and to avoid loss of products in the gaseous phase, the reaction was carried out in an inorganic molten salt medium. Thus, to carry out the reaction in liquid phase, the LiCl/KCl eutectic mixture (45:55 wt. %) was used as a water-soluble and low-melting-point inorganic salt solvent [67], [68].

The amounts of $CoCl_2$–$NiCl_2$–$NaBH_4$ mixtures were calculated based on the theoretical reaction between the precursors thereby accounting for the mole ratio of metal chlorides to $NaBH_4$ as 1:3 and 1:6, which results in $CoNiB_{x(s)}$, $NaCl_{(s)}$ and $H_{2(g)}$ as the reaction products, in order to prepare the ternary Co–Ni–B catalysts [69], [70]. Thus, 1 mole of $CoCl_2$ and $NiCl_2$ were added for a 1-gram ternary system, while $NaBH_4$ was added at ratios of 3 or 6 moles. For comparison purposes, the synthesis of binary borides was also studied by using the $CoCl_2$–$NaBH_4$ or $NiCl_2$–$NaBH_4$ mixtures based on a mole ratio of metal chlorides to $NaBH_4$ as 1:6. Thus, $CoCl_2$ or $NiCl_2$ was used at the ratio of 1 mole in a total sample of 1 gram, while $NaBH_4$ was added at the ratio of 6 moles.

The amount of the eutectic mixture was 10 times of the total amount of the precursor powders. All the preparation and handling steps were carried out under Ar atmosphere in an MBraun™ glove box. To obtain a homogenous mixture, the precursors were introduced to a short-time ball mill process, which was carried out for 3 min using a Retsch™ PM100 planetary ball mill with a rate of 600 rpm and a ball-to-powder weight ratio of 4:1. Only one set of the mixtures were mechanically alloyed (MA'd) for 2 min using a Spex™ 8000D high energy ball mill with a rate of 1200 rpm and ball-to-powder weight ratio of 4:1. Milling vials and balls made of stainless steel were used during the milling processes of precursors.

The mixtures were then introduced into a 316-L stainless steel tube and sealed via Ar welding. All the reactions were carried out under autogenic pressure in a sealed tube that was placed in a Protherm™ chamber furnace. The powders were heated up to 850 and 900°C, and then kept at that temperature for a duration of 2 h to obtain the nanocrystalline particles.

All the as-synthesized powders were leached with hot distilled water using an ultrasonic bath for 15 min, for the elimination of NaCl by-product and unreacted eutectic mixture. The leached solution was then introduced to a Sigma centrifuge device for precipitation of the powders at 3500 rpm for a duration of 15 min. The obtained solution was dumped, and precipitated powder was extracted and dried overnight under vacuum at 70 °C. Figure 3.3a shows the flowchart of the synthesis process in the Co–Ni–B system.

To indicate and summarize the research methodology, a flowchart of the general process used in the study is shown in Fig. 3.3b.

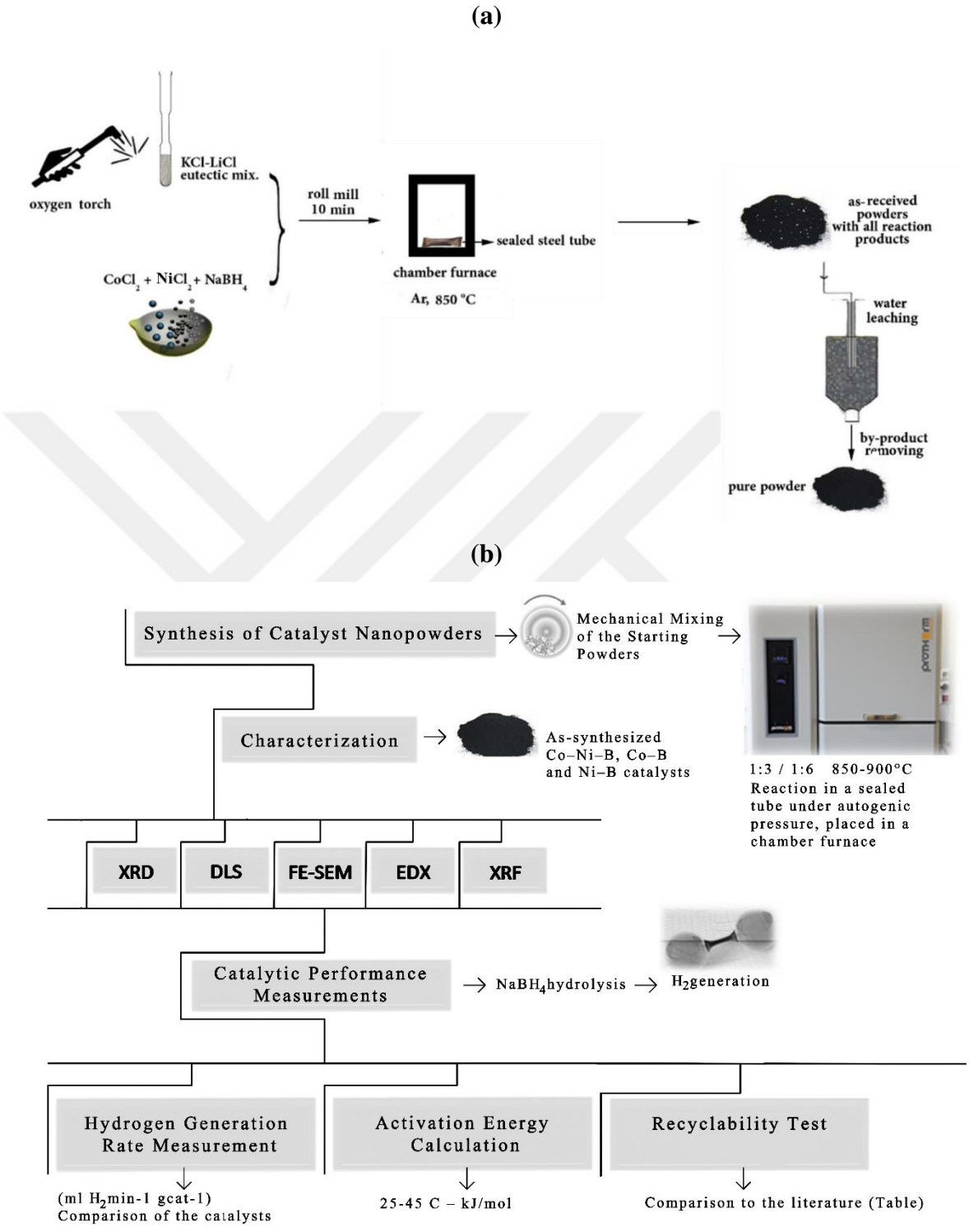

Figure 3.3 (a) Flowchart of the synthesis process and (b) general process for the Co–Ni–B, Co–B and Ni–B systems.

Table 3.4 summarizes the synthesis conditions and their corresponding sample names for Co–Ni–B catalysts. For comparison purposes, the commercially available cobalt boride powder (Co_2B–Co_3B, Alfa Aesar, 99 % purity) was also used as a catalyst, and is named as CP, as seen in Table 3.4.

Table 3.4 Synthesis conditions for Co–Ni–B, Co–B and Ni–B catalysts

Sample Name	Synthesis conditions		
	Starting powders	**Ratio of metal chlorides to $NaBH_4$ (mole)**	**Reaction Temperature (°C)**
S1@850	$CoCl_2$–$NiCl_2$–$NaBH_4$	1:3	850
S1@900	$CoCl_2$–$NiCl_2$–$NaBH_4$	1:3	900
S2@850	$CoCl_2$–$NiCl_2$–$NaBH_4$ (+2 mole of B)	1:3	850
S3@850	$CoCl_2$–$NiCl_2$–$NaBH_4$	1:6	850
S3@900	$CoCl_2$–$NiCl_2$–$NaBH_4$	1:6	900
S4@850	$CoCl_2$–$NiCl_2$–$NaBH_4$ (MA'd for 2 min)	1:6	850
S5@850	$CoCl_2$–$NaBH_4$	1:6	850
S6@850	$NiCl_2$–$NaBH_4$	1:6	850
CP	*Commercially available powder*		

3.3 Hydrolysis of $NaBH_4$

The experimental setup for hydrogen generation from $NaBH_4$ hydrolysis that was employed for catalytic performance measurements is shown in Figure 3.4. 5 mL of 0.2 M $NaBH_4$ solution containing 10 mmol NaOH was placed in a closed three-neck round bottom flask with an outlet tube for collecting the released hydrogen gas to conduct catalytic activity measurement experiment. As a result of the content, the solution used for $NaBH_4$ hydrolysis is a basic solution. As a stabilizer, this basic medium plays an important function in both extending the shelf life of H_2 and suppressing the self-hydrolysis of $NaBH_4$ [71], [72].

In the Fe-Ni-B system, since the synthesized catalyst powders have high magnetization, magnetic stirrer could not be used during the hydrolysis reaction. Therefore, before hydrolysis, the catalysts are wet milled so that they are dispersed in the solution. Powders were wet milled for 1.5 h using 1:10 ball to powder ratio and pure ethanol. The powders displayed excellent dispersion in the $NaBH_4$ solution as a result of

this procedure. An extra stirrer was not required due to the distribution. On the other hand, in the Co-Ni-B system, a hot plate magnetic stirrer was used to distribute the powders.

The flask was placed on a heater, and the flask's outlet pipe was inserted inside a water-filled burette, which was placed in a beaker filled with water with an upside-down position to capture the developed H_2 inside the burette (Figure 3.4). The $NaBH_4$ solution was placed into the flask, followed by 20 mg of catalyst, and the flask was immediately locked. It was verified that no H_2 was lost to the atmosphere because all catalysts required a short induction period. In order to control the temperature, the flask was placed in an oil bath and the temperature was observed with a thermometer as well. Equation 1 represents the reaction of $NaBH_4$ hydrolysis.

$$NaBH_4 + 2H_2O \rightarrow NaBO_2 + 4H_2 + Q\ (217\frac{kj}{mol}) \qquad Eq.\ (1)$$

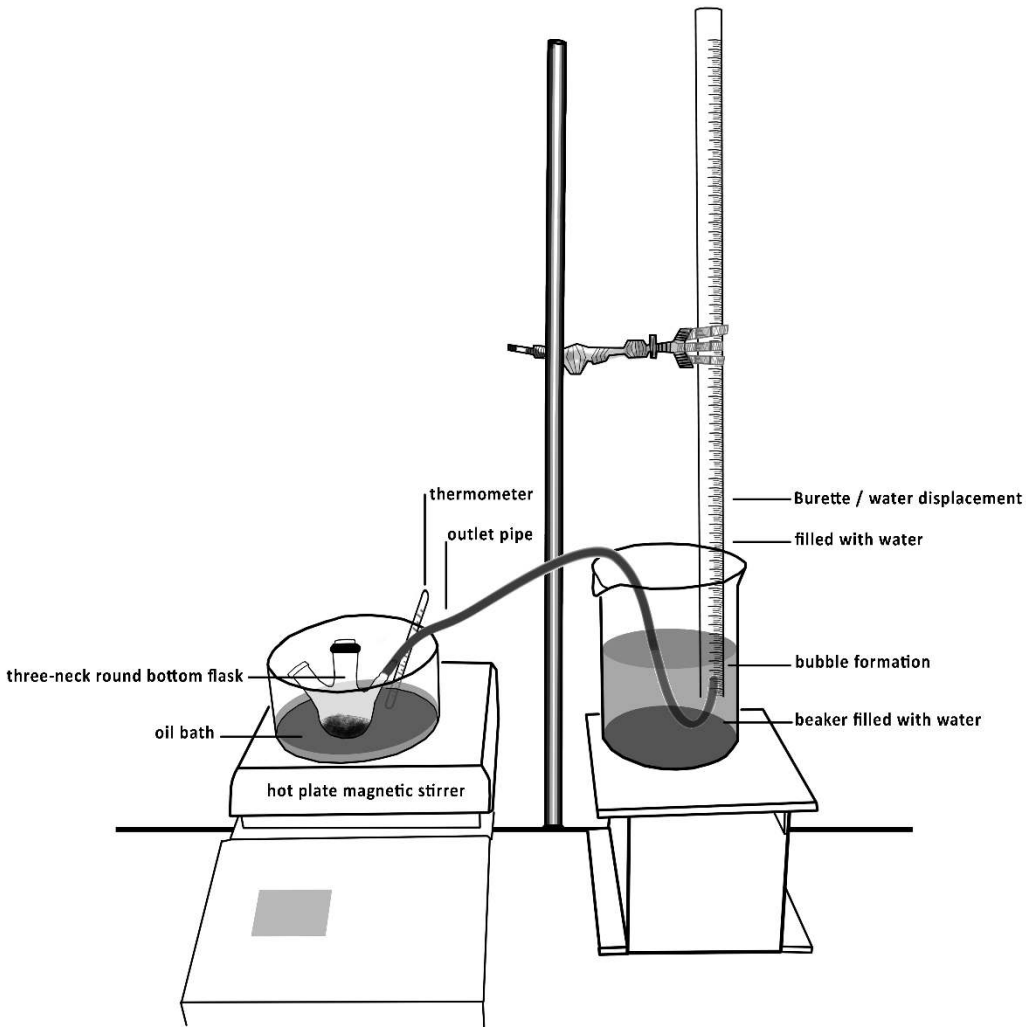

Figure 3.4 Experimental setup for hydrogen generation from the hydrolysis of $NaBH_4$.

The hydrolysis reaction was carried out at 25 °C for all catalyst particles. The linear part of the volume of produced H_2 versus reaction time graphs were used to calculate the specific hydrogen production rate (ml H_2 min^{-1} g_{cat}^{-1}) [73]. Hydrolysis at various temperatures (30, 35, 40, and 45 °C) was also accomplished, and the catalytic performance of the samples mentioned in results was investigated as temperature increased. For these catalysts, the Arrhenius plot was obtained, and the activation energy was determined. The Arrhenius equation is given in Eq. (2) [57].

$$\ln(k) = \ln(A)\,(\frac{-E_a}{RT}) \qquad \textit{Eq. (2)}$$

Here, k is the rate constant of the reaction, A is pre-exponential factor, E_a is the apparent activation energy (kJ/mol), R is molar gas constant (8.314 J/K/mol) and T is the reaction temperature (K). According to the kinetic studies in the literature, the hydrolysis reaction of $NaBH_4$ conforms to the zero-order kinetic model. In this thesis, the calculation of the activation energy values was carried out in accordance with the zero-order kinetic model [66], [74]–[76]. Firstly, the plot of the $NaBH_4$ concentration (mmol/ml) varying with time is drawn and the slope of this graph gives the k constant of the reaction. This process is done separately at room temperature, 30, 35, 40 and 45 °C. Then, a graph is obtained by using the exponential of these 5 different k values and the 1/T value of the corresponding temperature. Since the reaction kinetic model is zero-order, a linear curve is obtained. The value obtained by multiplying this curve with '-R' gives the new E_a value of the hydrolysis reaction [77].

The recyclability tests, were carried out at room temperature. First of all, 5 mL of 0.2 M standard $NaBH_4$ basic solution is prepared in which 20 mg of catalyst is used to obtain hydrogen. After making sure that $NaBH_4$ is completely consumed in the first hydrolysis reaction, the same amount of reactant ($NaBH_4$) is added. The addition of the same amount of $NaBH_4$ was continued until the same catalytic performance was measured (5th cycle).

3.4 Characterization Methods

3.4.1 X-ray Diffraction (XRD)

The primary instrument for determining the phases of a crystalline substance is X-ray diffraction (XRD). X-rays have wavelengths ranging from 0.2 to 10 nanometers. Because X-rays have dimensions corresponding to interplanar distances in crystals, X-ray crystallography is an effective non-destructive technique for material

characterization. In this thesis, phase analysis was conducted using a Rigaku™ Miniflex 600 Series X-ray diffractometer (XRD) with CuK_{α} radiation at a scan rate of 10°/min and a step size of 0.02°. XRF reduction mode of the device was conducted by changing the detector angle in order to reduce the fluorescence effects of Fe and Co. In the Co–Ni–B system, the International Center for Diffraction Data (ICDD) powder diffraction files were used to determine the crystalline phases. In the Fe–Ni–B system, the Crystallography Open Database (COD) powder diffraction files were used to determine the phases.

3.4.2 X-ray Fluorescence (XRF)

The emission of characteristic "secondary" (or fluorescent) X-rays from a material that has been accelerated by being attacked with high-energy X-rays or gamma rays is known as X-ray fluorescence (XRF). The phenomena is commonly applied in elemental and chemical analysis, especially in the study of metals, glass, and ceramics. [78], [79]. In this thesis, chemical analyses of the powders were conducted using a Bruker™ S8 TIGER X-ray fluorescence spectrometer (XRF), and the elemental composition up to ppm level (except elemental boron, which is not under limit of the device) was reported as wt. % of the total amount.

3.4.3 Field Emission Scanning Electron Microscopy (FE-SEM)

A scanning electron microscope (SEM) is an electron microscope that generates images by scanning the sample's surface with a focused electron beam. Electrons interact with the atoms in the sample to produce a variety of signals that provide information about the sample's topography and composition. The electron source, also known as an electron gun, the electron detector, the vacuum system, the condenser lenses, and the objective lenses, in general, are the essential components of a scanning electron microscope. To create a focused beam of electrons that impacts the sample's surface, electrons are first generated in an electron gun, accelerated down, and passed through a sequence of lenses and apertures. To decrease the detrimental effect of electron scattering in the air, the sample is put on a stand in the chamber area, and a combination of pumps are employed to empty both the column and the chamber. Based on the electron-sample

interaction, several signals are acquired. Detectors are then employed to keep track of these signals [80]–[82].

Field emission scanning electron microscopy (FE-SEM) is used analyze topographical details of a sample at a wide range of magnification (10X to 300.000X). In this thesis, the microstructures were investigated using a Zeiss™ Ultra Plus Field Emission Scanning Electron Microscope (FE-SEM); and the secondary electron detector was used to obtain the images (at 5 and 12 kV of acceleration voltages) by setting the working distance at about 5.0-5.9 mm. Bruker XFlash 5010 Energy Dispersive X-Ray Spectrometer (EDS) detector with 123 eV resolution was used for EDX analysis to obtain the elemental mapping of the samples on the selected area. Average particle sizes were calculated from the FE-SEM images taken at different magnifications: The result of each sample represents the arithmetic mean of twenty measurements of particle sizes and its standard deviation.

3.4.4 Brunauer–Emmett–Teller (BET)

The Brunauer–Emmett–Teller (BET) theory attempts to explain the physical adsorption of gas molecules on a solid surface and serves as the foundation for a critical analysis technique for calculating the specific surface area of materials. BET theory is used to determine specific surface area in multilayer adsorption systems that use a probing gas (called the adsorbate) that does not react chemically with the adsorptive (the material on which the gas connects and the gas phase is termed the adsorptive). The most often used gaseous adsorbate for probing surfaces is nitrogen (s). As a result, routine BET analysis is frequently performed at N_2 boiling temperature (77 K). In this thesis, the surface areas were investigating using a Micrometrics Gemini VII BET device, and the unit of the measurement is m^2/g for each sample.

3.4.5 Dynamic Light Scattering (DLS)

Dynamic Light Scattering (DLS) is a useful instrument for determining the properties of nanoparticles and other colloidal solutions. The light scattered from a laser passing through a colloidal solution is measured using DLS. The size of the particle in solution can be determined by examining the modulation of scattered light intensity as a function of time. The intensity and fluctuation of light scattered from nanoparticles in dilute solution are measured using DLS. The intensity of scattered light varies depending on

particle velocity, size, medium viscosity, temperature, and other parameters such as salinity. In terms of the typical properties of nanoparticles in liquid media, DLS analyses are critical [82]. In this thesis, particle size distribution graphs were obtained by using a Malvern™ Zetasizer Dynamic Light Scattering (DLS).

3.4.6 X-Ray Photoelectron Spectroscopy (XPS)

The most widely used surface analysis technique is X-ray photoelectron spectroscopy (XPS). XPS is based on energy distribution measurements of photon-excited electrons from atoms in the solid's surface region. With a sensitivity that changes by only a factor of ~ 30 across the periodic table, it can detect all elements except hydrogen. Depending on the element, the ab- solute sensitivity ranges from ~ 0.01 to 0.3 at %. The electron-binding energies are proportional to the atom's chemical state, and this is utilized to determine the atom's chemical state [83]. Thus, it provides information regarding the chemical state, elemental composition, and the electronic structure and density of the sample surface. [84]. In this thesis, the surface chemical structures of the samples were investigated by using a Thermo Scientific K-Alpha X-Ray Photoelectron Spectrometer (XPS) with an aluminum anode (Al Kα =1468.3 eV). The chamber pressure was below 5×10^{-8} mbar during the measurements. The raw data was fitted using the Thermo Avantage v5.973 software package.

Chapter 4:
RESULTS AND DISCUSSION

In this section, the outputs of the synthesized Fe–Ni–B system and Co–Ni–B system will be presented in two separate sections.

4.1 Fe–Ni–B System

4.1.1 Phase and Chemical Analysis of the Synthesized Catalysts

Figures 4.1, 4.2, and 4.3 show the XRD patterns of the synthesized catalysts. The used synthesis method enabled the simultaneous formation of the binary compounds via a one-step reaction of $FeCl_3$–$NiCl_2$–$NaBH_4$ mixture with or without Mg powder. According to the changing synthesis parameters, different compositions of the metal boride composites were formed. It is clearly seen that starting materials and reaction time directly affected the phases formed at the end of the synthesis. The formation of Ni_2B metal boride phase as well as dominant NiO phase was seen in the A1@1 and A1@2 samples showed in Figure 4.1. Since $NaBH_4$ is used here both as a reducing agent and as a boron source, it was insufficient to be used in the synthesis at a 1 molar ratio for the formation of boride phases, which are desired. Same crystalline phases was observed after ball milling for both 1 and 2 h, and it was determined that small amount of Fe remained in the metallic phase.

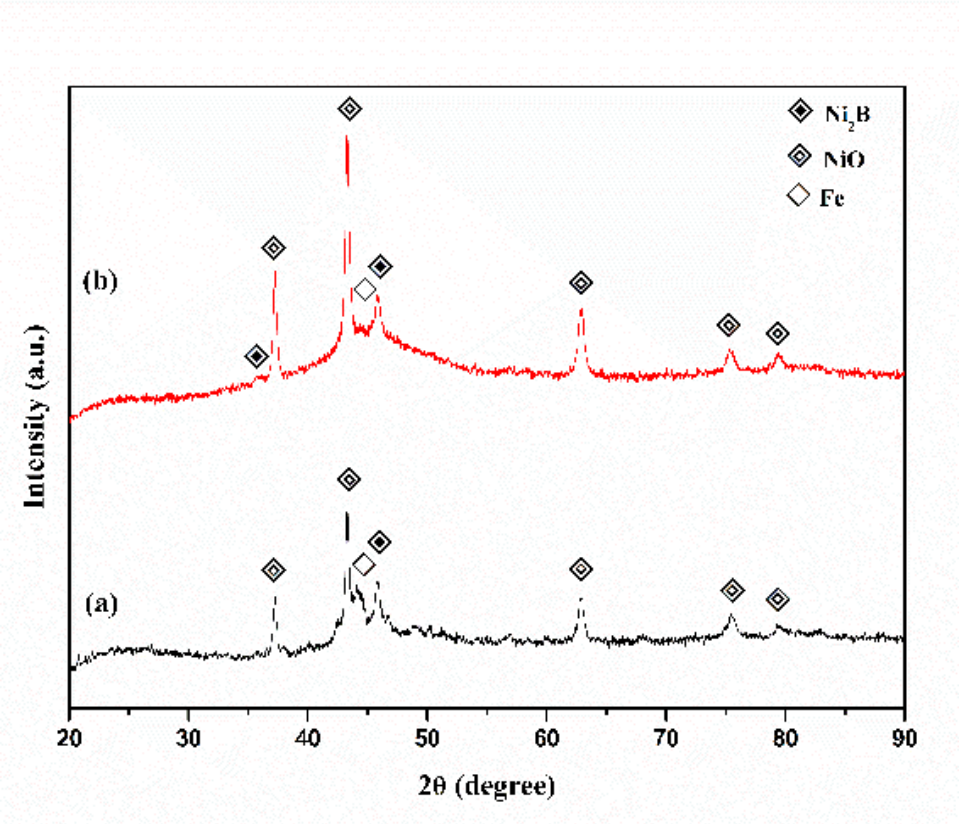

Figure 4.1 XRD patterns of the synthesized catalysts: (a) A1@1, (b) A1@2.

In this situation, two different options were evaluated. Firstly, it is aimed to double the mole ratio of $NaBH_4$ and react with minor amounts of oxygen and chlorine in the medium, and then remove it from the final powder by water leaching. As a result, high purity powders in semi-crystalline structure containing Ni_3B and FeB phases were obtained together. There is no oxygen impurity in the A2@1 and A2@2 samples, as shown in Figure 4.2.

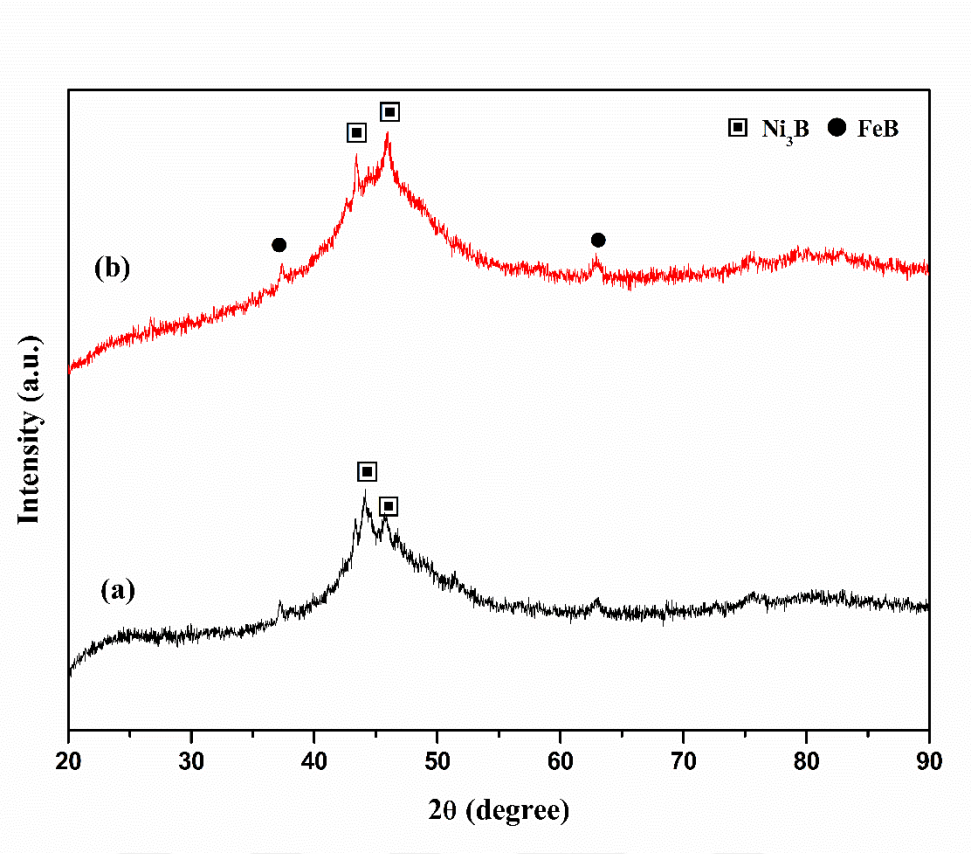

Figure 4.2 XRD patterns of the synthesized catalysts: (a) A2@1, (b) A2@2.

Secondly, Mg powder was added to the system. In this way, it is aimed to use $NaBH_4$ as a boron source and to use magnesium as a reducing agent. Under these synthesis conditions, the minor oxygen in the system reacted with magnesium and eventually formed the MgO phase. In order to remove this phase, which cannot be removed by water leaching, acid leaching was performed with HCl solutions at different concentrations. In this way, it is aimed to obtain the desired pure catalyst powder. However, acid leaching at low concentrations was ineffective in removing MgO, while the boride phases were separated as the concentration is raised. The XRD graphs of A3@1 and A3@2 samples to which Mg powder was added as reducing agent are given in Figure 4.3. The powders contain the Fe_3B and Ni_4B_3 phases with the presence of MgO impurity.

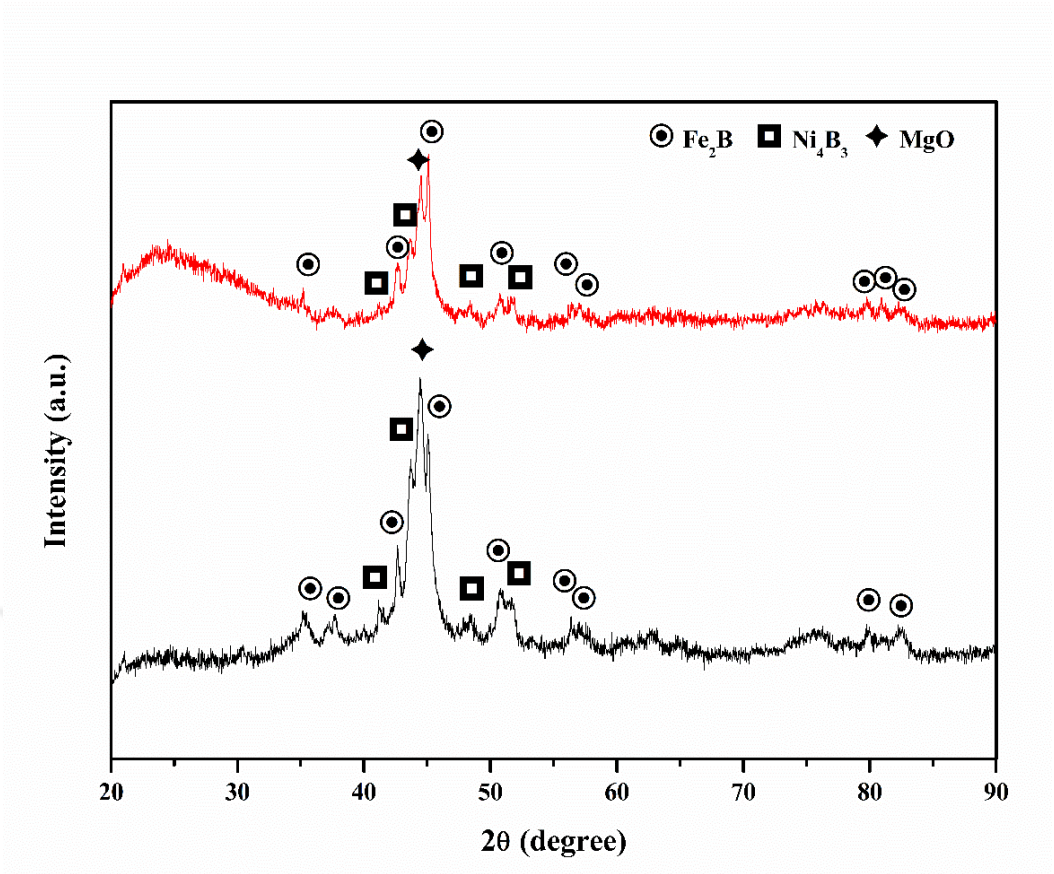

Figure 4.3 XRD patterns of the synthesized catalysts: (a) A3@1, (b) A3@2.

In order to eliminate the formed MgO phase, the samples were synthesized by reducing the amount of added Mg powder to half. XRD analyses of these powders are given in Figure 4.4. Nevertheless, the amount of Mg powder was insufficient and the reaction could not be completed. Accordingly, as provided in Figure 4.4, it is seen that $B_2MgNi_{6.7}$ phase and Fe_2B phase with magnesium, boron and nickel are formed in the A4@1 and A4@2 samples. It can be interpreted that the phases with reacting magnesium are more dominant and therefore no catalytic activity is observed (will be discussed in the *"4.1.4 Catalytic Performance Measurements"* part). In Appendix, Table A.1 presents the COD Card information for all the obtained phases, while Table A.2 shows the indices for the corresponding diffraction peaks of the all obtained phases.

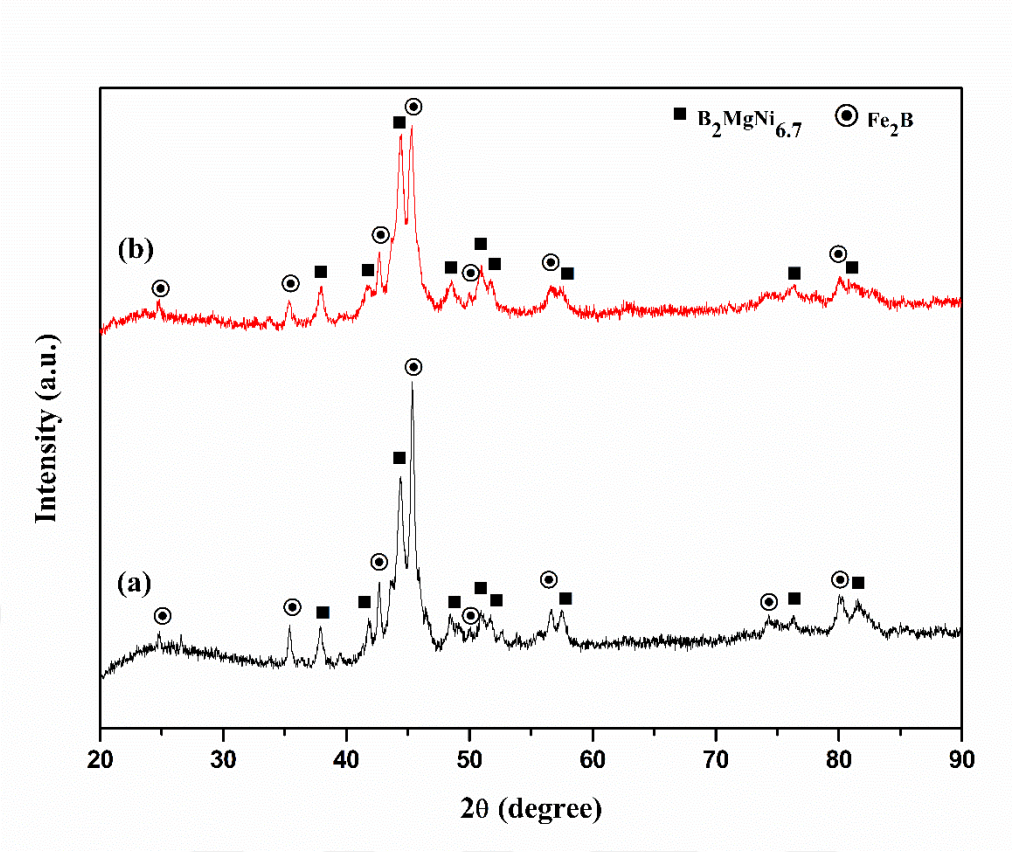

Figure 4.4 XRD patterns of the synthesized catalysts: (a) A4@1, (b) A4@2.

4.1.2 Microstructure Analysis of the Synthesized Catalysts

SEM images of the synthesized catalyst powders are given in Figure 4.5. The particles have a spherical-like morphology, and their synthesis via a mechanochemical route followed by wet milling has an effect on this. This mechanism also adds to particle distribution homogeneity. When the results of the SEM images are reviewed, it is discovered that the average particle size of the A1@1, A1@2, A2@1, and A2@2 samples are between in the range of 40 and 100 nm. When looking at the images in general, it can be seen that the particles of A1@1 and A2@1 powders synthesized with 1 h of milling are more agglomerated, and this agglomeration decreases in the A1@2 and A2@2 powders with a milling of 2 h. When looking at the A1@2, A2@1 and A2@2 samples, it is clear that they present a more uniform morphology compared to other samples and have the smallest particle size among them. This result in the A2@1 and A2@2 samples was attributable to the powders' pure composition, which contain the Ni_3B and FeB phases without any oxide or impurity phase (Figure 4.2). The presence of oxidized phases and

impurities makes particle size reduction difficult and prevents the formation of a uniform morphology. Despite the existing Fe impurity phase in the structure of the A1@2 sample (Figure 4.1), it also presents a homogeneous distribution of the particles, most likely due to the positive effect of 2 h of milling time. According to the SEM analyses, the average particle sizes of the A2@1 and A2@2 samples are calculated as 70 and 60 nm, respectively. On the other hand, it can be seen from the images of the A3@1 and A3@2 catalysts with magnesium impurity that larger particles form and they migrate away from the spherical-like and uniform morphology. The SEM images of the A4@2 sample, which was mentioned earlier in the XRD section, that catalytic activity was not observed and pattern graph was given in the Figure 4.4, are also shown in Figure 4.6. Large particle size and heterogeneous structure were determined in these images.

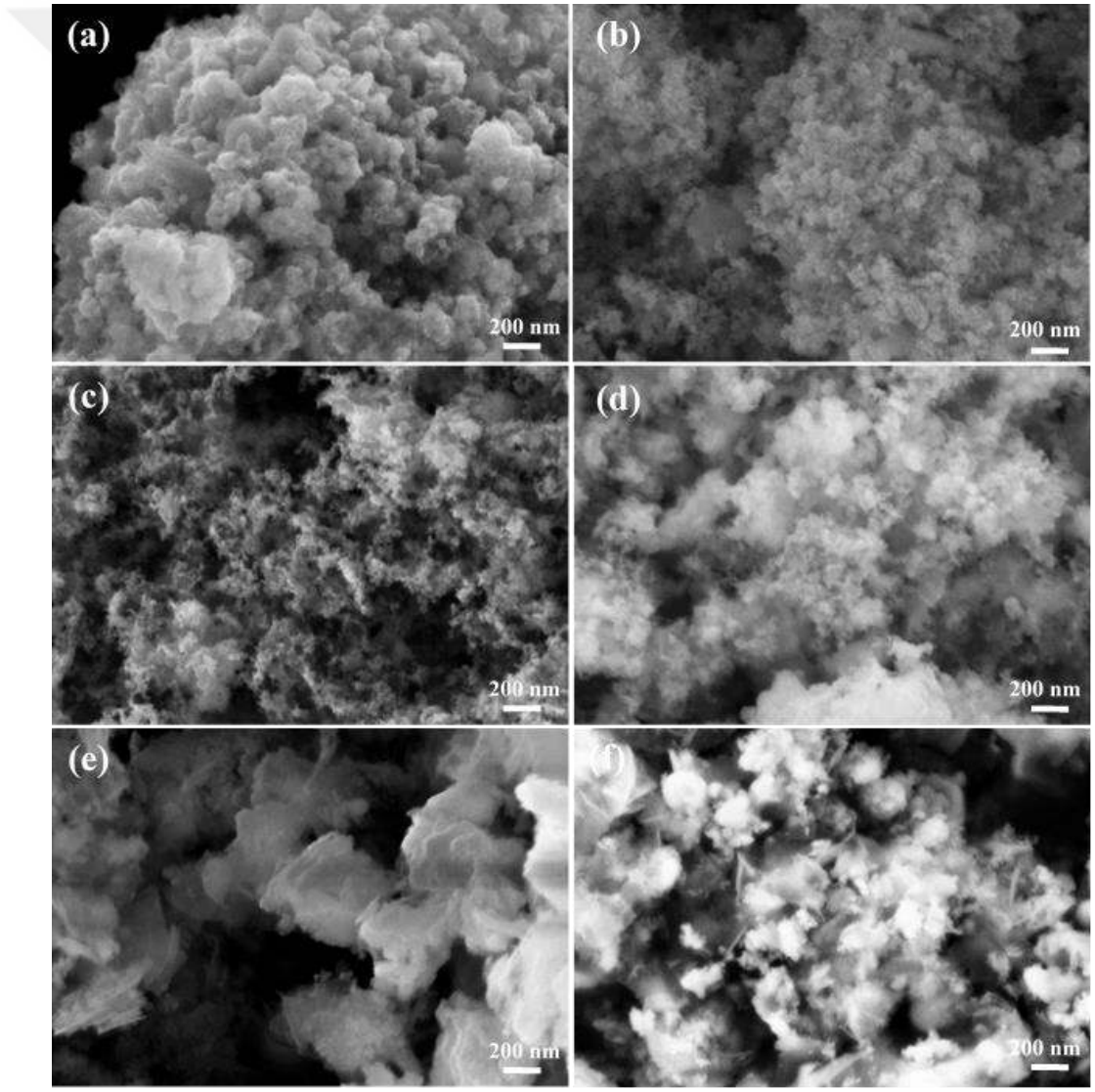

Figure 4.5 SEM images of the synthesized catalysts: (a) A1@1, (b) A1@2, (c) A2@1, (d) A2@2, (e) A3@1 and (f) A3@2.

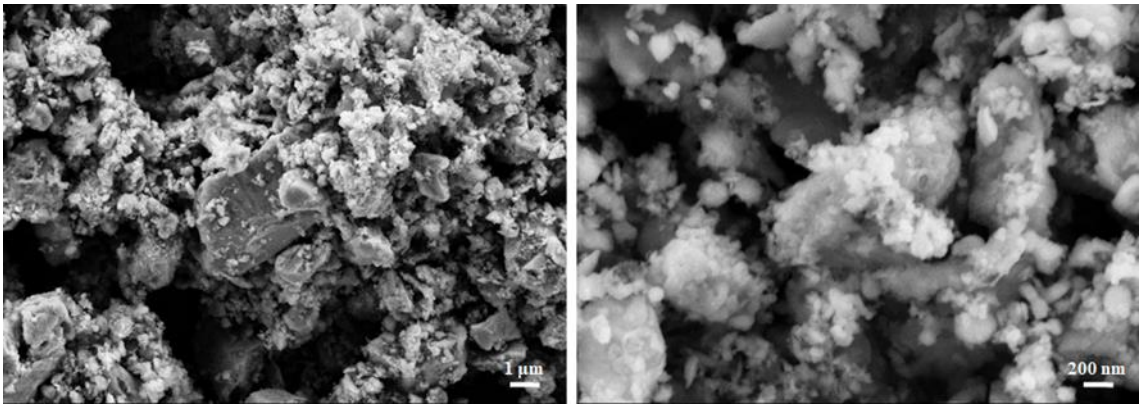

Figure 4.6 SEM images of the synthesized catalysts A4@2.

Figure 4.7, 4.8 and 4.9 show the SEM-EDX analyses of the powders. Figure 4.7 shows the homogeneous distribution of iron, nickel, and boron elements in the selected sample of A2@1. The elements Fe and Ni maps are completely consistent with the elemental B map, indicating the existence of iron and nickel boride phases, which were also discovered by XRD investigation (Figure 4.2). The suppression effect of the other strong signals of the Fe and Ni elements can be linked to the weak signals of B element in all analytical results. Furthermore, no other element signals were discovered during the EDX studies, demonstrating the high-purity of the catalyst powders. The mapping results for the A1@1 catalyst are presented in Figure 4.8, so that the outcome of expression in varied molar ratios could be seen more clearly. Figure 4.9 shows the SEM-EDX analysis of the A3@2 sample, which revealed the existence of MgO impurity in the XRD analysis (Figure 4.3). The strong signals of the Mg and O elements in the same area indicate the existence of a particle consisted of MgO phase, which is shown by a circle in the SEM image in Figure 4.9. In addition to the heterogeneous structure observed in the SEM image in Figure 4.5, iron and nickel elements do not have a fine distribution in the SEM-EDX analysis in Figure 4.9. When comparing the A3@2 sample to the A2@1 and A2@2 samples, the homogenous structure of the A2@1 and A2@2 samples can be clearly seen.

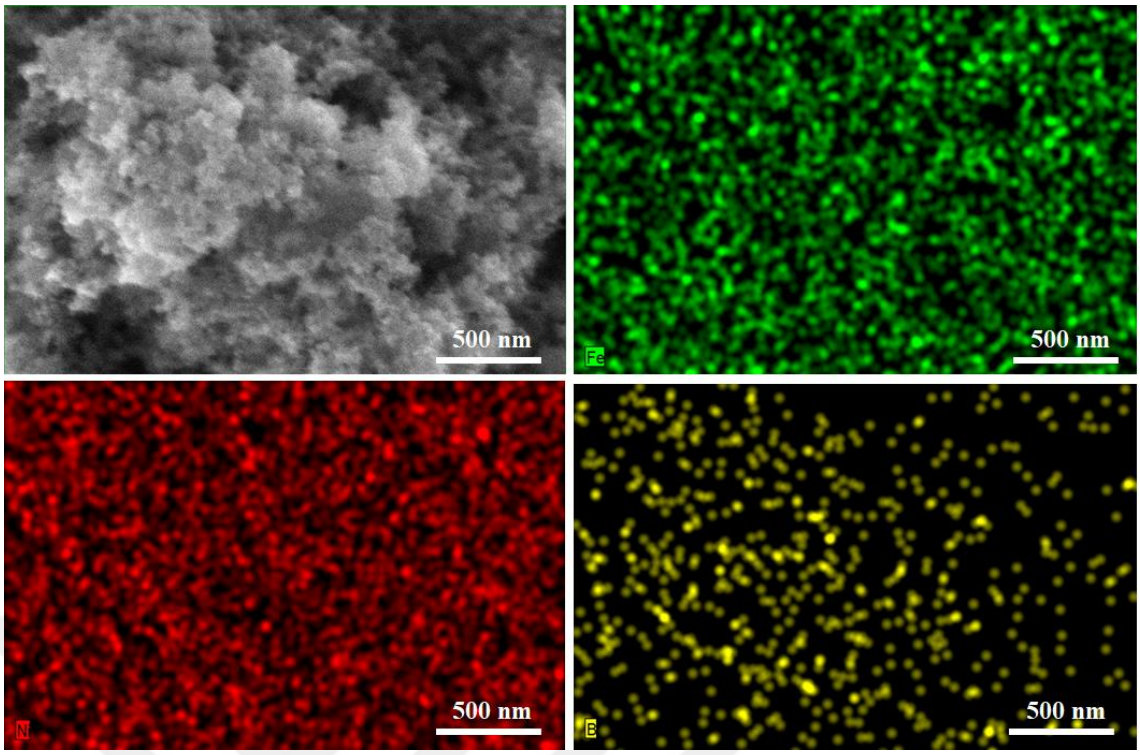

Figure 4.7 SEM images of sample A2@1, EDX mapping of Fe, Ni and B in sample A2@1.

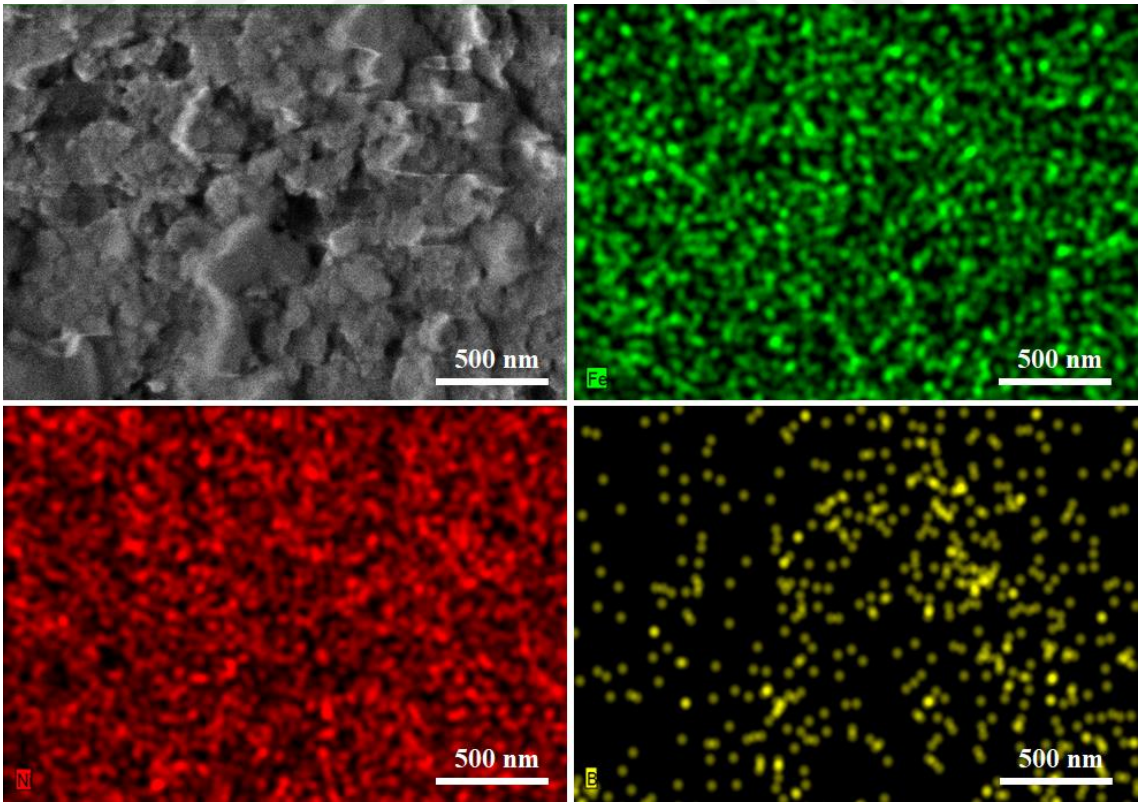

Figure 4.8 SEM images of sample A1@1, EDX mapping of Fe, Ni and B in sample A1@1.

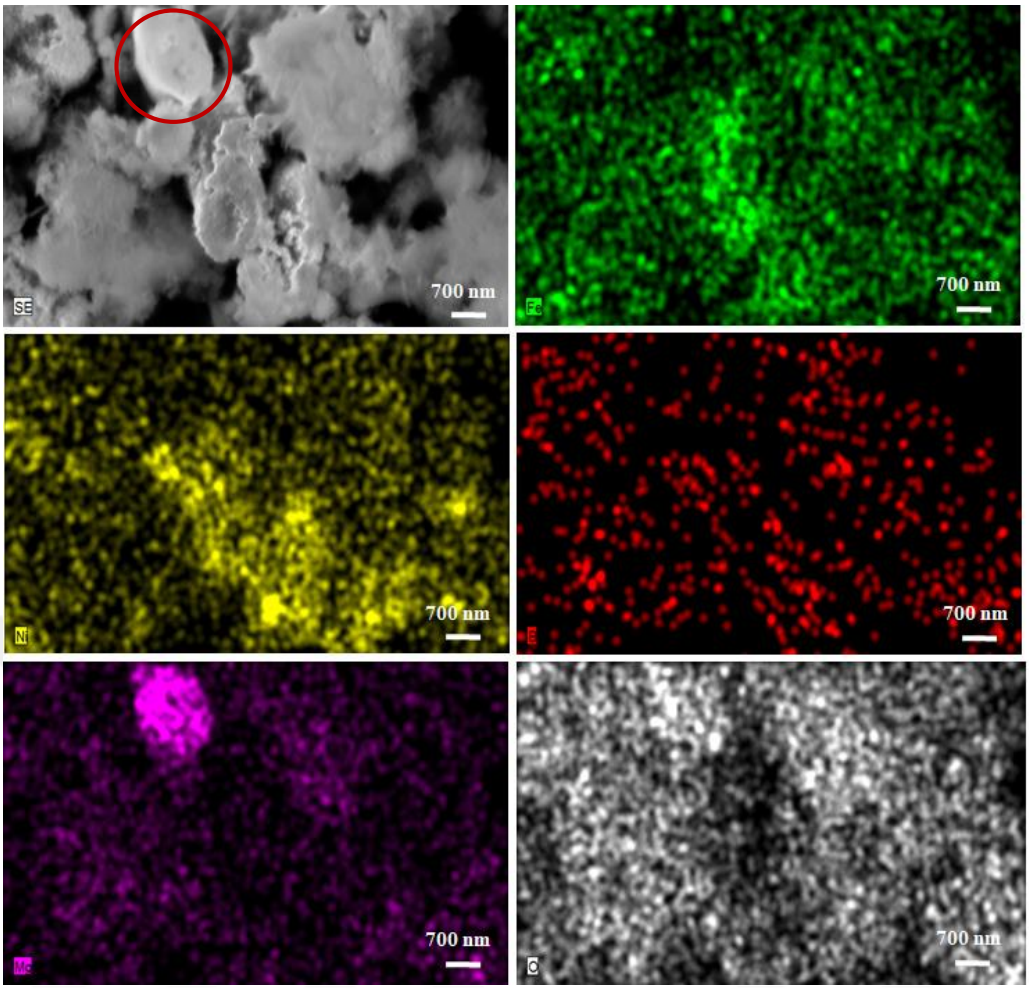

Figure 4.9 SEM image of sample A3@2, EDX mapping of Fe, Ni, B, Mg and O in sample A3@2.

BET surface area measurements were done on the selected samples. A1@1, A1@2, A2@1, A2@2, A3@1, and A3@2 powders exhibited surface area values of 24.85, 30.48, 41.80, 46.38, 35.88, and 37.35 m^2/g, respectively. Based on these data, it is noticed that the surface areas of the powders were slightly increased as the milling time increased from 1 to 2h and showed a similar trend between samples produced with the same ratio of starting powders. Among the all samples, the highest values were obtained for the A2@1 and A2@2 samples, which are comparable to the particle sizes observed by SEM analyses (Figure 4.5).

Figure 4.10 shows DLS analyses of the prepared catalysts. The powders generated by milling for 1 h have higher sizes, according to these statistics. However, this is due to the fact that this analysis takes into account the clusters that have developed. Furthermore, the particles in these powders, which have significant magnetic characteristics due to the elements they contain, have a natural tendency to attract each other. Therefore, the values obtained from the DLS analysis indicate the average size of the clustered particles.

Despite the clusters of powders, the tendency of the particle size change is comparable to those in the SEM images (Figure 4.5). As seen in Figure 4.10 A2@2 sample presents the smallest average size of the agglomerated particles (333.26 nm) while the average size of free particles was calculated as 60 nm for this sample, according to the SEM analysis (Figure 4.5). The A2@1 sample, presenting the average size of free particles as 70 nm according to the SEM analysis (Figure 4.5), exhibited an average size of the agglomerated particles as 460.36 nm. The fact that the A2@1 and A2@2 samples are substantially smaller than the other catalysts is the most noticeable aspect of the analysis. The reason for this can be attributed to the fact that no impurity phase such as MgO forms in its contents, and it is a pure powder containing metal boride phases (Figure 4.2).

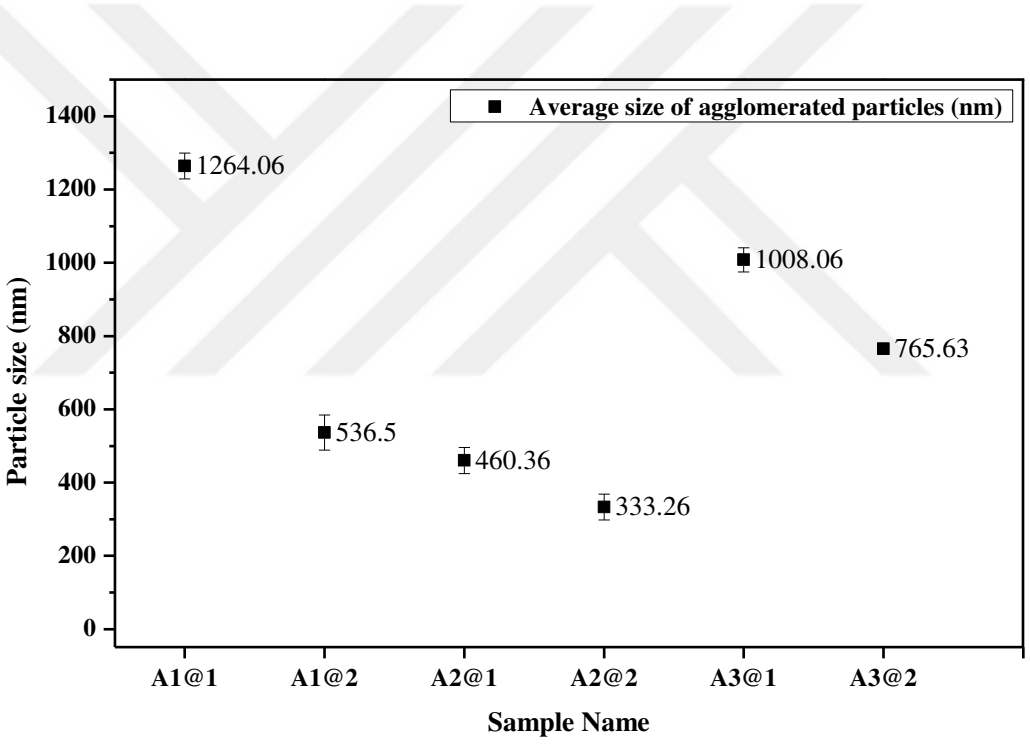

Figure 4.10 Average particle size comparison of selected catalysts derived from DLS particle size analysis.

4.1.3 XPS Analysis of the Synthesized Catalysts

Figure 4.11 shows the XPS spectra of the A1@1 sample. In the Fe2p spectrum, one pair of the peaks at 707.25eV and 721.38 eV indicates the elemental Fe state and the other pair of peaks at 711.81 eV and 725.08 eV indicates the oxidized Fe state. In the Ni2p spectrum the peaks at 852.02 eV and 870.48 eV, and peaks at 855.58 eV and 873.28 eV

attributed to oxidized Ni. Lastly, the peak at 187.54 eV in boronspectra corresponds to alloying B and peak at 191.39 eV corresponds to oxidized B. Thebinding energies of Ni and B demonstrates the construction of the electron structure of Ni_2B at the interface. In addition, the binding energies of oxidized Ni and O at 532.52 eVcorresponds to the NiO [85]. The surface analysis result confirms well with the XRD patterns, where Ni_2B and NiO phases with small amount of Fe impurity were observed (Figure 4.1).

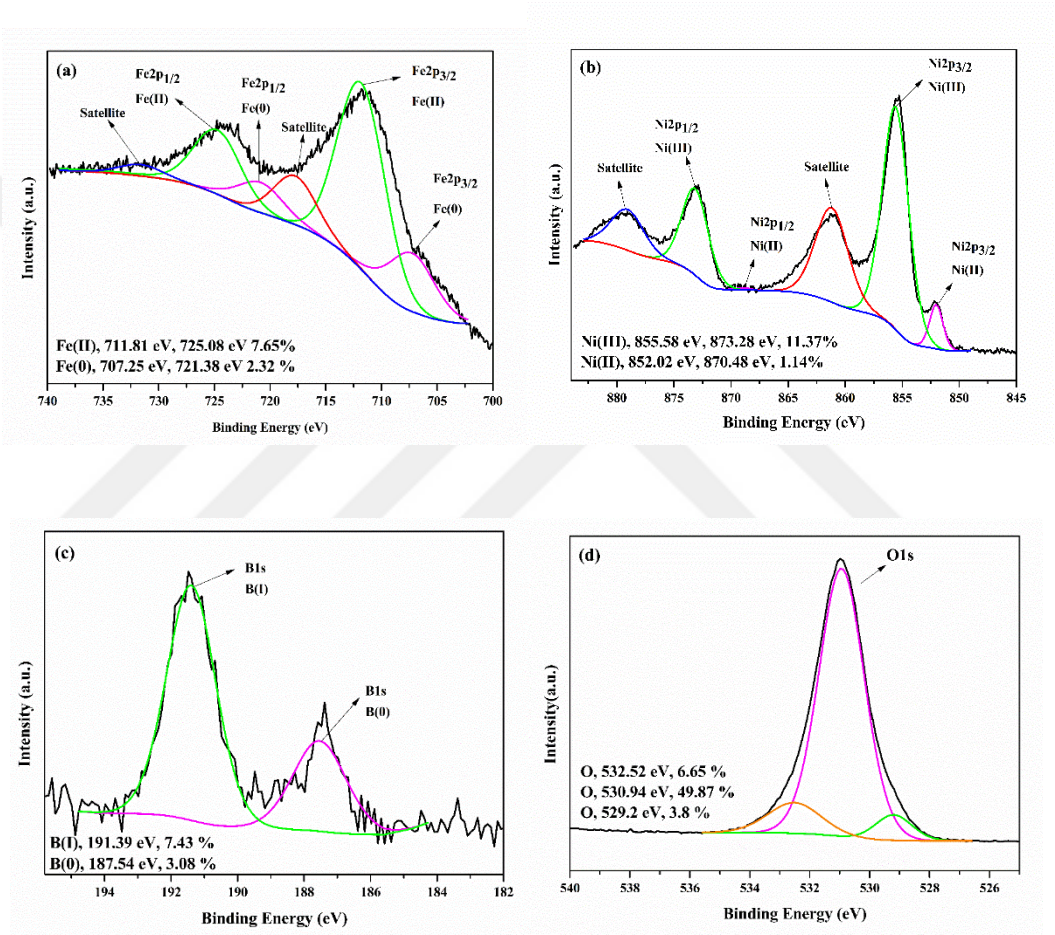

Figure 4.11 XPS spectra of (a) Fe2p, (b) Ni2p, (c) B1s and (d) O1s for the sample A1@1.

Figure 4.12 shows the XPS spectra of A2@1 sample. In the Fe2p spectrum, one pair ofpeaks at 710.85 eV and 724.68 eV indicates the oxidized Fe state [86], [87]. In the Ni2p spectrum the peaks at 852.08 eV and 871.08 eV, and peaks at 855.56 eV and 873.38 eV attributed to oxidized Ni. Lastly, the peak at 187.42 eV in boronspectra corresponds to alloying B and peak at 191.48 eV corresponds to oxidized B. As seen in the B1s spectrum

(Figure 4.11c and Figure 4.12c), the binding energy of boron is higher than in its pure form. This situation can be interpreted as electron transfer from B to Ni as an indication of the existence of B–Ni electronic interaction, which leads to the formation of electron-rich nickel species. When the A1@1 and A2@1 samples are compared, it can be said that the positive shift in the binding energies in the B 1s spectrum is higher in the A2@1 sample, and as a result, the B–Ni interaction is stronger. In addition, when the atomic percentage of boron in the two samples is compared, it is seen that it is higher in A2@1 (16.84%) and supports metal-boride formation. In A1@1 (7.43%), this ratio is less and nickel mostly bonded with oxygen [88], [89]. This situation is also seen when looking at the XRD graph (Figure 4.1). It is an expected result that the formed boride compounds behave as active sites. In the Fe 2p spectrum, a similar condition could be seen. The increase in atomic percentages, in addition to peak positions, reflects the Fe–B concentration in the A2@1 sample. Both of the two boron species found on the surface have the potential to improve the performance of the A2@1 catalyst. Also, the binding energies of Ni and B demonstrates the construction of the electron structure of Ni_3B at the interface [90]. Therefore, it can be confirmed that the prepared catalyst is composed of metal boride species at the surface matching with XRD patterns (Figure 4.2). Finally, according to the spectrum, O 1s peak at 531.04 eV can be correlated with the surface-absorbed oxygen species [91]. According to spectrum, O 1s peak at 531.04 displays the surface-absorbed oxygen species [91]. The reason behind this is that when powders are exposed to the air, they tend to oxidize. Also, XPS analysis of the A2@2 catalyst is specified in Figure 4.13. In the results obtained, it was determined that there was no difference in terms of surface properties, compared to the A2@1 catalyst.

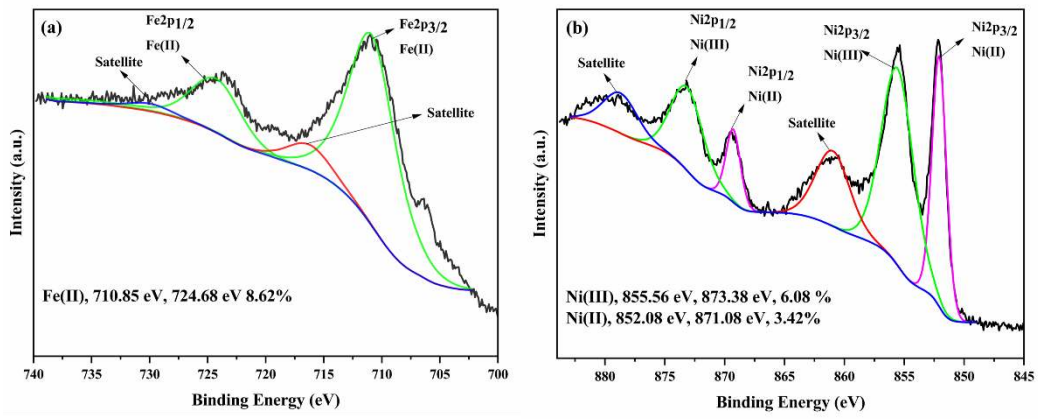

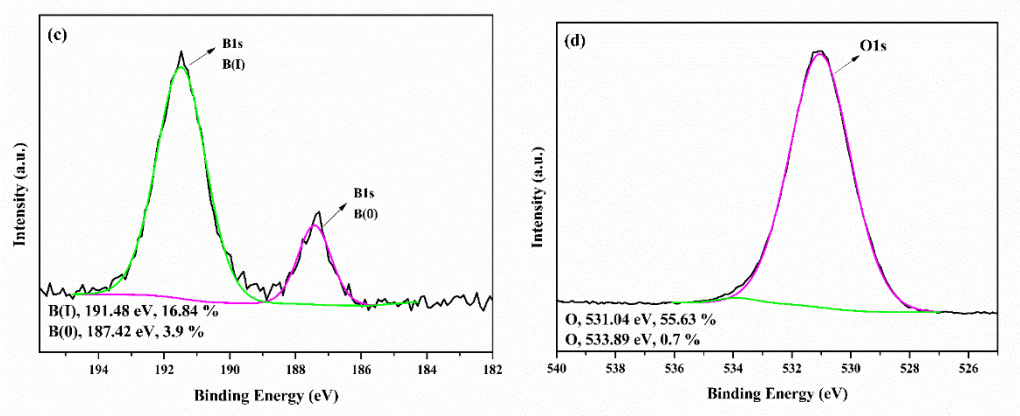

Figure 4.12 XPS spectra of (a) Fe2p, (b) Ni2p, (c) B1s and (d) O1s for the sample A2@1.

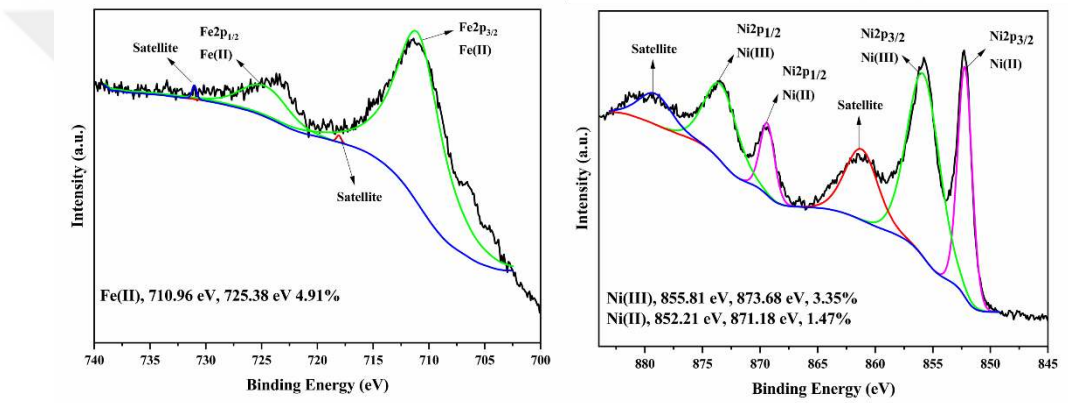

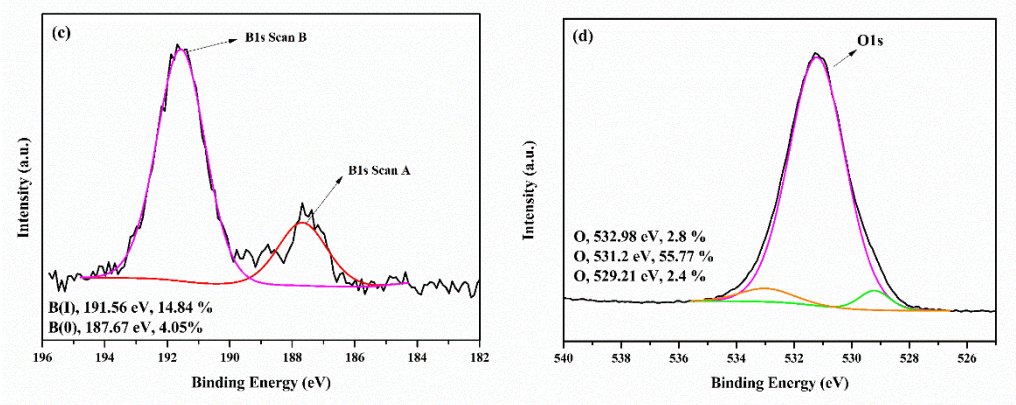

Figure 4.13 XPS spectra of (a) Fe2p, (b) Ni2p, (c) B1s and (d) O1s for the sample A2@2.

The XPS spectra of the Mg and O for the sample A3@1 sample is given in the Appendix (Figure A.4). From here, the formation of the MgO phase on the surface can also be determined. The surface analysis result confirms well with the XRD patterns.

4.1.4 Catalytic Performance Measurements

Figure 4.14 shows the evolution of equivalent hydrogen per mole of $NaBH_4$ versus time plot for the hydrolysis of $NaBH_4$ solution at 25°C of the synthesized catalysts. The amount of hydrogen produced and the reaction time are almost directly proportional for all catalysts, confirming that the catalytic activity of the catalysts is stable. When the hydrogen evolution of the A2@1 and A2@2 catalysts is examined, it is determined that they have the highest performances. Unlike other catalysts, the presence of boron phases was increased by the excess amount of $NaBH_4$ in their chemical composition, and this presence had a beneficial influence on hydrogen evolution. A2@1 and A2@2 semi-crystalline catalyst powders with Ni_3B–FeB phases (Figure 4.2) completed the hydrolysis reaction in the shortest time. Positive shifts in binding energies are larger in the A2@1 sample (Figure 4.12), indicating more metal-boron electrical interaction, as determined by XPS analysis. It's reasonable to conclude that the active sites formed here are the most crucial factor influencing catalytic performance. Combining some transition metals (such as Fe, Co or Ni) with metalloid atoms (such as P or B) modifies the intrinsic electronic states of transition metals, resulting in improved catalytic activity [58], [59]. As a result, the catalysts A2@1 and A2@2, which have a boron-rich semi-crystalline structure (Figure 4.2), are expected to finish the hydrolysis reaction the fastest (Figure 4.12). When compared to the others, the A3@1 and A3@2 catalysts had lower activity. In fact, the crystalline Fe_2B–Ni_4B_3 phases they contain improved the catalytic activity of the catalysts. However, the presence of phases containing MgO, which formed due to excess Mg powder in their content, negatively affected the purity and this effect was also reflected in their catalytic performance. A3@1 and A3@2 catalysts exhibit heterogeneous morphology, as shown in SEM pictures, in addition to the phases they contain (Figure 4.5). Furthermore, average particle sizes exceed 700 nm, which confirms the decrease in hydrogen generation rate of A3@1 and A3@2 when compared to A2@1 (460.36 nm) and A2@2 (333.26 nm) (Figure 4.10). Since the A4@1 and A4@2 samples did not show catalytic activity, they are not included in the graph.

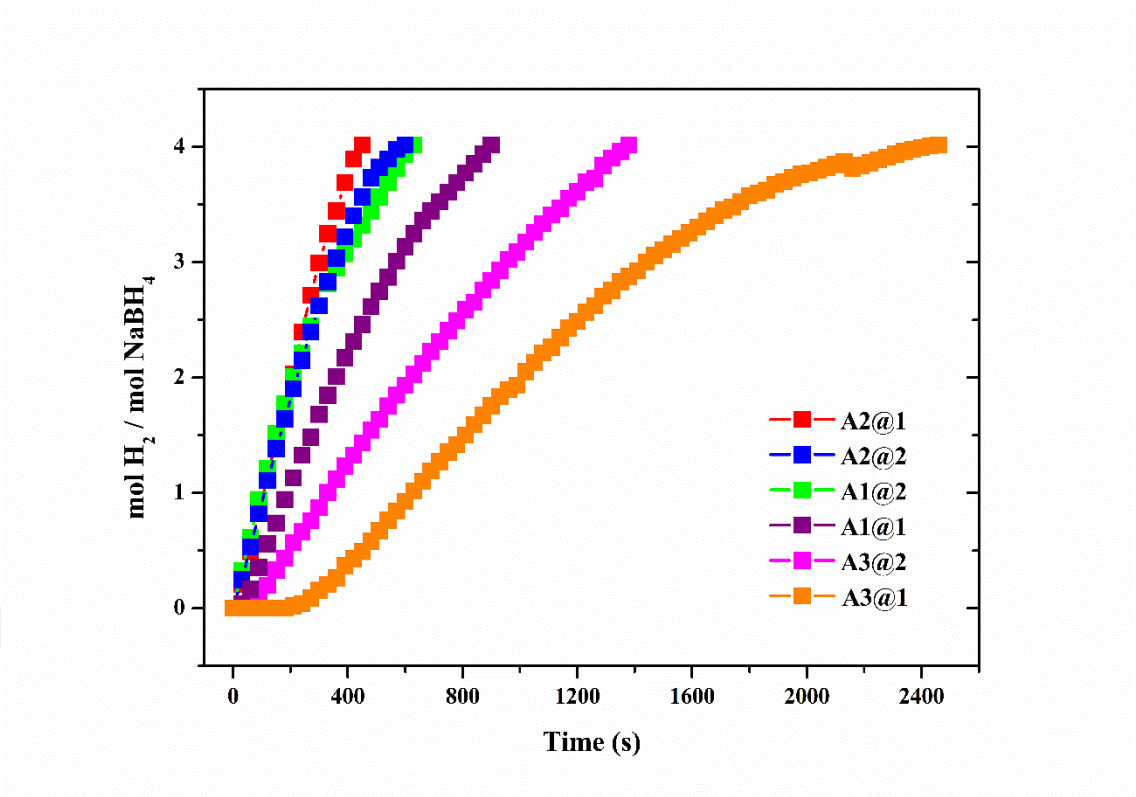

Figure 4.14 The evolution of equivalent hydrogen per mole of $NaBH_4$ versus time plot for the hydrolysis of 5 mL of 0.2 M $NaBH_4$ containing 10 mmol NaOH in the presence of different catalysts (20 mg) at 25 °C

Activation energies and HGR values of the synthesized catalysts are shown in Table 4.1. To get the data, hydrogen production rates were estimated using graphs of hydrogen production volume versus time (min) and the unit of catalyst amount (g); the hydrogen production rate was expressed in ml H_2 min^{-1} $gcat^{-1}$. In order to determine the performances and calculate the activation energy values of the synthesized catalysts, hydrolysis reaction was carried out with $NaBH_4$ at 25, 30, 35, 40 and 45 °C. The HGR increased as the temperature was raised from 25 to 45 °C, as expected. The synthesized catalyst's Arrhenius curve was calculated using data from hydrolysis experiments conducted at various temperatures. In this way, the activation energy of the $NaBH_4$ hydrolysis reaction in the presence of the synthesized catalyst could be calculated. The Arrhenius equation (Equation 2) and the details of the calculation of the activation energy are given above in the heading *3.3 Hydrolysis of $NaBH_4$*. Accordingly, the activation energies of the catalysts calculated from the slopes of the Arrhenius curves are given in Table 4.1.

When all catalysts' HGR values are compared, it's clear that the A1@1 and A2@1 samples synthesized with 1 h of milling time have higher catalytic activity in $NaBH_4$ hydrolysis.

Table 4.1 Properties and performance of the catalysts at room temperature

Catalyst	Hydrogen Generation Rate (ml H_2 min^{-1} g_{cat}^{-1})	Activation Energy (kJ/mol)
A1@1	681.81	59.2
A1@2	505.45	62.3
A2@1	758.0	40.8
A2@2	536.36	48.9
A3@1	90.90	69.6
A3@2	192.72	63.6
A4@1	No activity	-
A4@2	No activity	-

The hydrogen production graph and corresponding Arrhenius plot is representatively presented here for the A2@1 catalyst, which has the highest HGR ratio. Figure 4.15a illustrates the hydrogen productions at five selected temperatures, with the time for the catalyst to consume $NaBH_4$ in the reaction decreasing as the temperature increased. Table 4.2 shows the details of the amount of increase in HGR values, as the temperature rises. When the temperature reaches to 45°C, HGR can achieve 1600 ml H_2 $min^{-1}g_{cat}^{-1}$, according to this Table. The A2@1 catalyst's Arrhenius curve was calculated using data from hydrolysis experiments conducted at various temperatures and it is shown in Figure 4.15b.

The rate graphs were compared to reaction kinetic models of zero order, first order, and second order. As a result, the hydrolysis reaction with the synthesized catalysts has been determined to be suitable for the 'zero order' kinetic model. In addition, in various studies in the literature, it has been stated that the hydrolysis reaction of $NaBH_4$ is in 'zero order' reaction kinetics [66], [74]–[76]. A2@1 catalyst showed the best performance with the lowest activation energy value, 40.8 kJ/mole, and highest HGR. The zero-order rate constants of the A2@1 catalyst provided in Appendix (Table A.3). The Arrhenius curve details of the A2@2 catalyst, which showed the best performance after A2@1, are given in Figure 4.16. In addition, the Arrhenius curves of A1@1 and A1@2 catalysts containing metal oxide (NiO) phase are shown in Figure 4.17(a) and (b) respectively. It should be particularly noted that the A2@1 and A2@2 catalyst powders, which is said to have the

best performance here, had the highest BET surface area results (41.80 and 46.38 m^2/g) among the samples.

(a)

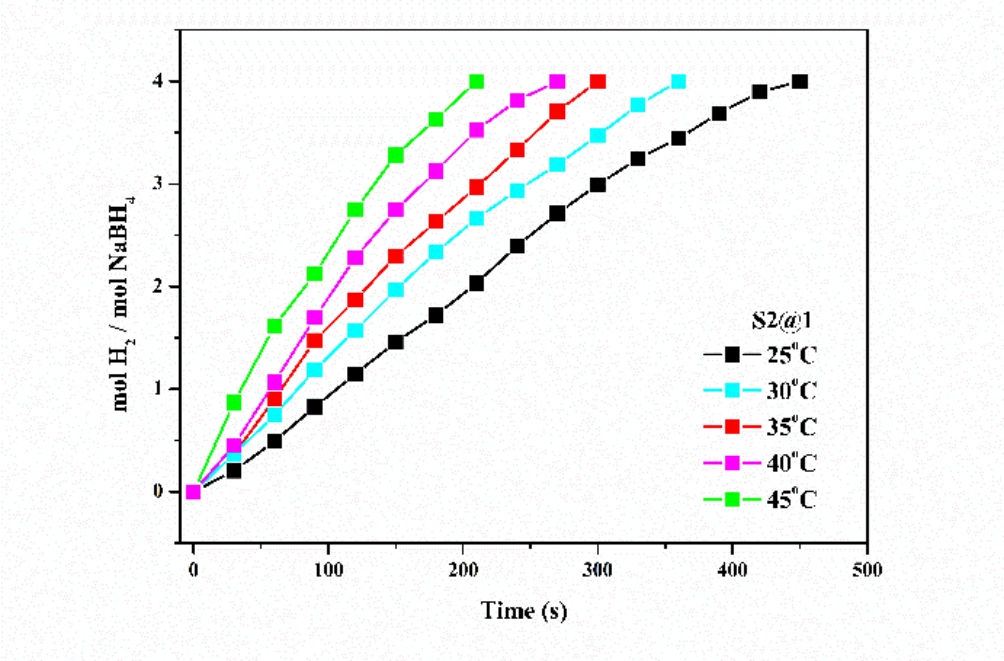

(b)

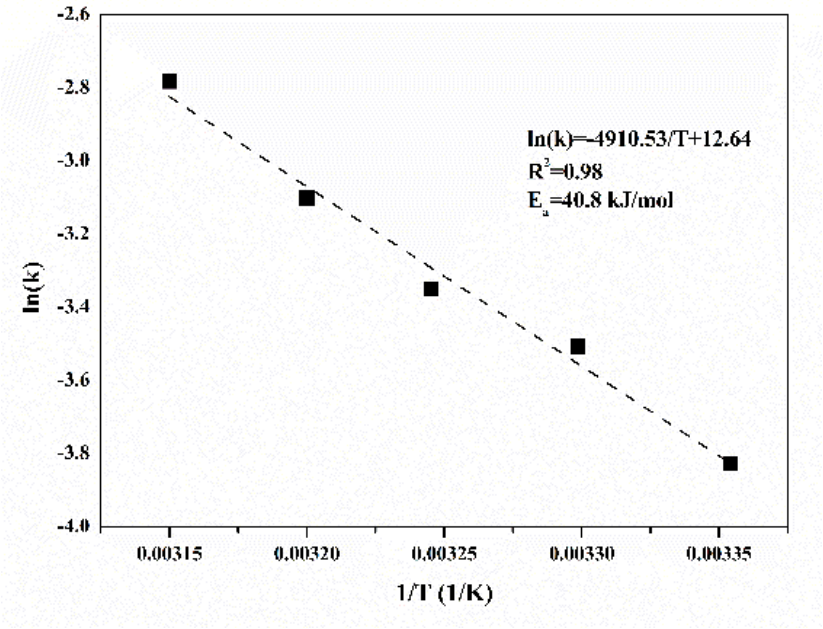

Figure 4.15 The evolution of equivalent hydrogen per mole of $NaBH_4$ versus time plot in the presence of A2@1 catalyst: (a) at different temperatures and (b) the corresponding Arrhenius plot (Hydrolysis conditions: 5 mL of 0.2 M $NaBH_4$ containing 10 mmol NaOH in the presence of 20 mg of the catalyst).

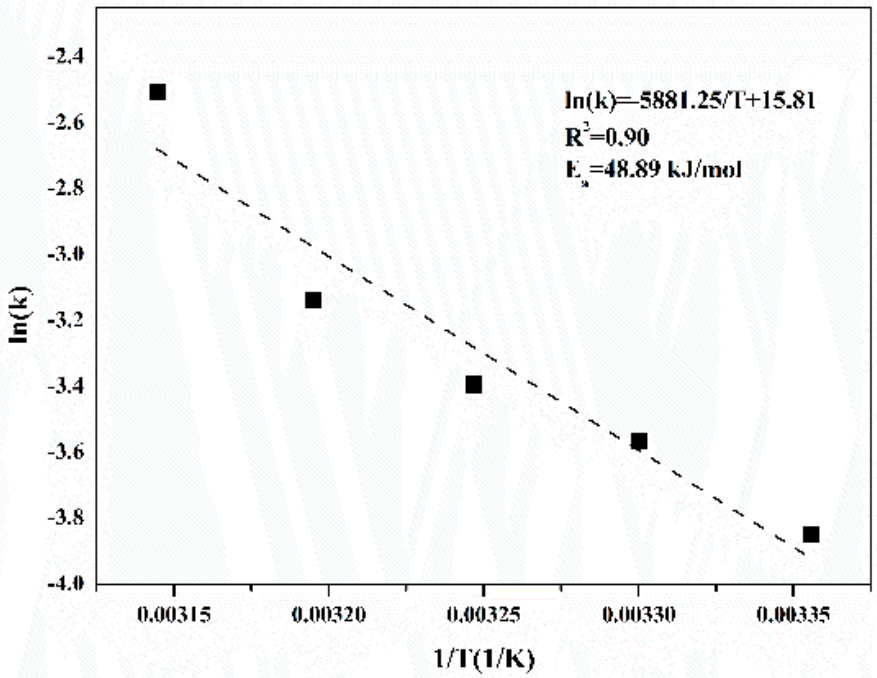

Figure 4.16 The Arrhenius plot of A2@2 catalyst (Hydrolysis conditions: 5 mL of 0.2 M $NaBH_4$ containing 10 mmol NaOH in the presence of 20 mg of the catalyst).

(a)

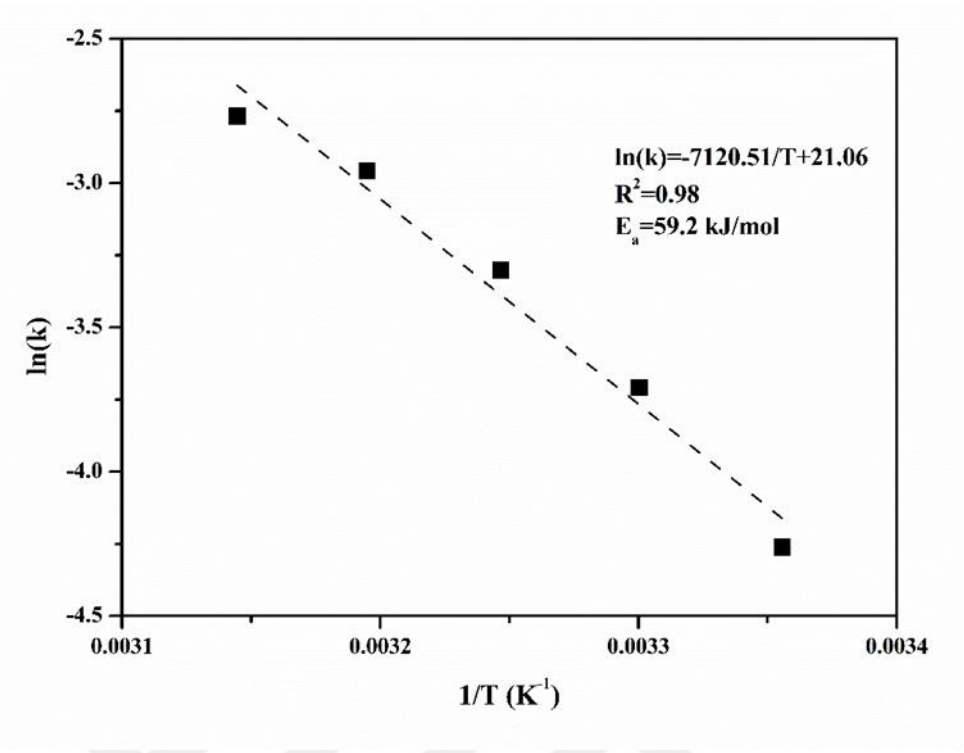

(b)

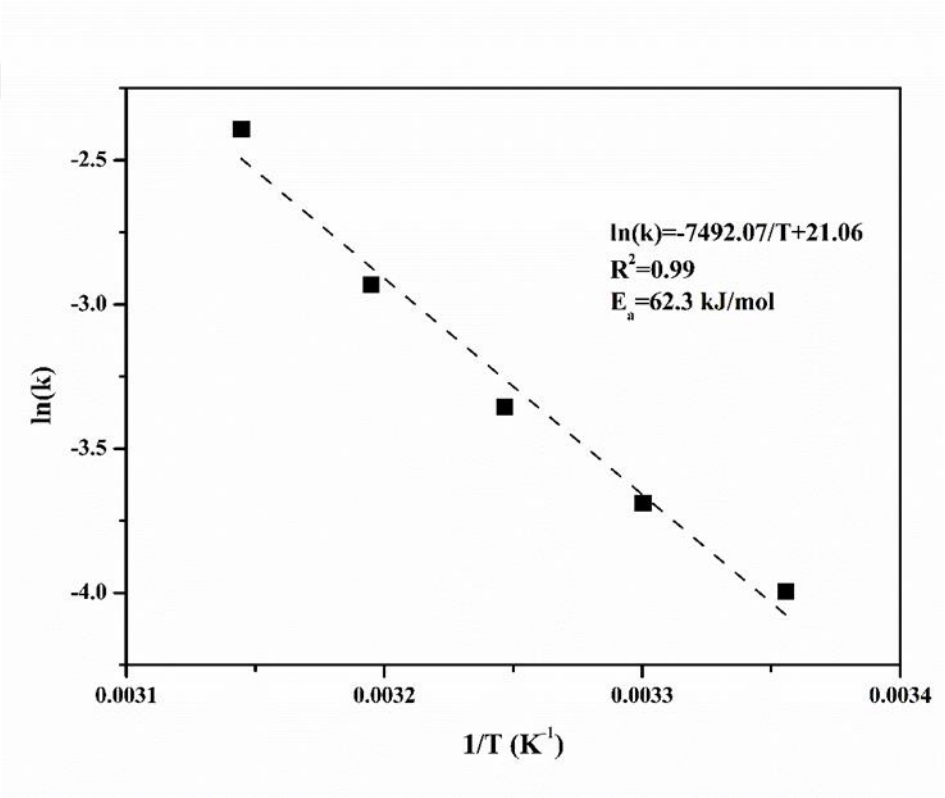

Figure 4.17 The Arrhenius plot of (a) A2@1 catalyst and (b) A2@1 (Hydrolysis conditions: 5 mL of 0.2 M $NaBH_4$ containing 10 mmol NaOH in the presence of 20 mg of the catalyst).

Table 4.2 A2@1 catalyst powders' hydrogen generation rates at selected temperatures by hydrolysis of $NaBH_4$ solution and calculated activation energy value (Hydrolysis conditions: 5 mL of 0.2 M $NaBH_4$ containing 10 mmol NaOH in the presence of 20 mg of the catalyst).

Catalyst Powder	Hydrolysis exp. temperature (°C)	Hydrogen generation rate (ml H_2 min^{-1} g_{cat}^{-1})	Activation energy (kJ/mol)
A2@1 (FeB–Ni_3B)	25	758.0	40.8
	30	836.36	
	35	1034.28	
	40	1228.57	
	45	1600.0	

Hydrogen generation rates and activation energies of various catalysts used for $NaBH_4$ hydrolysis in literature are given in Table 2.1. Compared to these values in Table 2.1, the A2@1 catalyst clearly displayed a high HGR value and a low activation energy. When Nie et al. synthesized the Ni–Fe–B catalyst, they were able to achieve an activation energy value of 57.8 kJ/mol in a 5 wt.% $NaBH_4$ solution. However, in this study, a value of 40.8 kJ/mol was achieved in the amount of $NaBH_4$, which is almost one in seven [38]. The powder containing Ni_3B phase synthesized by Walter et al., on the other hand, had an HGR value of 1298 ml H_2 min^{-1} g_{cat}^{-1} at 60 °C, according to the report [62]. The FeB-Ni_3B (A2@1) catalyst, on the other hand, could achieve a value in this range with significantly less solution at a temperature of 45 °C, confirming its remarkable catalytic capabilities. With NiB/$NiFe_2O_4$ catalysts containing oxygen, Liang et al. were considerably behind A2@1 in terms of activation energy and HGR values [93]. This demonstrates that A2@1's FeB-Ni_3B phase has a direct impact on the catalytic performance. The performance of Ni-Co_{20}-P@NF and CoP@NF catalysts has been claimed to be greater than A2@1 [94]. However, in these catalysts, NF was utilized as a support material, and it is well known that using a support material improves the catalytic effect. In contrast, the A2@1 catalyst is competitive with other catalysts in the literature, with a homogenous structure synthesized in a single step without the use of any support material.

Recyclability test was performed on A1@1, A2@1 and A3@1 catalysts. In this way, the stability of the powder was tried to be investigated. The hydrolysis reaction was started at room temperature. After ensuring complete $NaBH_4$ hydrolysis, the same amount of $NaBH_4$ was added to each cycle to remeasure the catalyst powder's activity under

identical conditions. Figure 4.18(b) indicates that A2@1's performance degrades over time, although the catalytic activity is maintained even after several cycles. Furthermore, after the 4th cycle, there is no remarkable difference in performance. After repeated use, the boron-rich A2@1 catalyst was able to successfully complete the hydrolysis reactions. This indicates that the powder not only has a low activation energy and a high hydrogen generation rate, but also performs remarkably well enough in terms of stability. The A1@1 catalyst, which exhibits higher activation energy than the A2@1 catalyst, also showed lower performance in the recyclability test, as shown in Figure 4.18(a). However, it can be seen that the catalyst powder can successfully complete the reaction in every cycle. It is clear that the scenario in A3@1 is different in Figure 4.18(c). The experiment continued until the fourth cycle, which took over an hour. As a result, the fifth cycle hadn't measured and not represented in the graph. Because of the presence of impurity phases in the catalyst powder, it performed relatively worse performance in recycling tests. It can be concluded that the best-performing A2@1 catalyst completed the 5th cycle in a very short time of about 13 min, indicating its high durability during the recyclability tests.

(a)

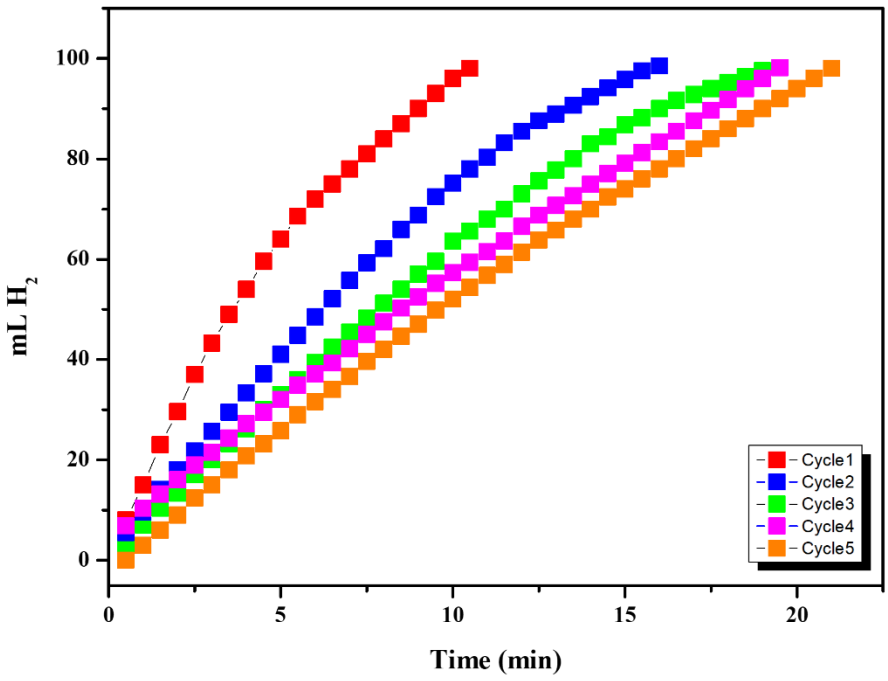

(b)

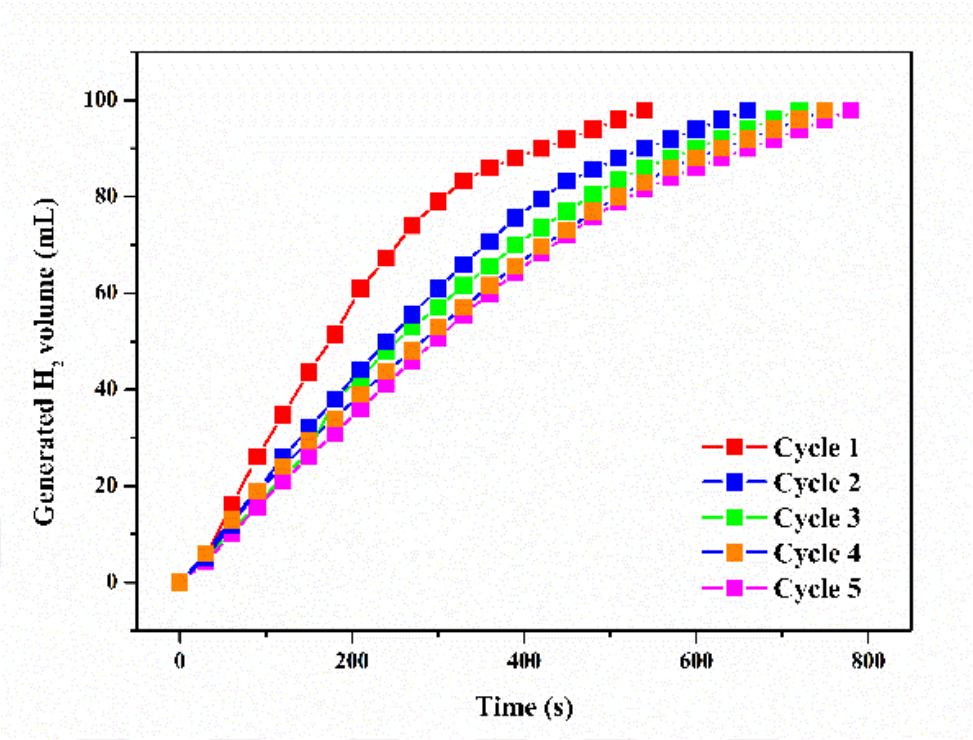

(c)

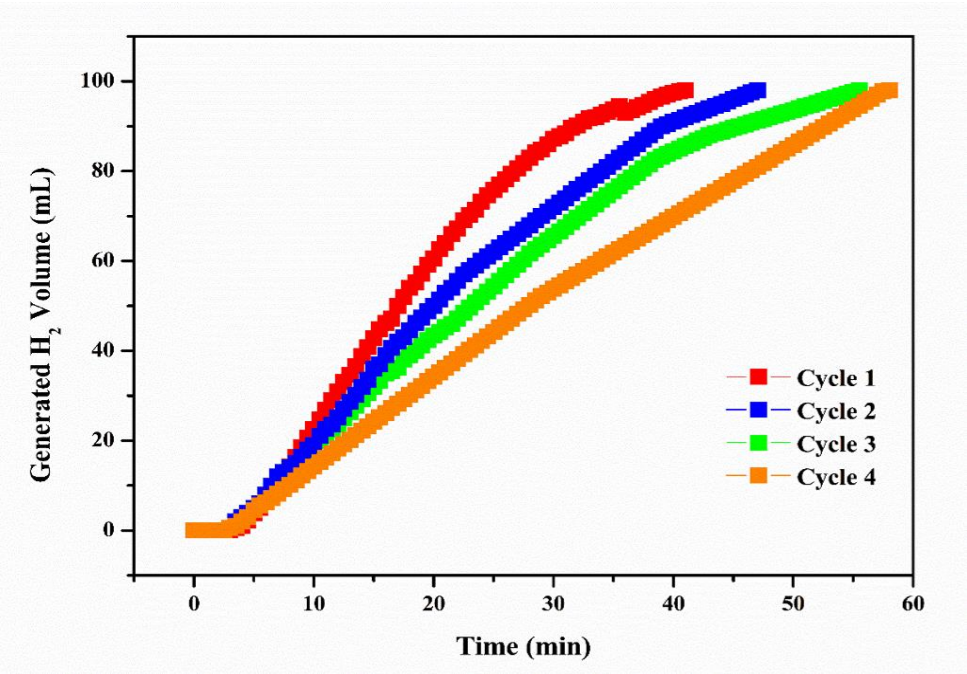

Figure 4.18 Evolution of hydrogen (mL) versus time plot for (a) A1@1, (b) A2@1, (c)A3@1 showing the recyclability of the catalysts for 5 cycles (Hydrolysis conditions

for each cycle: 5 mL of 0.2 M $NaBH_4$ containing 10 mmol NaOH in the presence of 20 mg of the catalyst).

The A2@1 powder was dried again after the recyclability tests were completed, and the XRD result was analyzed. According to this result, the formation of residual oxidized phases is observed at the end of the fifth round. The reason for the increasing cycle time can be shown as the presence of these oxidized phases. The XRD pattern is given in the Appendix (Figure A.5).

4.2 Co-Ni-B System

4.2.1 Phase and Chemical Analysis of the Synthesized Catalysts

Figures 4.19 and 4.20 show the XRD patterns of the synthesized Co–Ni–B catalysts. The XRD patterns of the synthesized Co–B and Ni–B binary boride catalysts are presented in Figure 4.21. As seen from the XRD analyses, all the powders synthesized at 850 and 900°C by using $CoCl_2$–$NiCl_2$–$NaBH_4$ mixtures consist of crystalline Co/Ni–B and Co–Ni–B-based metal boride composites. The used synthesis method enabled the simultaneous formation of the binary/ternary compounds via a one-step reaction of $CoCl_2$–$NiCl_2$–$NaBH_4$ mixture in an inorganic molten salt environment. According to the changing synthesis parameters, different compositions of the metal boride composites were formed including the crystalline CoB, Co_2B, Co_5B_{16}, NiB, Ni_4B_3, and $Ni_2Co_{0.67}B_{0.33}$ phases. Table A.4 presents the ICDD Card information for all the crystalline phases, while Table A.5 shows the indices for the corresponding diffraction peaks of the all obtained phases (Appendix). It is clear that the ratio of metal chlorides to $NaBH_4$ and reaction temperature significantly affected the formed phases, which made the preparation of different catalysts possible. As the $CoCl_2$–$NaBH_4$ or $NiCl_2$–$NaBH_4$ binary systems were used as starting mixtures with a ratio of metal chlorides to $NaBH_4$ as 1:6, single phases of CoB or Ni_4B_3 binary borides were formed, respectively (Figure 4.21). However, as the $CoCl_2$–$NiCl_2$–$NaBH_4$ ternary system was used with a ratio of metal chlorides to $NaBH_4$ as 1:3 and 1:6, mixed compositions containing different binary and ternary compounds were achieved (Figures 4.19 and 4.20). The formation of $Ni_2Co_{0.67}B_{0.33}$ ternary phase was only observed in the S2@850 sample (Figure 4.19(c)), where elemental boron was added to the starting mixture (+2 mole of B). On the other hand, nickel-rich Ni_4B_3 phase was

occurred, when the starting ratio was 1:6 (Figure 4.20), whereas the formed phase including Ni was NiB in the case of the ratio as 1:3 (Figure 4.19). Thus, playing with the metal chloride to $NaBH_4$ ratio seems to affect the phase of the Ni-containing crystal. On the other hand, despite the use of the same reaction temperature and starting ratio (Figure 4.20(a) and (c)), mechanical alloying of the starting mixture prevented the formation of NiB and thereby resulted in the powders containing only CoB and Ni_4B_3 phases. In overall, it can be indicated from the XRD peaks that the increase in reaction temperature from 850 to 900 °C caused a slight increase in the crystallinity of the CoB phase (Figures 4.19(b) and 4.20(b)).

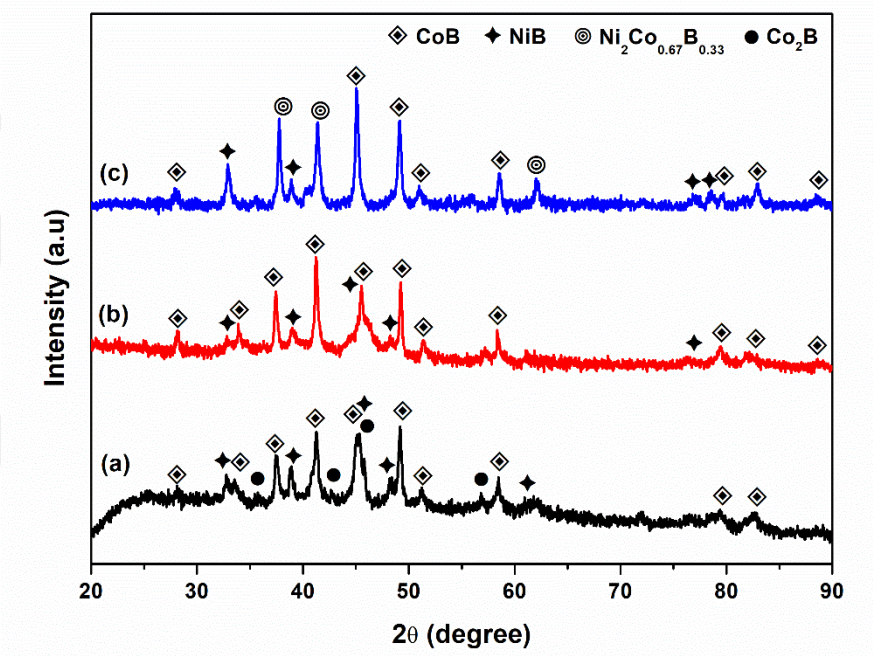

Figure 4.19 XRD patterns of the synthesized Co–Ni–B catalysts: (a) S1@850, (b) S1@900 and (c) S2@850.

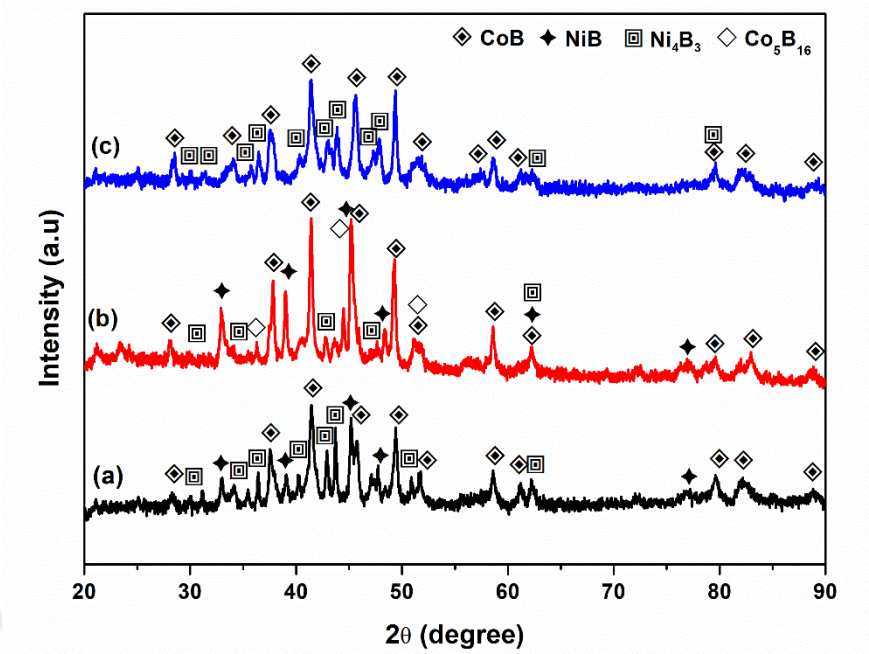

Figure 4.20 XRD patterns of the synthesized Co–Ni–B catalysts: (a) S3@850, (b) S3@900 and (c) S4@850.

(a)

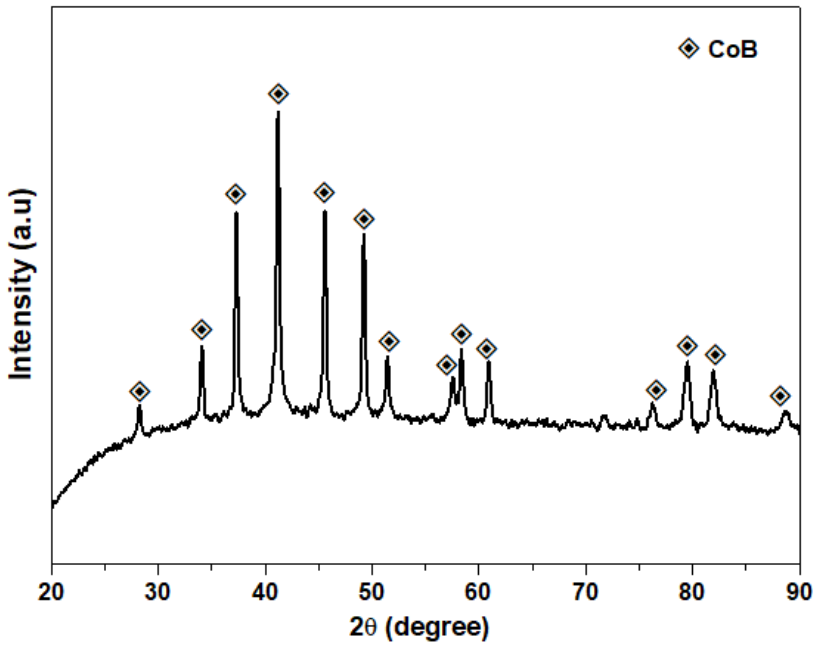

(b)

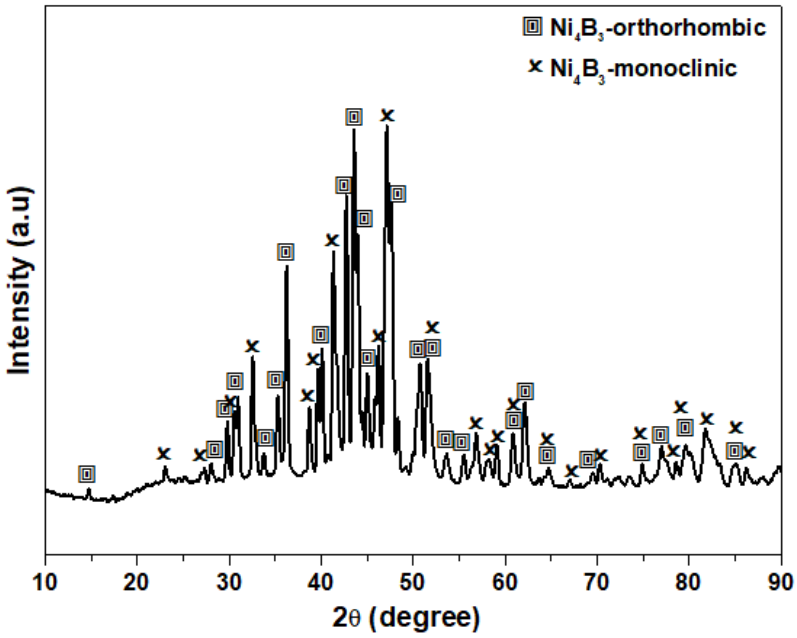

Figure 4.21 XRD patterns of the synthesized Co-B and Ni-B binary boride catalysts: (a) S5@850 and (b) S6@850.

Table 4.3 summarizes the phase compositions obtained from the XRD patterns and presents the chemical analyses of the synthesized catalysts. Chemical analyses of the ternary systems revealed the Co and Ni elemental compositions as similar values for all compositions in between 31–41 and 32–45 wt. %, respectively (Table 4.3). Only the S3@900 sample with high boron content showed an exception with the Co and Ni values at about 28 wt. %, most likely due to the high amount of starting $NaBH_4$ and relatively high reaction temperature of 900°C. On the other hand, the powders contain slight amount of K and Cl impurities (0.2–0.9 wt. %) stemming from the KCl inorganic compound, which could not be completely removed from the system. It could be declared that this Cl impurity may have a decreasing effect on the hydrogen generation rate. Thus, this impurity are trace amounts and almost in the same range for all of the catalysts.

Table 4.3 Phase composition of the synthesized catalysts.

Sample Name	Phase and chemical analysis				
	Formed crystalline phases (XRD analysis)	Elemental composition (wt. %) (XRF analysis)			
		Co	Ni	K	Cl
S1@850	CoB–NiB–Co_2B	40.3	41.6	0.6	0.9
S1@900	CoB–NiB	31.8	32.5	-	0.4

S2@850	CoB–NiB–$Ni_2Co_{0.67}B_{0.33}$	40.7	44.7	-	0.2
S3@850	CoB–Ni_4B_3–NiB	40.5	38.5	0.9	-
S3@900	CoB–Ni_4B_3–NiB–Co_5B_{16}	28.6	28.9	0.3	0.9
S4@850	CoB–Ni_4B_3	35.0	36.2	0.5	0.6
S5@850	CoB	82.8	-	0.4	0.2
S6@850	Ni_4B_3	-	85.4	0.5	-
CP	Co_2B–Co_3B				

4.2.2 Microstructures and Particle Sizes of the Synthesized Catalysts

Figure 4.22 presents the FE-SEM images of the synthesized Co–Ni–B, Co–B and Ni–B catalysts. It is observed that the particles possess a spherical-like morphology, which can be attributed to the autogenic pressure present inside of the sealed tubes during the synthesis process. The spherical-like morphology of the catalysts can be better observed in the high magnification FE-SEM images of the selected powders, shown in Figure 4.23. SEM images of the particles present a homogeneous distribution throughout the samples, most likely because of the effect of roll milling or mechanical alloying processes during the preparation step, and also the molten salt environment of the synthesis process. Especially the S4@850 sample revealed a uniform and fine microstructure due to the positive effect of mechanical alloying. To better observe its whole microstructure, the low-magnification SEM image of this sample is presented in Figure 4.24. Nano-sized particles are seen in agglomerated forms in low magnification image of S4@850 sample (Figure 4.22(d)). In compliance with the SEM images, all XRD patterns exhibited peak broadening indicating the nanocrystalline character of the obtained particles (Figures 4.19 and 4.20).

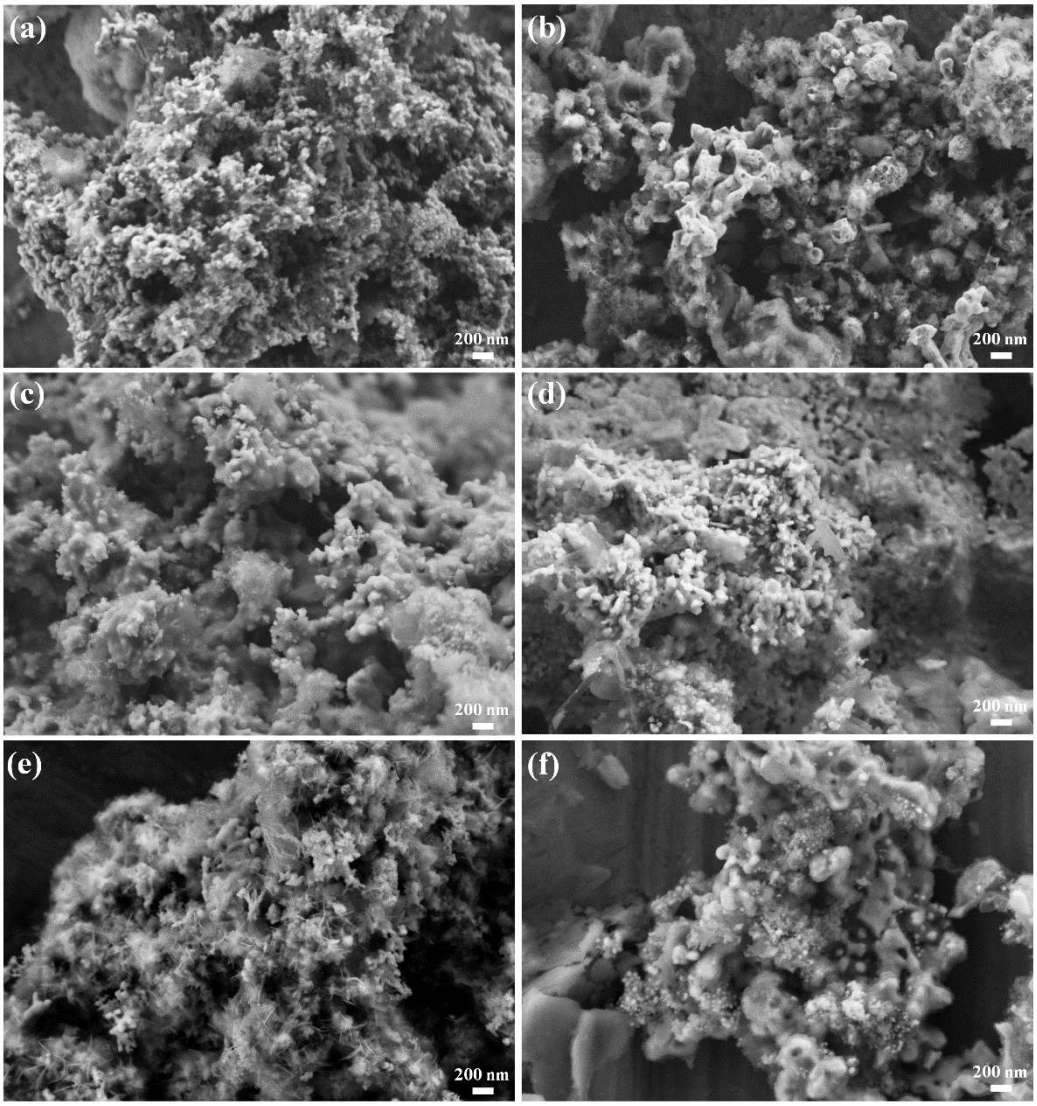

Figure 4.22 Secondary electron FE-SEM images of the synthesized Co–Ni–B, Co–B and Ni–B catalysts: (a) S1@850, (b) S1@900, (c) S3@900, (d) S4@850, (e) S5@850, and (f) S6@850

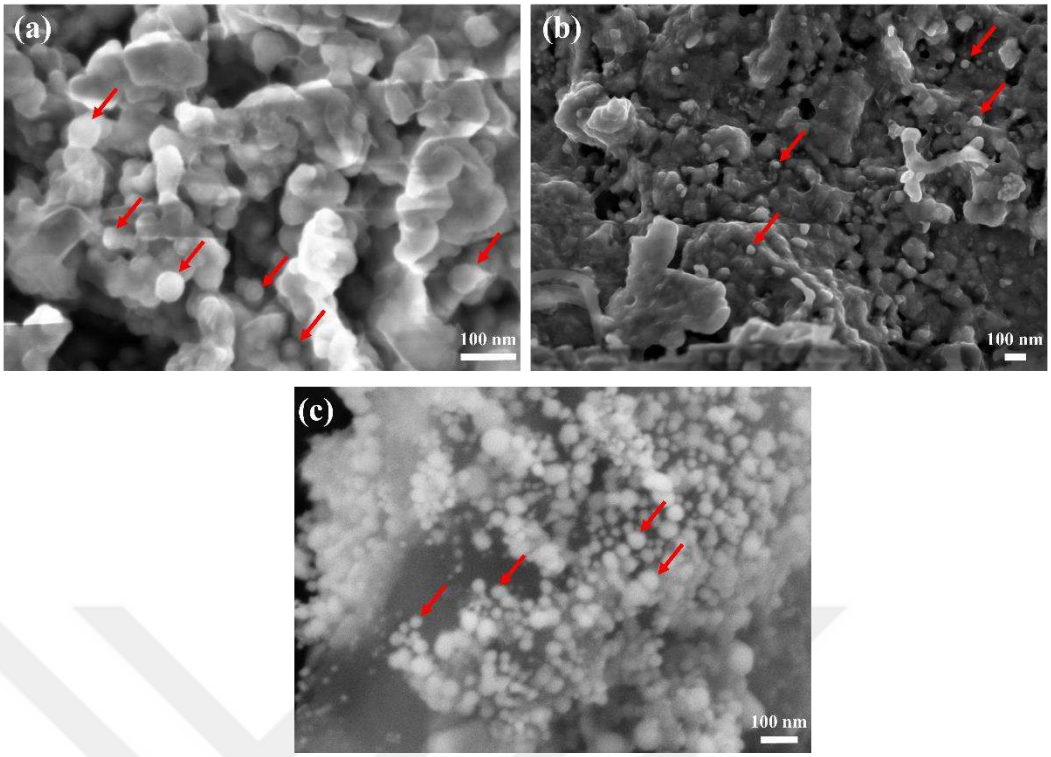

Figure 4.23 High magnification SEM images of the selected catalysts: (a) S1@850, (b) S4@850, (c) S6@850. (The red arrows indicate the spherical-like morphology).

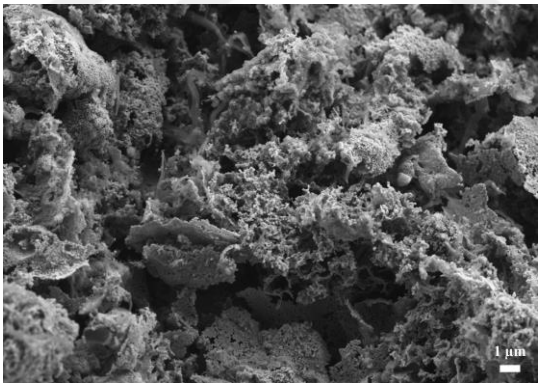

Figure 4.24 Low magnification SEM image of the S4@850 sample.

In order to confirm the uniformity of all elements distribution, SEM/EDX analyses are performed on the catalysts. The homogenous distribution of nickel, cobalt and boron elements can be observed in Figure 4.25, for the selected sample of S4@850. The elemental Co and Ni maps coincide entirely with the elemental B map, supporting the simultaneous presence of cobalt and nickel boride phases detected by XRD analysis (Figure 4.20(c)). EDX analyses for the other catalysts are given in Figure 4.26 to show the distribution of all elements throughout the samples. The weak signals of B particles

in all analysis results can be associated with the suppression effect of the other strong signals of the Co and Ni elements. Furthermore, any signals of other elements were not detected during the EDX analyses, which also proves the purity of the catalyst powders.

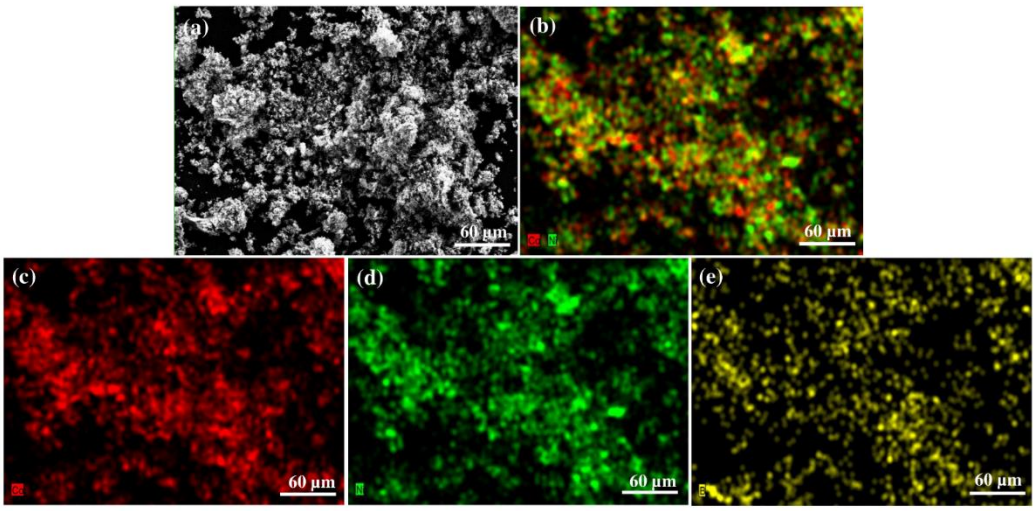

Figure 4.25 (a) SEM image of sample S4@850, (b) EDX mapping of sample S4@850, (c) EDX mapping of Co, (d) Ni, (e) B in sample S4@850.

(a)

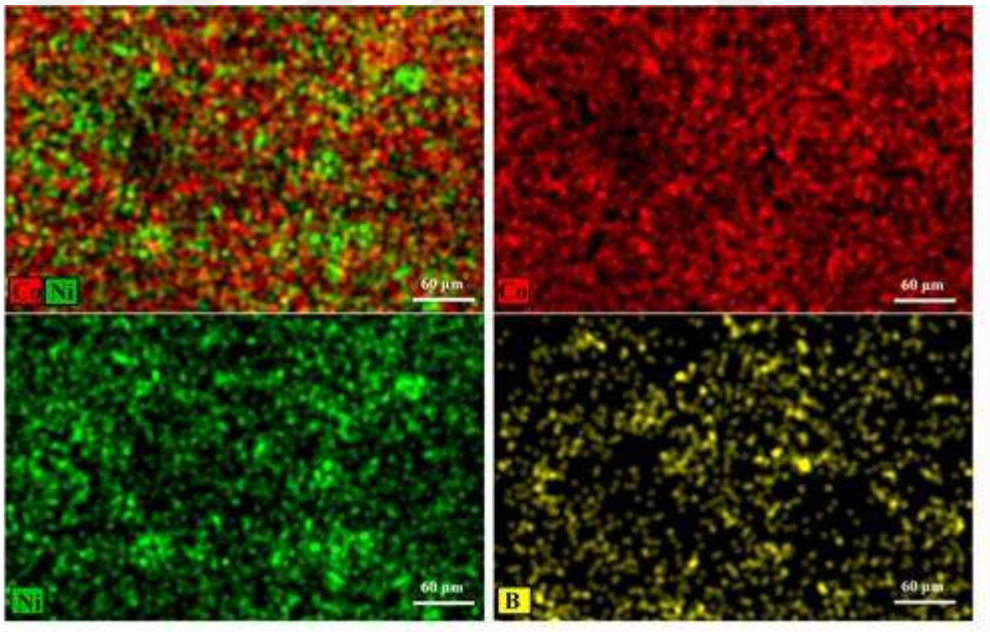

(b)

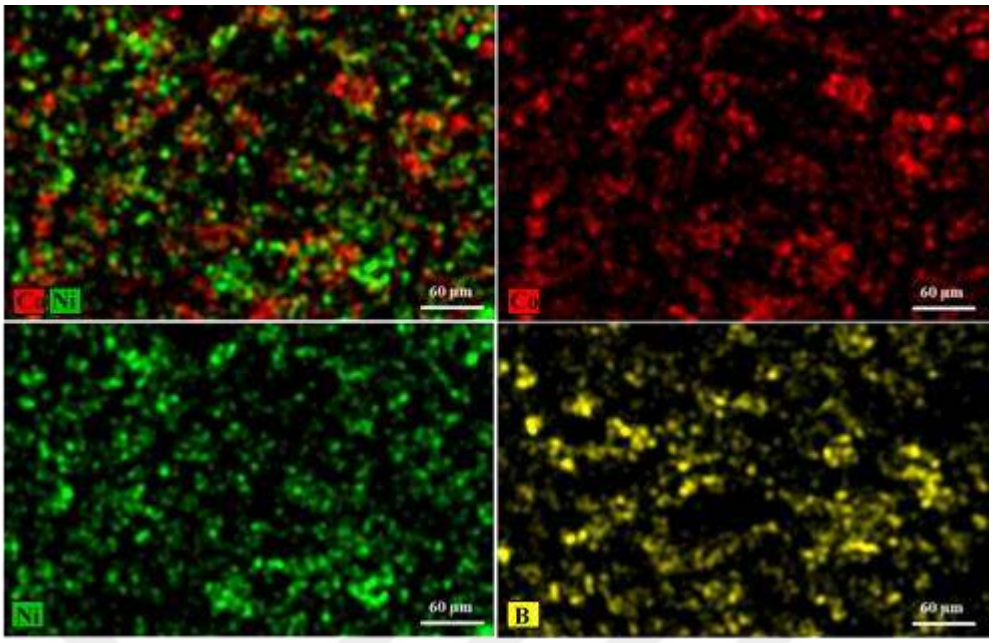
Co Ni
60 µm
Co
60 µm
Ni
60 µm
B
60 µm

(c)

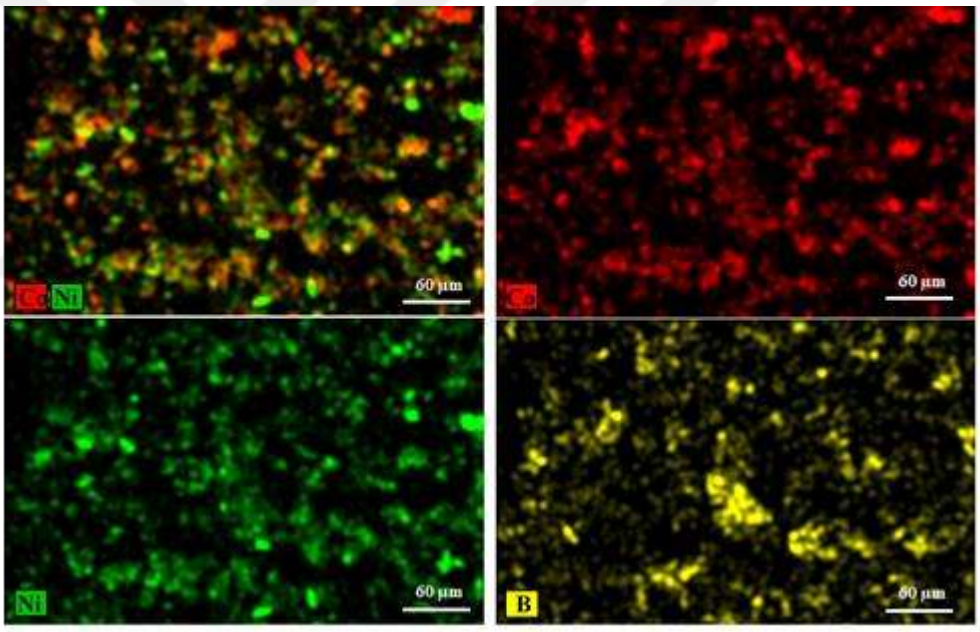
Co Ni
60 µm
Co
60 µm
Ni
60 µm
B
60 µm

(d)

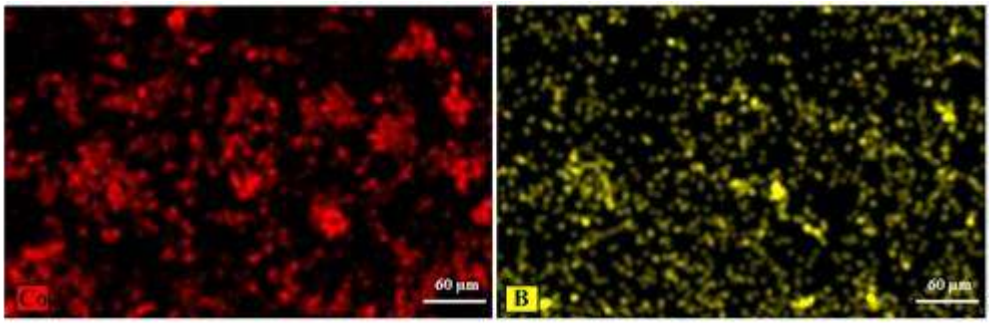
Co
60 µm
B
60 µm

(e)

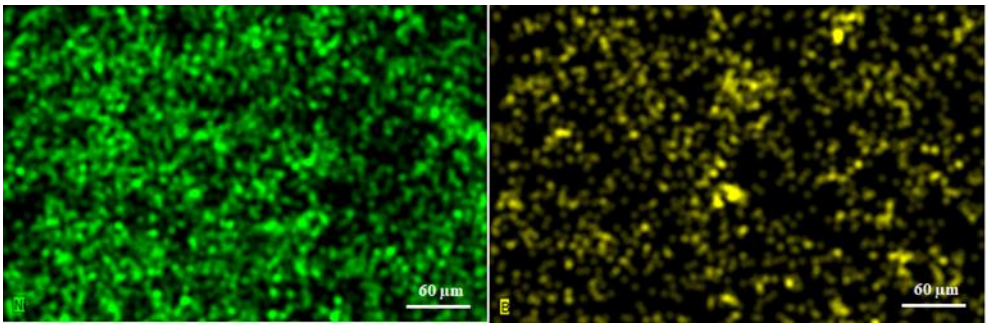

Figure 4.26 EDX analyses for the catalyst samples: (a) S1@850, (b) S1@900, (c) S3@900, (d) S5@850, (e) S6@850.

Figure 4.27 shows the particle size measurements of the catalysts that is derived from the SEM and DLS analyses. As seen in Figure 4.27(a), average particle sizes of the powders are changing from ~51 to 94 nm. Particle size distribution graphs of the selected samples are shown as representative for all samples, which have a uniform particle size distribution (Figure 4.27(b) and 4.27(c)). The average particle size of S4@850 sample is determined as 62.4 and 65 nm according to the SEM and DLS analyses, respectively, in which comparable values are obtained despite of the different techniques. The data also indicate that when using the same ratio of metal chlorides to $NaBH_4$ during the synthesis, an increase in the reaction temperature from 850 to 900 °C resulted in an increase in the particle size. Namely, while the particle size in S1@850 was 51.7 nm, the particle size in S1@900 was 94.0 nm. Similarly, the particle size increased from 68.2 nm to 77.8 nm when using a higher reaction temperature for the samples obtained by using a ratio of metal chlorides to $NaBH_4$ as 1:6 (S3@850 and S3@900). On the other hand, some measured average particle sizes of the powders synthesized at the same temperature showed no obvious change, like in the samples S3@850 (68.2 nm) and S4@850 (62.4 nm). This is seen convenient for a comparison of the catalytic performances of the metal boride composites to see the sole effect of different phases on the hydrogen production. Finally, the analysis results showed that the as-prepared catalysts are in high-purity and consisting of nano-size particles with similar morphology and uniform distribution.

(a)

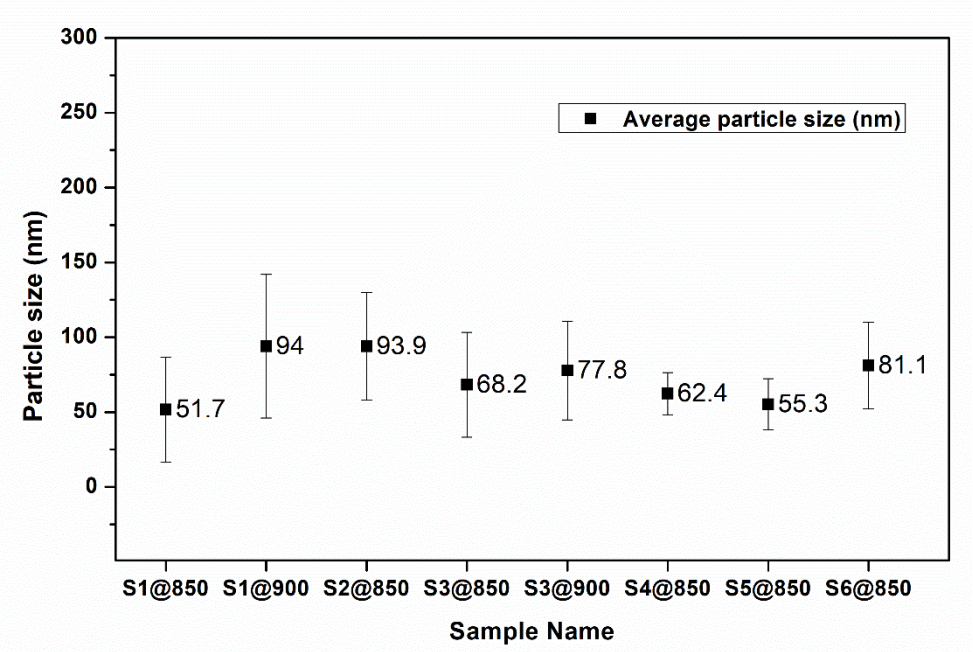
Average particle size (nm)
Particle size (nm)
300
250
200
150
100
50
0
51.7
94
93.9
68.2
77.8
62.4
55.3
81.1
S1@850
S1@900
S2@850
S3@850
S3@900
S4@850
S5@850
S6@850
Sample Name

(b)

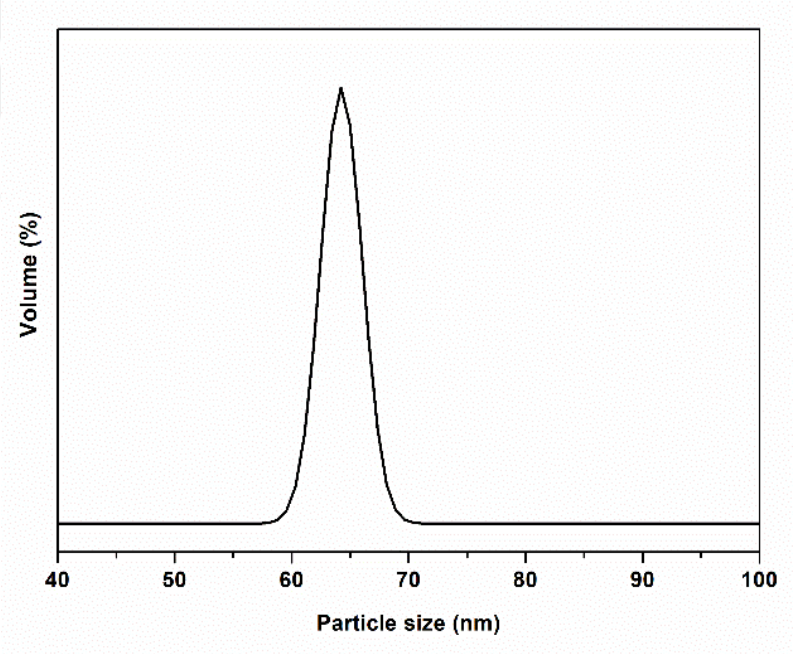
Volume (%)
40
50
60
70
80
90
100
Particle size (nm)

(c)

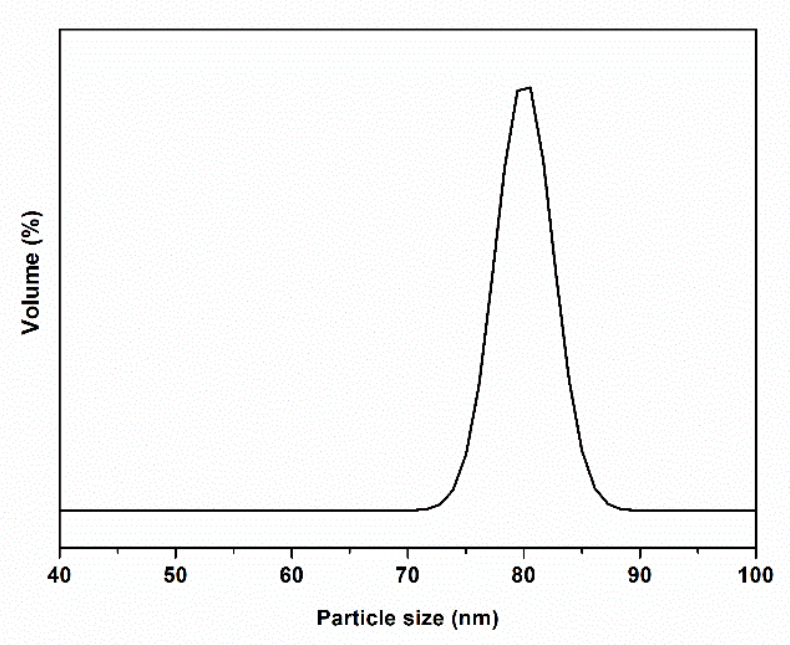

Figure 4.27 (a) Average particle size comparison of all Co–Ni–B, Co–B and Ni–B catalysts, derived from FE-SEM analysis (error bars indicate the standard deviation of twenty measurements) and representative size distribution graphs of (b) S4@850 and (c) S6@850 derived from DLS particle size analysis.

4.2.3 Catalytic Performance Measurements

Figure 4.28 shows the evolution of equivalent hydrogen per mole of $NaBH_4$ versus time plot for the hydrolysis of $NaBH_4$ solution in the presence of different Co–Ni–B catalysts at 25°C. For all catalysts, the amount of hydrogen produced is almost directly proportional to the reaction time, which indicates the stable catalytic activity of the catalysts. The data in Figure 4.28 show that the S4@850 catalyst with CoB–Ni_4B_3 phases showed the highest catalytic activity. Among the as-prepared catalysts, the powder containing the single Ni_4B_3 phase (S6@850) showed no catalytic activity and therefore, it is not included in the graph in Figure 4.28. Such was the case for the commercial cobalt boride powder (CP), which had no catalytic activity as well. Furthermore, it is seen that the S5@850 catalyst containing the single CoB phase showed lower catalytic activity compared to the other catalysts. It is interesting to note that as these catalysts including the Ni_4B_3 phase or CP showed no catalytic activity alone, the powders with different boride phases together or with ternary boride compound including the CoB-Ni_4B_3 and $Ni_2Co_{0.67}B_{0.33}$ showed very high activities. Thus, synergetic effect of the CoB and Ni_4B_3

crystalline phases in Co–Ni–B based catalyst is able to significantly increase the catalytic activity and decrease the reaction time, as compared to those obtained with CoB or Ni_4B_3 phases alone. Similar findings were reported for the amorphous phases, where the Co–Ni–B system provided higher activity compared to CoB or NiB alone for hydrogen production by $NaBH_4$ [15], [53], [95]. In another study, Raney catalysts obtained by the alloying of Raney Ni and Raney Co provided enhanced performance for $NaBH_4$ hydrolysis compared to only Ni or Co [61]. Comparing all the catalysts investigated in this study, S4@850 and S3@850 catalysts containing the CoB–Ni_4B_3 and CoB–Ni_4B_3–NiB phases, respectively, demonstrated the highest catalytic performance under the same conditions at 25°C.

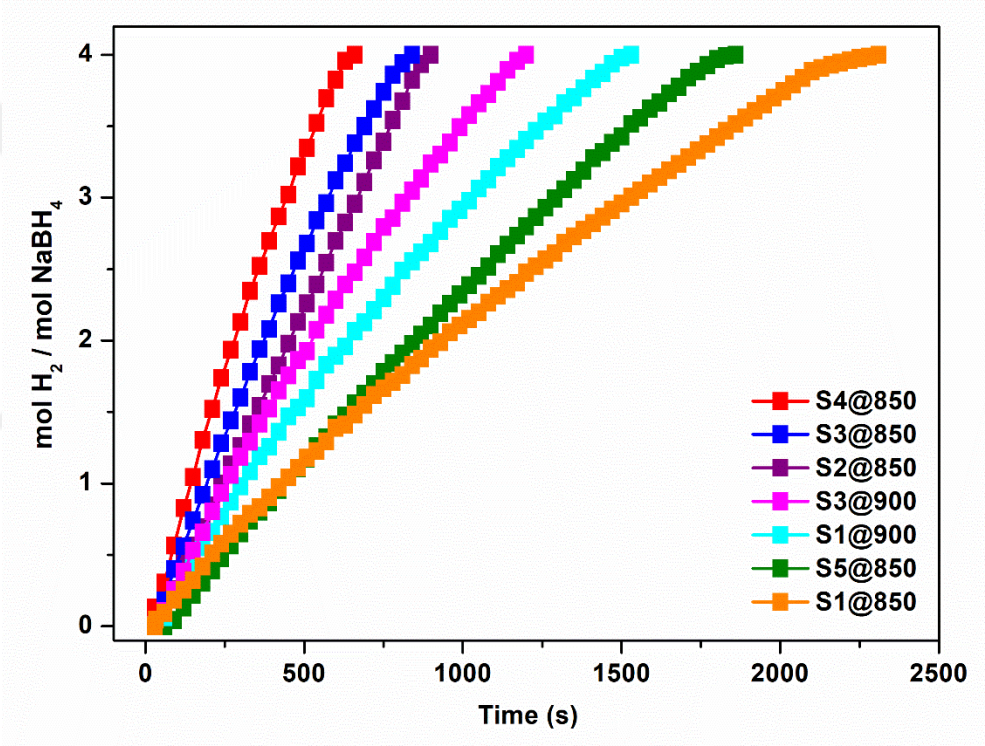

Figure 4.28 The evolution of equivalent hydrogen per mole of $NaBH_4$ versus time plot for the hydrolysis of 5 mL of 0.2 M $NaBH_4$ containing 10 mmol NaOH in the presence of different catalysts (20 mg) at 25 °C.

Figure 4.29 shows the effect of binary and composite boride catalysts on the hydrogen generation rate from $NaBH_4$ solution. To obtain the data presented in Figure 4.29, hydrogen production rates were calculated based on the graphs of hydrogen production volume versus time (min) and the unit of catalyst amount (g); and so the hydrogen production rate was reported in ml H_2 min^{-1} g_{cat}^{-1}. It is known that the alkaline $NaBH_4$ solution is highly stable at high pH values [66]. In recent experimental studies, it

has been determined that with the use of a suitable catalyst, hydrogen can be produced from sodium borohydride even in environments with a pH value greater than 11 [96]. As can be clearly seen from the comparison of values in Figure 4.29, the catalysts containing the CoB–Ni_4B_3 and CoB–Ni_4B_3–NiB phases that were used during the hydrolysis of $NaBH_4$ had provided an important catalytic activity advantage in the rate of hydrogen production (500.0 and 404.6 ml H_2 min^{-1} g_{cat}^{-1}, respectively) compared to all other powders. According to Figures 4.28 and 4.29, one can see that the catalysts containing the Ni_4B_3 phase (S4@850 and S3@850) provides enhanced hydrogen production rates compared to the NiB containing samples (S1@850, S1@900, S2@850). S3@900, containing the dominant NiB phase with slight amount of Ni_4B_3 (Figure 4.20(b)), provided lower catalytic performance compared to the catalysts containing only Ni_4B_3, as well (Figure 4.29). The presence of Ni plays an important role as it is proposed by Guo and coworkers [97]. The presence of well-dispersed Ni sites with an optimal content was found to prompt hydrogen spillover from the surface thereby hindering H_2 agglomeration and coverage on the active Co sites [97]. Based on our findings the Ni-rich phase, Ni_4B_3, act as a better promoter than NiB. Thus, using a mole ratio of metal chlorides to $NaBH_4$ of 1:6 during the synthesis seems more desirable (Table 4.3). When comparing the best performing catalysts containing the Ni_4B_3 phase (S4@850 and S3@850), the existence of NiB phase in the S3@850 sample seem to reduce the catalytic performance. Because the average particle sizes (68.2 and 62.4 nm) and purities of these catalysts (impurities ≤0.9 and 1.1 wt. %) are comparable to each other (Figure 4.27(a) and Table 4.3), the type of formed crystalline phases are the main influential fact of the H_2 generation rates. Slightly lower particle size of S4@850 (62.4 nm) than S3@850 (68.2 nm) might also contribute to the enhancement of the catalytic performance. On the other hand, S1@850 which has the Co_2B phase provided the lowest activity. The presence of Co_2B phase in the structure of the catalyst might decrease chemical stability of the composite borides because of low stability of the metal-rich boride compound of Co–B system. Given the higher hydrogen production rate of 246.4 ml H_2 min^{-1} g_{cat}^{-1} of the S1@900 sample containing the CoB–NiB phases supports this claim, even though this sample has a twice higher particle size compared to S1@850 (Figure 4.27(a)). It is worth to mention here that the CP catalyst containing the Co_2B–Co_3B phases did not present a catalytic activity. This indicates that the metal rich cobalt boride compounds with low chemical stability are not efficient to be used as catalysts in the present system. Figure 4.29 clearly demonstrates also the difference between the composite and binary metal boride catalysts,

where binary boride catalysts give either very low rate or do not give an activity. It is widely known that the regular Co–B systems provide low surface area, poor thermal stability and broadly distributed particle size [95]. Fernandes and coworkers determined that mixed Co–Ni together with B atoms performs much better as the electron density over the metals are enriched by the electron transfer from B. It was found that the Co and Ni metals exchange electrons much easier in the Co–Ni–B system, compared to the Co–B and Ni–B catalysts [15]. It was also reported that the mole ratio of Co/(Co+Ni) in the amorphous catalyst powders highly affected the hydrogen production rates [15]. In our findings however, the alterations in catalytic performances can be directly related to the existing crystalline phases in the catalyst structures, since the Co/(Co+Ni) mole ratios are the same as 0.5 for all catalysts (Table 4.3). Furthermore, the addition of Ni to Co–B catalyst was found to enhance the stability of the final catalyst [98]. In addition to the obtained phases, the nanocrystalline character of the as-prepared catalysts (Figures 4.19-4.27) has also a positive effect on the achieved hydrogen production rates. It is a known method to reduce sizes of the particles used as catalyst in order to accelerate the hydrolysis of $NaBH_4$ due to the higher surface area thereby increasing the number of active sites [97]. Based on the obtained results in this study, the authors validate the claim that catalysts with a fine and uniform particle size, exhibit increased hydrogen generation rates [99]. The inorganic molten salt technique as a low-cost and simple synthesis method in this study makes it possible for the preparation of the nanocrystalline catalysts.

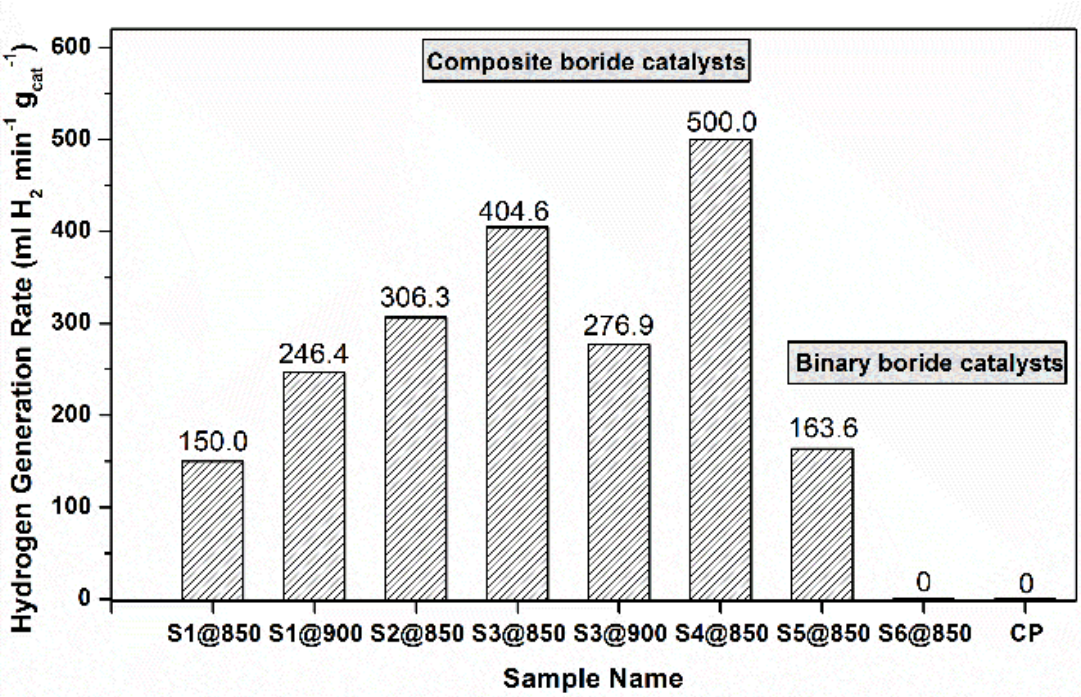

Figure 4.29 Effect of binary and composite boride catalysts on the hydrogen generation rate from $NaBH_4$ solution. (Hydrolysis conditions: 5 mL of 0.2 M $NaBH_4$ containing 10 mmol NaOH in the presence of different Co–Ni–B, Co–B and Ni–B catalysts (20 mg) at 25 °C).

In order to determine the effect of different temperatures on catalytic performance, catalytic hydrolysis of 0.2 M sodium borohydride ($NaBH_4$) was analyzed in the presence of 20 mg S4@850 catalyst at various temperatures (25, 30, 35, 40, and 45°C). Figure 4.26(a) shows the evolution of equivalent hydrogen per mole of $NaBH_4$ versus time plot in the presence of S4@850 catalyst. As seen from Figure 4.30(a), the rate of hydrogen production increased as expected with the increase in temperature. The hydrogen production rates obtained at various temperatures are given in Table 4.4 in ml H_2 min^{-1} g_{cat}^{-1} and it is seen that the hydrogen production rate at 45°C has reached 1257.1 ml H_2 min^{-1} g_{cat}^{-1}. The Arrhenius curve for the activation energy calculation has been extracted and the Arrhenius curve of the hydrogen production rate between 25-45°C is presented in Figure 4.26(b). In the activation energy calculation, the data points closer to the differential conversion region were used. The activation energy (E_a) of $NaBH_4$ hydrolysis reaction can be obtained from the Arrhenius equation given in Equation 2.

Obtained data shows that the hydrolysis obeyed zero-order kinetics as the concentration of $NaBH_4$ shows a linear relation with reaction time at a reaction

temperature of 25°C. The reaction kinetics of $NaBH_4$ is previously stated under *3.3 Hydrolysis of $NaBH_4$* section. Rate of the hydrogen generation was determined as zero-order for S4@850 as shown in Appendix (Figure A.6), comparing data in the zero-, first-, and second-order reaction kinetic models. According to Appendix (Figure A.7), data shows that the hydrolysis obeyed zero-order kinetics as the concentration of $NaBH_4$ shows a linear relation with reaction time at a reaction temperature of 25°C. The activation energy for $NaBH_4$ hydrolysis as catalyzed by S4@850 sample was calculated as 32.7 kJ/mol from the slope of the graph in Figure 4.30(b), which has been created using the zero-order rate constants provided in Appendix (Table A.6). Rate constant were determined using the slope of the zero-order reaction kinetic models at 25, 30, 35, 40, 45 °C (Figure A.4 and A.5).

(a)

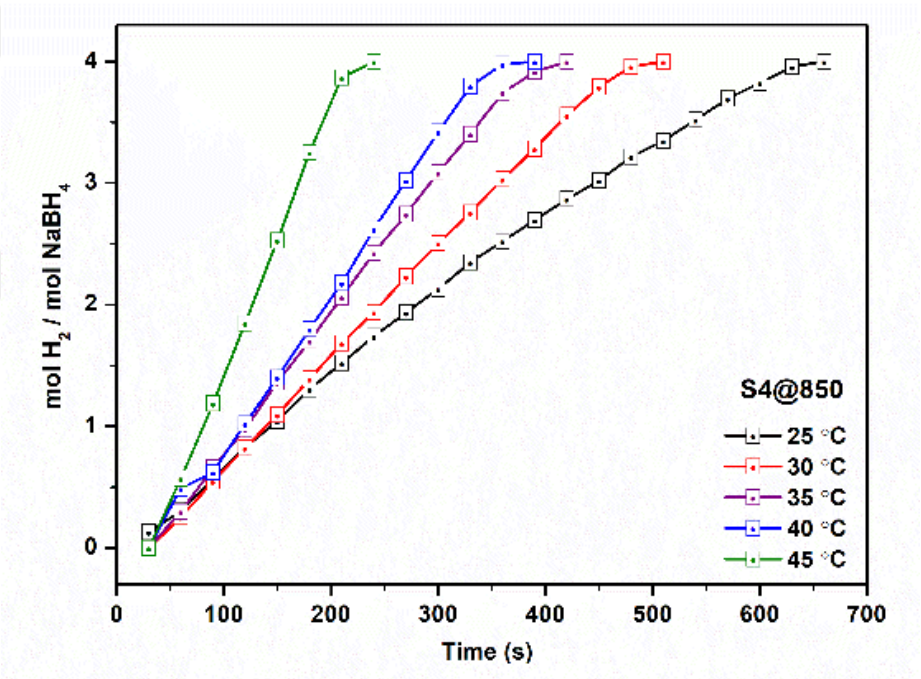

(b)

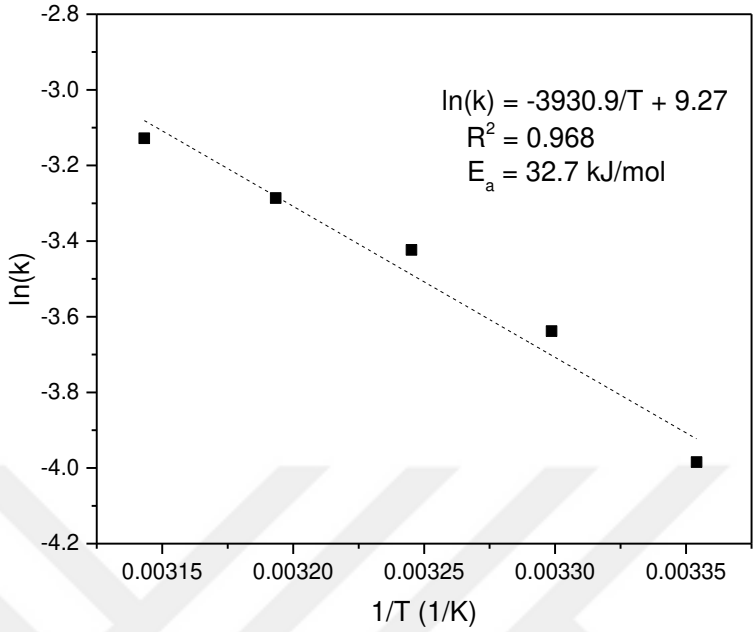

Figure 4.30 The evolution of equivalent hydrogen per mole of $NaBH_4$ versus time plot in the presence of S4@850 catalyst: (a) at different temperatures and (b) the corresponding Arrhenius plot (Hydrolysis conditions: 5 mL of 0.2 M $NaBH_4$ containing 10 mmol NaOH in the presence of 20 mg of the catalyst).

Table 4.4 Hydrogen generation rates at five different temperatures by hydrolysis of $NaBH_4$ solution in the presence of S4@850 catalyst and calculated activation energy value. (Hydrolysis conditions: 5 mL of 0.2 M $NaBH_4$ containing 10 mmol NaOH in the presence of 20 mg of the catalyst)

Catalyst Powder	Hydrolysis exp. temperature (°C)	Hydrogen generation rate (ml H_2 min^{-1} g_{cat}^{-1})	Activation energy (kJ/mol)
S4@850 ($CoB–Ni_4B_3$)	25	500.0	32.7
	30	600.0	
	35	733.3	
	40	777.3	
	45	1257.1	

Table 2.1 displays the hydrogen generation rates and calculated activation energy values for the hydrolysis of $NaBH_4$, as catalyzed by various reported catalysts. It is well

known that the NaOH and $NaBH_4$ concentrations considerably affect the hydrolysis rates [45], [76], [97], [100], [101]. Since sodium borohydride is used here as a source of hydrogen, the increase in the amount of hydrogen with the increase wt. % of $NaBH_4$ is an expected result. Moreover, optimizing the basicity of the hydrolysis solution also promotes hydrogen generation. The Cl impurities remaining in the catalyst (Table 4.3) material also have an effect of reducing the hydrogen generation rate. On the other hand, the obtained activation energy value of the $NaBH_4$ hydrolysis reaction as catalyzed by S4@850 sample (32.7 kJ/mol) is obviously lower than that of previously reported catalysts, whose activation values were reported as 57.8, 72.5, 45, 42.8 kJ/mol [8,9,18,49]. As seen from Table 2.1, only carbon-supported boride catalyst showed a low activation energy value (23.5 kJ/mol), because of its well-dispersed characteristics having more active sites (due to the CNTs promoters) and hence accelerating the hydrolysis [55].The activation energy value obtained in the present study is still lowest among those reported in the literature despite that any supporting or coating material was not used here. This result may be related to the fine distribution and homogeneous microstructure of the S4@850 sample (Figures 4.19 and 4.24), the Ni-rich phase Ni_4B_3 and the absence of Co_2B, thanks to the synthesis method used in this study. Further effect of the surface properties and coating conditions of the composite boride catalysts on the hydrogen generation would be interesting to study in the future. It is interesting to note that the studies on the performances of Co–Ni–B or Co–B catalysts for $NaBH_4$ hydrolysis is very limited (as listed in Table 2.1) and all the catalysts powders are in amorphous phase, except for the reports by Wei et al [47], and our study. Thus, it is thought that the achievement of activation energy value lower than those of Co–Ni–B based powders that are reported in the literature is related to the presence of non-amorphous, nanocrystalline and highly chemically stable metal boride compounds in the structure of the synthesized catalyst [102]. As suggested by Gupta et al., even though it is widely accepted that completely crystalline phases of metal boride are less active than their amorphous counterparts for the electrochemical water splitting, tailoring the crystalline metal borides so that more active sites are exposed to the reactants can be promising [103]. Here we showed that, the crystalline metal borides provide favorable performance with amorphous counterparts for $NaBH_4$ hydrolysis (Table 2.1), thereby creating new opportunities for the utilization of these nanocrystalline metal borides.

Recyclability tests were performed for the best performing catalyst (S4@850) to ensure that S4@850 maintains its catalytic performance after various cycles. A standard

experiment was performed as the first cycle at room temperature. After assuring the hydrolysis of $NaBH_4$ completely, the same amount of $NaBH_4$ was added at each cycle to remeasure the activity of the catalyst powder at identical conditions. Figure 4.31 shows that the performance of S4@850 relatively decreases; however, the catalytic activity is retained even after multiple cycles. Furthermore, the performance does not change after the 4th cycle as illustrated in Figure 4.31.

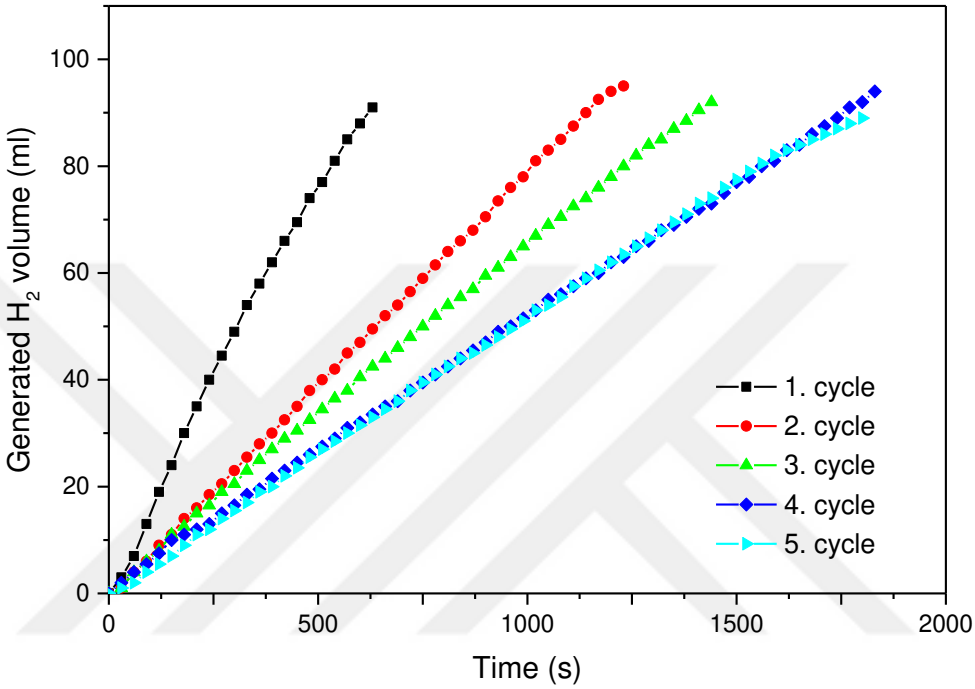

Figure 4.31 Evolution of hydrogen (mL) versus time plot for S4@850 showing the recyclability of the catalyst for 5 cycles. (Hydrolysis conditions for each cycle: 5 mL of 0.2 M $NaBH_4$ containing 10 mmol NaOH in the presence of 20 mg of the catalyst).

Consequently, Co–Ni–B based nanocrystalline powders as synthesized within the scope of this study are materials that are very suitable for use as catalysts of low activation energy in $NaBH_4$ hydrolysis. It has been concluded that the nickel-rich crystalline Ni_4B_3 binary metal boride phase that was synthesized as cobalt-nickel-boron based composite powders significantly increase catalytic performance of the $NaBH_4$ hydrolysis for hydrogen production.

In here, it is important to note that The hydrostatic pressure formed due to the presence of the water in the burette, and the vapor pressure of water were neglected and the total pressure of the H_2 collected was assumed constant throughout the experiment at the atmospheric pressure. A comparison of the volume of hydrogen generated by taking these into considerations and by neglecting them is presented in Figure 4.32. According

to Figure 4.32, data show that the error is negligible and that it remained always smaller than the error range of our measurements (±5%). All calculations were performed by considering ideal gas law in this thesis. Besides, any possibility of H_2 lost by its dissolution in water was also neglected.

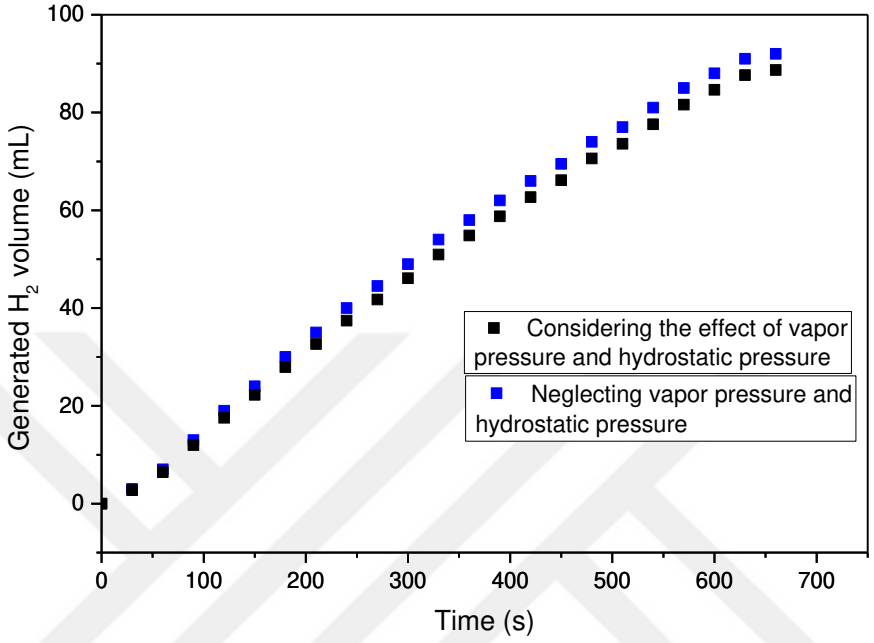

Figure 4.32 Comparison of the generated H_2 volume when considering or neglecting the effect of hydrostatic pressure and water vapor pressure for the representative sample S4@850 at 25 °C. (Hydrolysis conditions: 5 mL of 0.2 M $NaBH_4$ containing 10 mmol NaOH in the presence of 20 mg of catalyst).

Chapter 5:
CONCLUSION

In this thesis, synthesis and characterization studies were carried out to synthesize a suitable catalyst to be used in the hydrolysis reaction of $NaBH_4$. In this direction, transition-metal boride compounds including iron, cobalt and nickel have been examined due to their chemical and economic advantages. The synthesis and results of the two selected systems, Fe–Ni–B and Co–Ni–B, in the thesis study are presented.

Fe–Ni–B containing metal boride nanocatalysts having different compositions (including the semi-crystalline FeB, Fe_3B, Fe_2B, Ni_2B, Ni_3B, Ni_4B_3 phases) were synthesized via a one-step direct reaction of $FeCl_3$–$NiCl_2$–$NaBH_4$ by mechanochemical synthesis followed by a wet milling step. This ternary system resulted in mixed compositions containing different binary compounds. It has been determined that the obtained phases become pure with the increase of the mole ratio of boron in the composition. All of the catalysts prepared according to the results of the analyses have a particle size of 40-100 nanometers. It has been determined that the catalyst with pure FeB-Ni_3B phases exhibits the best performance and the reason for this is the consistency of the metal boride phases in its content. This determination was supported by XPS analysis, where the surface Fe, Ni and B moieties were clearly observed. XPS data further indicated that nickel enriched and iron enriched active sites were formed as a result of the electron transfer of boron to nickel and iron. Furthermore, according to the BET analysis, the best performing powder has the greatest surface area, with a value of 41.8 m^2/g. This aspect contributed to the increase in activity as well. The catalyst powder, which reduced the activation energy of the hydrolysis reaction of $NaBH_4$ to 40.8 kJ/mol, was the powder in which the most hydrogen was obtained, with an HGR value of 758 $ml.min^{-1}.g^{-1}$ at room temperature. In addition, it remained stable in the cycle tests and successfully completed the hydrolysis reaction. In summary, metal boride containing nanopowders are suitable catalyst alternatives for highly efficient sodium borohydride hydrolysis reaction, as high-performance, recyclable and low-cost materials.

Co–Ni–B containing metal boride composite nanocatalysts having different compositions (including the crystalline CoB, Co_2B, Co_5B_{16}, NiB, Ni_4B_3, and $Ni_2Co_{0.67}B_{0.33}$ phases) were synthesized via a one-step direct reaction of $CoCl_2$–$NiCl_2$–

$NaBH_4$ in an inorganic molten salt environment. The obtained compositions were varied by changing the mole ratio of metal chlorides to sodium borohydride as 1:3/1:6 and the reaction temperature as 850/950°C. The reactions for binary systems of $CoCl_2$–$NaBH_4$ and $NiCl_2$–$NaBH_4$ respectively resulted in pure crystalline CoB and Ni_4B_3 formation, whereas the reactions in $CoCl_2$–$NiCl_2$–$NaBH_4$ ternary system resulted in mixed compositions containing different binary and ternary compounds. Analyses of the powders illustrated that all the as-prepared catalysts are in high-purity with average particle sizes ranging in ~51 to 94 nm and consisting of nanocrystalline phases. Catalytic performance tests showed that the existence of nickel rich Ni_4B_3 crystalline phase in the composite catalyst and the synergetic effect of the different cobalt and nickel boride phases had a positive role on the enhancement of catalytic activities. The composite catalyst containing the CoB–Ni_4B_3 phases exhibited the highest H_2 production rate (500.0 $ml.min^{-1}.g^{-1}$), whereas the Co–B and Ni–B based catalysts containing the crystalline phases of unstable cobalt borides or single Ni_4B_3 did not show any catalytic activity. The activation energy of the best performing catalyst (CoB–Ni_4B_3) was calculated as 32.7 kJ/mol, which is remarkably lower than those of many other Co–Ni–B based catalysts reported in the literature. Recyclability tests were also executed on the best performing catalyst. In these tests carried out under room temperature, it was observed that the powder did not lose its catalytic activity despite multiple cycles. Even though the cycle number was increased, the stability of the catalyst was not impaired. In summary, it was shown that metal boride composites in nanocrystalline structure can be used as alternative and stable catalysts for highly efficient hydrogen production from the hydrolysis of sodium borohydride.

When the two systems are compared, the semi-crystalline structure formed in the Fe–Ni–B system increases catalytic activity, whereas the Co–Ni–B system achieves high catalytic activity in the nanocrystalline structure. For both systems, small particle size, spherical morphology, and regular distribution are crucial elements for observing high catalytic activity. Optimum powders with these qualities could be produced using the designed synthesis methods. Furthermore, the presence of active sites is the most significant factor for catalytic activity, and the presence of active sites for both systems, as well as their favorable effects on activity, could be highlighted in the studies.

BIBLIOGRAPHY

[1] D. Welsby, J. Price, S. Pye, and P. Ekins, “Unextractable fossil fuels in a 1.5°C world,” *Nature*, vol. 597, no. February, 2021.

[2] R. D. Brook *et al.*, “Air Pollution and Cardiovascular Disease,” *AHA Scientific Statement,* pp. 2655–2671, 2004.

[3] G. A. O. Lijie, Z. Meigen, and H. A. N. Zhiwei, “Model Analysis of Seasonal Variations in Tropospheric Ozone and Carbon Monoxide over East Asia,” *Advances in Atmospheric Sciences*, vol. 26, no. 2, pp. 312–318, 2009.

[4] Ü. Ağbulut and S. Sarıdemir, “A general view to converting fossil fuels to cleaner energy source by adding nanoparticles,” *Int. J. Ambient Energy*, vol. 42, no. 13, pp. 1569–1574, 2021.

[5] L. R. Khanal, J. A. Sundararajan, and Y. Qiang, “Advanced Nanomaterials for Nuclear Energy and Nano - Technology.” *ACS Sustain. Chem. Eng.*, 6, 2018

[6] M. H. Ahmadi, “Renewable energy harvesting with the application of nanotechnology : A review,” *Int. J. Energy Res.*, pp. 1–24, 2018.

[7] M. Momirlan and T. N. Veziroglu, “Current status of hydrogen energy,” vol. 6, pp. 141–179, 2002.

[8] L. Schlapbach and A. Züttel, “for mobile applications,” *Renewable & Sustainable Energy Reviews*, vol. 414, pp. 353–358, 2001.

[9] N. P. Ghodke, S. Rayaprol, S. V. Bhoraskar, and V. L. Mathe, “Catalytic hydrolysis of sodium borohydride solution for hydrogen production using thermal plasma synthesized nickel nanoparticles,” *Int. J. Hydrogen Energy*, vol. 45, no. 33, pp. 16591–16605, 2020.

[10] S. C. Amendola *et al.*, “A Safe, portable, hydrogen gas generator using aqueous borohydride solution and Ru catalyst,” *Int. J. Hydrogen Energy*, vol. 25, no. 10, pp. 969–975, 2000.

[11] A. Züttel, P. Wenger, S. Rentsch, P. Sudan, P. Mauron, and C. Emmenegger, “$LiBH_4$ a new hydrogen storage material,” *J. Power Sources*, vol. 118, no. 1–2, pp. 1–7, 2003.

[12] Y. Kojima *et al.*, “Hydrogen generation using sodium borohydride solution and metal catalyst coated on metal oxide,” *Int. J. Hydrogen Energy*, vol. 27, no. 10, pp. 1029–1034, 2002.

[13] M. A. M. Luengo and P. A. Sermon, “Experiments Illustrating Heterogeneous Catalysis,” *Journal of Chemical Education*, vol. 68, no. 3, pp. 3–5, 1991.

[14] J. Zhao, H. Ma, and J. Chen, “Improved hydrogen generation from alkaline $NaBH_4$ solution using carbon-supported Co-B as catalysts,” *Int. J. Hydrogen Energy*, vol. 32, no. 18, pp. 4711–4716, 2007.

[15] R. Fernandes, N. Patel, A. Miotello, and M. Filippi, “Studies on catalytic behavior of Co-Ni-B in hydrogen production by hydrolysis of $NaBH_4$,” *J. Mol. Catal. A Chem.*, vol. 298, no. 1–2, pp. 1–6, 2009.

[16] B. A. Yusuf, Y. Xu, N. Ullah, and M. Xie, “B-Doped carbon enclosed nickel nanoparticles: a robust, stable and efficient electrocatalyst for hydrogen evolution reaction,” *J. Electroanal. Chem.*, 2020.

[17] H. Maryon *et al.*, “Early Near Eastern Steel Swords,” *American Journal of Archaeology,* vol. 65, no. 2, pp. 173–184, 2013.

[18] A. Montecucco, J. R. Buckle, and A. R. Knox, “Solution to the 1-D unsteady heat conduction equation with internal Joule heat generation for thermoelectric devices,” *Appl. Therm. Eng.*, vol. 35, no. 1, pp. 177–184, 2012.

[19] C. E. Housecroft and A. G. Sharpe, *Inorganic Chemistry*, Fourth Edition, Pearson, 2012.

[20] A. L. Ivanovskii, “Progress in Materials Science Mechanical and electronic properties of diborides of transition 3d–5d metals from first principles: Toward search of novel ultra-incompressible and superhard materials,” *Prog. Mater. Sci.*, vol. 57, no. 1, pp. 184–228, 2012.

[21] F. Habashi, “*Handbook of extractive metallurgy*” Wiley, 1997.

[22] T. Materials and I. Company, “Properties and Selection: Nonferrous Alloys and Special-Purpose Materials” *The Materials Information Company*, 1992.

[23] M. Usta, I. Ozbek, C. Bindal, A. Hikmet, S. Ingole, and H. Liang, “A comparative study of borided pure niobium , tungsten and chromium,” vol. 80, pp. 1321–1325, 2006.

[24] B. T. Matthias T. H. Geballe K. et. al. “Superconductivity and antiferromagnetism in boron-rich lattices” *Science*, vol. 159, 1968.

[25] J. F. Herbest, J. J. Croat, F. E. Pinkerton, “Relationships between crystal structure and magnetic properties in $Nd_2Fe_{14}B$” *Physical Review B*, vol. 29, no. 7, pp. 7–9, 1984.

[26] B. Y. Clara, B. Srioemai, and D. P. Sroemaker, “The Structure of a New Magnetic

Phase Related to the Sigma Phase : Iron Neodymium Boride Nd_2Fe_{14} B," no. 010, pp. 2–5, 1984.

[27] M. M. Opeka, I. G. Talmy, J. A. Zaykoski, N. Surface, C. Division, and W. Bethesda, "Oxidation-based materials selection for 2000°C hypersonic aerosurfaces : Theoretical," vol. 9, pp. 5887–5904, 2004.

[28] C. Saiyasombat, N. Petchsang, I. M. Tang, and J. H. Hodak, "Preparation of iron boride–silica core–shell nanoparticles with soft ferromagnetic properties," *Nanotechnology*, 19, 2008.

[29] P. K. Deheri, S. Shukla, and R. V Ramanujan, "The reaction mechanism of formation of chemically synthesized $Nd_2Fe_{14}B$ hard magnetic nanoparticles," *J. Solid State Chem.*, vol. 186, pp. 224–230, 2012.

[30] S. L. Bud, G. Lapertot, C. Petrovic, C. E. Cunningham, N. Anderson, and P. C. Canfield, "Boron Isotope Effect in Superconducting MgB_2," pp. 1877–1880, 2001.

[31] J. E. Kunzler, E. Buehler, "Superconductivity in Nb_3Sn at high current density," *Physical review letters*, vol. 6, no. 3, pp. 3–5, 1961. .

[32] Z. Chen, Q. Kang, G. Cao, N. Xu, H. Dai, and P. Wang, "Study of cobalt boride-derived electrocatalysts for overall water splitting," *Int. J. Hydrogen Energy*, vol. 43, no. 12, pp. 6076–6087, 2018.

[33] T. Zell and R. Langer, "Iron-catalyzed hydrogenation and dehydrogenation reactions with relevance to reversible hydrogen storage applications," pp. 87–109, 2015.

[34] J. Miettinen and G. P. Vassilev, "Thermodynamic description of ternary Fe-B-X Systems. Part 2: Fe-B-Ni," no. November, 2015.

[35] K. Narasimhan, F. J. Semel, and S. Scientist, "Sintering Of Powder Premixes - A Brief Overview Sintering Of Powder Premixes–A Brief Overview," no. March, 2019..

[36] C. Nickel and B. Superalloy, "Research on Interlayer Alloys for Transient Liquid Phase Diffusion Bonding of Single," *Scientific Research*, pp. 12–19, 2014.

[37] Y. A. Knutskii, E. V. Marek, "Some physical properties of iron boride," vol. 3, no. 3, pp. 216–218, 1971.

[38] M. Nie, Y. C. Zou, Y. M. Huang, and J. Q. Wang, "Ni–Fe–B catalysts for $NaBH_4$ hydrolysis," *Int. J. Hydrogen Energy*, vol. 7, pp. 2–10, 2011.

[39] Y. N. Regmi *et al.*, "Catalytic transfer hydrogenolysis of organosolv lignin using B-containing FeNi alloyed catalysts," *Catalysis Today*, pp. 5–10, 2017.

[40] Z. Liang, Q. Li, F. Li, S. Zhao, and X. Xia, "Hydrogen generation from hydrolysis of $NaBH_4$ based on high stable NiB / $NiFe_2O_4$ catalyst," *Int. J. Hydrogen Energy*, vol. 42, no. 7, pp. 3971–3980, 2016.

[41] Y. Zhao *et al.*, "A synergistic effect between nanoconfinement of carbon aerogels and catalysis of CoNiB nanoparticles on dehydrogenation of $LiBH_4$," *Int. J. Hydrogen Energy*, vol. 39, no. 2, pp. 917–926, 2014.

[42] L. Li, Y. J. Wang, Y. P. Wang, Q. L. Ren, L. F. Jiao, and H. T. Yuan, "Effect of Ni content in $Co_{1-x}Ni_xB$ catalysts on hydrogen generation during hydrolysis," *Wuli Huaxue Xuebao/ Acta Phys. - Chim. Sin.*, vol. 26, no. 6, pp. 1575–1578, 2010.

[43] D. Xu, H. Wang, Q. Guo, and S. Ji, "Catalytic behavior of carbon supported Ni-B, Co-B and Co-Ni-B in hydrogen generation by hydrolysis of KBH_4," *Fuel Process. Technol.*, vol. 92, no. 8, pp. 1606–1610, 2011.

[44] H. Li, Y. Wu, J. Zhang, W. Dai, and M. Qiao, "Liquid phase acetonitrile hydrogenation to ethylamine over a highly active and selective Ni-Co-B amorphous alloy catalyst," *Appl. Catal. A Gen.*, vol. 275, no. 1–2, pp. 199–206, 2004.

[45] G. Bozkurt, A. Özer, and A. B. Yurtcan, "Hydrogen generation from sodium borohydride with Ni and Co based catalysts supported on Co_3O_4," *Int. J. Hydrogen Energy*, vol. 43, no. 49, pp. 22205–22214, 2018.

[46] S. Qiu *et al.*, "Ternary Co–Ni–B amorphous alloy with a superior electrochemical performance in a wide temperature range," *Int. J. Hydrogen Energy*, vol. 41, no. 6, pp. 3955–3960, 2016.

[47] Y. Wei, W. Meng, Y. Wang, Y. Gao, K. Qi, and K. Zhang, "Fast hydrogen generation from $NaBH_4$ hydrolysis catalyzed by nanostructured Co–Ni–B catalysts," *Int. J. Hydrogen Energy*, vol. 42, no. 9, pp. 6072–6079, 2017.

[48] J. Wisniak, "The History of Catalysis . From the Beginning to Nobel Prizes," *Educ. Química*, vol. 21, no. 1, pp. 60–69, 2017.

[49] J. M. Basset, J. P. Candy, C. C. Santiniü, "Supported Transition Metals Catalysis", *Transition Metals for Organic Synthesis*, Wiley, 1998.

[50] I. Union, O. F. Pure, and A. Chemistry, "Commission On Chemical Kinetics * A Glossary Of Terms Used In Chemical Kinetics , Including Reaction Dynamics," vol. 68, no. 1, pp. 149–192, 1996.

[51] P. Munnik, P. E. De Jongh, and K. P. De Jong, "Recent Developments in the Synthesis of Supported Catalysts," 2014.

[52] C. Wang, X. Wang, "Ultrathin Amorphous Iron-nickel Boride Nanosheets for Highly Efficient Electrocatalytic Oxygen Production," *E. Electrocatalytic*, 2018

[53] N. Patel, R. Fernandes, and A. Miotello, "Promoting effect of transition metal-doped Co-B alloy catalysts for hydrogen production by hydrolysis of alkaline $NaBH_4$ solution," *J. Catal.*, vol. 271, no. 2, pp. 315–324, 2010.

[54] N. P. Ghodke, S. Rayaprol, S. V Bhoraskar, and V. L. Mathe, "Catalytic hydrolysis of sodium borohydride solution for hydrogen production using thermal plasma synthesized nickel nanoparticles," Int. J. Hydrogen Energy, 2020.

[55] L. Shi, Z. Chen, Z. Jian, F. Guo, and C. Gao, "Carbon nanotubes-promoted Co–B catalysts for rapid hydrogen generation via $NaBH_4$ hydrolysis," *Int. J. Hydrogen Energy*, vol. 44, no. 36, pp. 19868–19877, 2019.

[56] Y. Guo, R. Zhang, W. Hao, J. Zhang, and Y. Yang, "Multifunctional Co–B–O@CoxB catalysts for efficient hydrogen generation," *Int. J. Hydrogen Energy*, vol. 45, no. 1, pp. 380–390, 2020.

[57] C. Kim, S. Soo, W. Li, and J. D. Fortner, "General Towards optimizing cobalt based metal oxide nanocrystals for hydrogen generation via $NaBH_4$ hydrolysis," *Appl. Catal. A, Gen.*, vol. 589, no. October 2019, p. 117303, 2020.

[58] F. Li, J. Li, L. Chen, Y. Dong, P. Xie, and Q. Li, "Hydrogen production through hydrolysis of sodium borohydride: Highly dispersed CoB particles immobilized in carbon nanofibers as a novel catalyst," *Int. J. Hydrogen Energy*, 2020.

[59] F. Wang, Y. Zhang, Y. Wang, Y. Luo, Y. Chen, and H. Zhu, "Co-P nanoparticles supported on dandelion-like CNTs-Ni foam composite carrier as a novel catalyst for hydrogen generation from $NaBH_4$ methanolysis," *Int. J. Hydrogen Energy*, vol. 43, no. 18, pp. 8805–8814, 2018.

[60] Z. Liang, Q. Li, F. Li, S. Zhao, and X. Xia, "Hydrogen generation from hydrolysis of $NaBH_4$ based on high stable $NiB/NiFe_2O_4$ catalyst," *Int. J. Hydrogen Energy*, vol. 42, no. 7, pp. 3971–3980, 2017.

[61] B. H. Liu, Z. P. Li, and S. Suda, "Nickel- and cobalt-based catalysts for hydrogen generation by hydrolysis of borohydride," *J. Alloys Compd.*, vol. 415, no. 1–2, pp. 288–293, 2006.

[62] J. C. Walter, A. Zurawski, D. Montgomery, M. Thornburg, and S. Revankar, "Sodium borohydride hydrolysis kinetics comparison for nickel, cobalt, and ruthenium boride catalysts," *J. Power Sources*, vol. 179, no. 1, pp. 335–339, 2008.

[63] J. Zhang, C. Li, L. Li, X. Du, B. Song, and H. Xu, "Multi-shaped Amorphous Alloy

Ni-B: Ultrasonically Aided Complexing-reduction Preparation , Catalytic Ability for $NaBH_4$ Hydrolysis Yielding H_2 Gas," no. 2, pp. 456–461, 2014.

[64] J. Kwang, H. Ann, Y. Yi, K. Wan, S. Uhm, and J. Lee, "A stable Ni–B catalyst in hydrogen generation via $NaBH_4$ hydrolysis," *Cat. Com.*, vol. 16, no. 1, pp. 120–123, 2011.

[65] L. Wang, M. Zhong, J. Li, X. Zhao, W. Hao, and Y. Guo, "Highly efficient ferromagnetic Co–B–O catalyst for hydrogen generation," *Int. J. Hydrogen Energy*, vol. 43, no. 36, pp. 17164–17171, 2018.

[66] J. C. Ingersoll, N. Mani, J. C. Thenmozhiyal, and A. Muthaiah, "Catalytic hydrolysis of sodium borohydride by a novel nickel-cobalt-boride catalyst," *J. Power Sources*, vol. 173, no. 1, pp. 450–457, 2007.

[67] S. Khoshsima, Z. Altıntaş, U. Burkhardt, M. Schmidt, K.G. Prashanth, M. Somer, Ö. Balcı, "CoB-TiB_2 crystalline powders: Synthesis , microstructural analysis and their utilization as reinforcement agent," vol. 31, pp. 2964–2972, 2020.

[68] S. Khoshsima, Z. Altıntaş, M. Schmidt, M. Bobnar, M. Somer, and Ö. Balcı, "Crystalline Co-Fe-B nanoparticles: Synthesis , microstructure and magnetic properties," vol. 805, 2019.

[69] D. Portehault *et al.*, "A general solution route toward metal boride nanocrystals," *Angew. Chemie - Int. Ed.*, vol. 50, no. 14, pp. 3262–3265, 2011.

[70] G. Gouget *et al.*, "In Situ Solid-Gas Reactivity of Nanoscaled Metal Borides from Molten Salt Synthesis," *Inorg. Chem.*, vol. 56, no. 15, pp. 9225–9234, 2017.

[71] S. Guo *et al.*, "Highly stable and controllable CoB/Ni-foam catalysts for hydrogen generation from alkaline $NaBH_4$ solution," *Int. J. Hydrogen Energy*, vol. 42, no. 33, pp. 21063–21072, 2017.

[72] R. Retnamma, A. Q. Novais, and C. M. Rangel, "Kinetics of hydrolysis of sodium borohydride for hydrogen production in fuel cell applications: A review," *Int. J. Hydrogen Energy*, vol. 36, no. 16, pp. 9772–9790, 2011.

[73] E. B. Kalkan, S. Akbayrak, and S. Özkar, "Ruthenium(0) nanoparticles supported on nanohafnia: A highly active and long-lived catalyst in hydrolytic dehydrogenation of ammonia borane," *Mol. Catal.*, vol. 430, pp. 29–35, 2017.

[74] D. Hua, Y. Hanxi, A. Xinping, and C. Chuansin, "Hydrogen production from catalytic hydrolysis of sodium borohydride solution using nickel boride catalyst," *Int. J. Hydrogen Energy*, vol. 28, no. 10, pp. 1095–1100, 2003.

[75] S. C. Amendola, S. L. Sharp-Goldman, M. S. Janjua, M. T. Kelly, P. J. Petillo, and

M. Binder, “An ultrasafe hydrogen generator: Aqueous, alkaline borohydride solutions and Ru catalyst,” *ACS Div. Fuel Chem. Prepr.*, vol. 44, no. 4, pp. 864–866, 1999.

[76] H. Y. Kao, C. C. Lin, C. J. Hung, and C. C. Hu, “Kinetics of hydrogen generation on $NaBH_4$ powders using cobalt catalysts,” *J. Taiwan Inst. Chem. Eng.*, vol. 87, pp. 123–130, 2018.

[77] Keith J Laidler, “Chemical Kinetics”, Harper Collins, 1987.

[78] L. De Viguerie, V. A. Sole, and P. Walter, “Multilayers quantitative X-ray fluorescence analysis applied to easel paintings,” pp. 2015–2020, 2020.

[79] I. Queralt and J. M. Sampaio, “Accuracy comparison using analytical methodology and Monte Carlo simulations,” vol. 152, no. June, pp. 6–10, 2019.

[80] P. H. Salame, V. B. Pawade, and B. A. Bhanvase, *Chapter 3 - Characterization Tools and Techniques for Nanomaterials*. Elsevier Inc., 2018.

[81] K. D. Parry V, “Scanning Electron Microscopy : An introduction,” *III-Vs Rev.*, vol. 13, no. 4, pp. 40–44, 2000.

[82] “Physical Principle of Electron Microscopy: an introduction,” vol. 13, no. 4, pp. 40–44, 2000.

[83] S. Tougaard and S. Denmark, “X-Ray Photoelectron Spectroscopy,” vol. 1, no. C, p. 2005, 2005.

[84] E. Capabilities, “X-Ray Photoelectron Spectroscopy Applications,” pp. 716–724, 2017.

[85] A. P. Grosvenor, M. C. Biesinger, R. S. C. Smart, and N. S. Mcintyre, “New interpretations of XPS spectra of nickel metal and oxides,” vol. 600, pp. 1771–1779, 2006.

[86] M. C. Biesinger and B. P. Payne, “Resolving surface chemical states in XPS analysis of first row transition metals, oxides and hydroxides: Cr , Mn , Fe , Co and Ni.”

[87] K. Wei, X. Liu, S. Cao, H. Cui, Y. Zhang, and Z. Ai, “Fe_2O_3@FeB composites facilitate heterogeneous Fenton process by efficient Fe(III)/ Fe(II) cycle and in-situ H_2O_2 generation,” *Chem. Eng. J. Adv.*, vol. 8, p. 100165, 2021.

[88] M. Lan, G. Fan, Y. Wang, L. Yang, and F. Li, “Synthesis of highly dispersed boron-promoted nickel nanocatalysts and significantly enhanced catalytic performance in hydrodechlorination of,” *J. Mater. Chem. A Mater. energy Sustain.*, vol. 2, pp. 14682–14689, 2014.

[89] W. Li, S. Wang, et. al. “Direct Aqueous Solution Synthesis of Ultra-fine Amorphous Nickel-Boron Alloy with Superior Pseudocapacitive Performance for Advanced Asymmetric Supercapacitors. ” *New J. Chem.*, 2017.

[90] F. Yang, P. Han, N. Yao, G. Cheng, W. Luo, and S. Chen, “Chemical Science heterostructure for boosting hydrogen electrooxidation in alkaline media,” 2020.

[91] Y. Wang and X. Liu, “Catalytic Hydrolysis of Sodium Borohydride for Hydrogen Production Using Magnetic Recyclable $CoFe_2O_4$-Modified Transition-Metal Nanoparticles,” 2021.

[92] A. Paksoy, S. F. Kurtoğlu, A. K. Dizaji, Z. Altıntaş, S. Khoshsima, A. Uzun, Ö. Balcı, “Nanocrystalline cobalt–nickel–boron (metal boride) catalysts for efficient hydrogen production from the hydrolysis of sodium borohydride,” *Int. J. Hydrogen Energy*, vol. 46, no. 11, pp. 7974–7988, 2021.

[93] Z. Liang, Q. Li, F. Li, S. Zhao, and X. Xia, “Hydrogen generation from hydrolysis of $NaBH_4$ based on high stable $NiB/NiFe_2O_4$ catalyst,” *Int. J. Hydrogen Energy*, pp. 2–11, 2016.

[94] J. Guo *et al.*, “Hierarchically structured rugae-like RuP_3-CoP arrays as robust catalysts synergistically promoting hydrogen generation,” *J. Mater. Chem. A*, vol. 7, no. 15, pp. 8865–8872, 2019.

[95] N. Patel and A. Miotello, “Progress in Co-B related catalyst for hydrogen production by hydrolysis of boron-hydrides: A review and the perspectives to substitute noble metals,” *Int. J. Hydrogen Energy*, vol. 40, no. 3, pp. 1429–1464, 2015.

[96] J. Li *et al.*, “Encapsulated cobalt nanoparticles as a recoverable catalyst for the hydrolysis of sodium borohydride,” *Energy Storage Mater.*, vol. 27, no. November 2019, pp. 187–197, 2020.

[97] J. Guo, Y. Hou, B. Li, and Y. Liu, “Novel Ni–Co–B hollow nanospheres promote hydrogen generation from the hydrolysis of sodium borohydride,” *Int. J. Hydrogen Energy*, vol. 43, no. 32, pp. 15245–15254, 2018.

[98] R. Fernandes, N. Patel, A. Miotello, R. Jaiswal, and D. C. Kothari, “Stability, durability, and reusability studies on transition metal-doped Co-B alloy catalysts for hydrogen production,” *Int. J. Hydrogen Energy*, vol. 36, no. 21, pp. 13379–13391, 2011.

[99] A. Didehban, M. Zabihi, and N. Babajani, “Preparation of the efficient nano-bimetallic cobalt-nickel catalysts supported on the various magnetic substrates for

hydrogen generation from hydrolysis of sodium borohydride in alkaline solutions," *Polyhedron*, vol. 180, p. 114405, 2020.

[100] Y. Wang *et al.*, "Cobalt–copper–boron nanoparticles as catalysts for the efficient hydrolysis of alkaline sodium borohydride solution," *Int. J. Hydrogen Energy*, vol. 45, no. 16, pp. 9845–9853, 2020.

[101] X. Wang *et al.*, "Highly active porous Co–B nanoalloy synthesized on liquid-gas interface for hydrolysis of sodium borohydride," *Int. J. Hydrogen Energy*, vol. 43, no. 37, pp. 17543–17555, 2018.

[102] C. Wu, F. Wu, Y. Bai, B. Yi, and H. Zhang, "Cobalt boride catalysts for hydrogen generation from alkaline $NaBH_4$ solution," *Mater. Lett.*, vol. 59, no. 14–15, pp. 1748–1751, 2005.

[103] S. Gupta, M. K. Patel, A. Miotello, and N. Patel, "Metal Boride-Based Catalysts for Electrochemical Water-Splitting: A Review," *Adv. Funct. Mater.*, vol. 30, no. 1, 2020.

APPENDIX

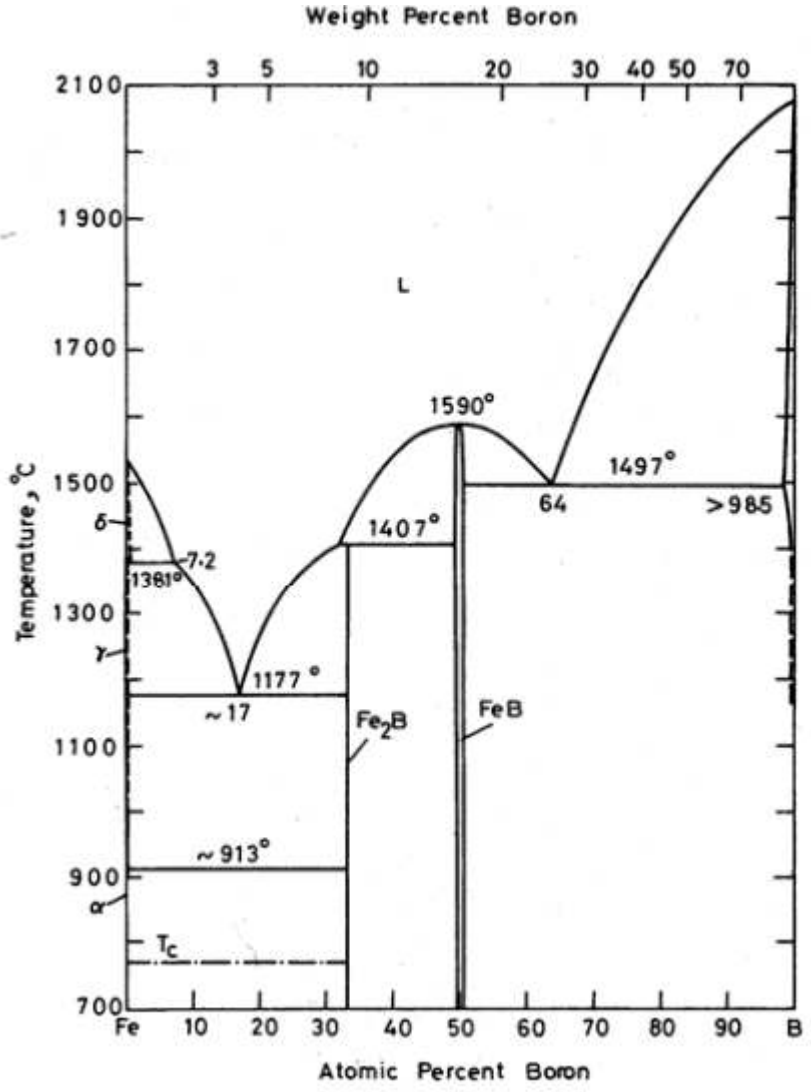

Figure A.1 Binary phase diagram of Fe-B, adapted from [35].

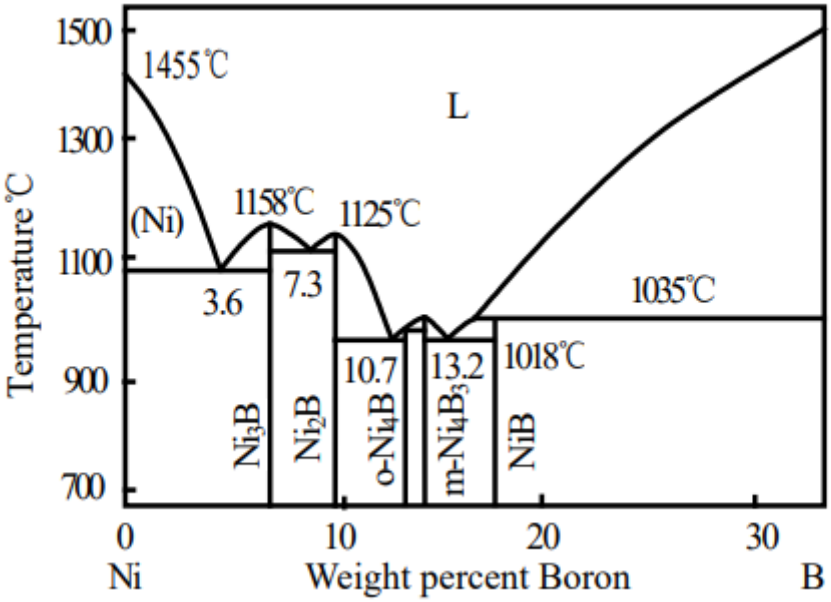

Figure A.2 Binary phase diagram Ni-B, adapted from [36].

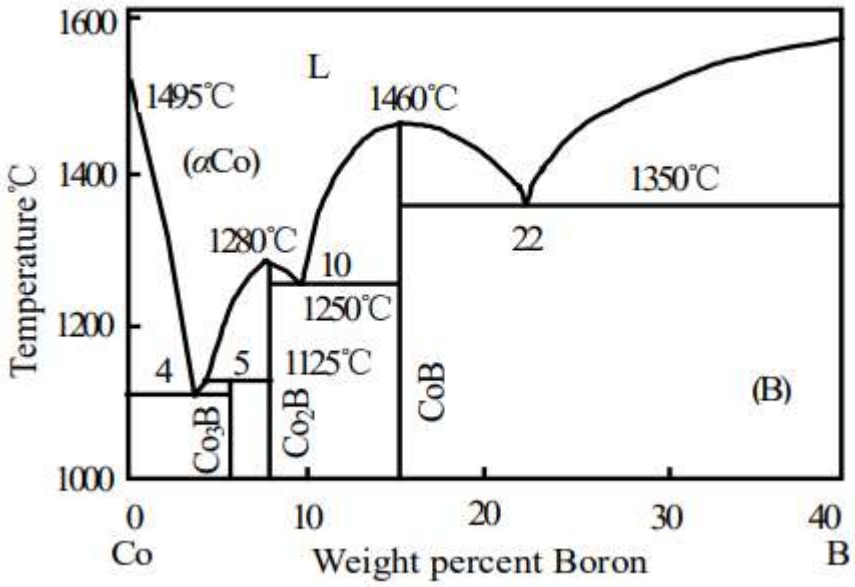

Figure A.3 Binary phase diagram of Co-B, adapted from [36].

Table A.1 COD Card numbers and theoretical lattice parameters (Å, Angstrom) for the obtained phases in A1@1, A1@2, A2@1, A2@2, A3@1, A3@2, A4@1 and A4@2

Phase	Crystal structure	COD Card Number	a	b	c
NiO	Cubic	4329325	4.17	4.17	4.17
Ni_2B	Tetragonal	1511265	5.01	5.01	4.22
Ni_3B	Orthorhombic	8102955	5.22	6.61	4.39
FeB	Orthorhombic	9008944	4.05	5.49	2.94
Ni_4B_3	Orthorhombic	1510943	11.95	2.98	6.57
Fe_2B	Tetragonal	1010474	5.09	5.09	4.24
MgO	Cubic	9013224	4.08	4.08	4.08
$B_2MgNi_{6.7}$	Cubic	1510752	10.56	10.56	10.56

Table A.2 The indices for diffraction peaks of the obtained phases in Fe–Ni–B system.

Phase	2θ	h k l	Sample Name
NiO	37.25	(1 1 1)	A1@1, A1@2
	43.29	(2 0 0)	
	62.88	(2 2 0)	
	75.41	(3 1 1)	
	79.41	(2 2 2)	
Ni_2B	25.21	(1 1 0)	A1@1, A1@2
	35.96	(2 0 0)	
	42.54	(0 0 2)	
	45.89	(2 1 1)	
	50.09	(1 1 2)	
	51.77	(2 2 0)	
	56.89	(2 0 2)	
	58.43	(3 1 0)	
	69.16	(2 2 2)	
	71.65	(3 2 1)	
	74.90	(3 1 2)	
	76.25	(4 0 0)	
	80.23	(2 1 3)	
	81.81	(3 3 0)	
	82.86	(4 1 1)	
	87.29	(4 2 0)	
Fe	44.56	(1 1 0)	A1@1, A1@2
	64.85	(2 0 0)	
	82.10	(2 1 1)	
Ni_3B	44.78	(1 1 0)	A2@1, A2@2
	65.19	(2 0 0)	
	82.56	(2 1 1)	
FeB	27.32	(1 1 0)	A2@1, A2@2
	32.56	(0 2 0)	
	37.72	(1 0 1)	

	39.60	(1 2 0)	
	41.26	(1 1 1)	
	44.68	(2 0 0)	
	45.08	(0 2 1)	
	47.80	(2 1 0)	
	50.67	(1 2 1)	
	54.97	(1 3 0)	
	56.37	(2 2 0)	
	57.66	(2 1 1)	
	63.06	(0 0 2)	
	64.07	(1 3 1)	
	65.35	(2 2 1)	
	68.21	(0 4 0)	
	69.06	(2 3 0)	
	70.03	(1 1 2)	
	71.91	(3 1 0)	
	72.61	(1 4 0)	
Fe_2B	24.67	(1 1 0)	A3@1, A3@2,
	27.33	(1 0 1)	A4@1, A4@2
	35.17	(2 0 0)	
	42.61	(0 0 2)	
	45.11	(2 1 1)	
	49.86	(1 1 2)	
	50.59	(2 2 0)	
	56.40	(2 0 2)	
	57.07	(3 1 0)	
	58.45	(3 0 1)	
	68.23	(2 2 2)	
	68.88	(1 0 3)	
	70.08	(3 2 1)	
	73.77	(3 1 2)	
	74.35	(4 0 0)	
	79.72	(3 3 0)	
	79.76	(2 1 3)	
	80.91	(4 1 1)	
	85.00	(4 2 0)	
	89.68	(4 0 2)	
Ni_4B_3	56.99	(5 0 3)	A3@1, A3@2
	57.03	(3 1 3)	
	57.31	(6 1 1)	
	58.22	(2 0 4)	
	60.92	(4 1 3)	
	60.98	(3 0 4)	
	61.12	(7 0 2)	
	62.06	(8 0 0)	
	62.22	(0 2 0)	
	62.77	(6 1 2)	
	63.03	(6 0 3)	
	63.83	(8 0 1)	
	64.36	(2 2 0)	

64.40	(7 1 1)
64.52	(1 2 1)
64.72	(4 0 4)
65.29	(1 1 4)
65.71	(5 1 3)
66.09	(2 2 1)
66.85	(2 1 4)
68.67	(3 2 1)
68.99	(8 0 2)
69.15	(0 2 2)
69.37	(5 0 4)
69.41	(3 1 4)
69.54	(7 1 2)
69.65	(1 2 2)
69.79	(7 0 3)
70.43	(8 1 0)
70.54	(4 2 0)
71.17	(2 2 2)
71.34	(6 1 3)
72.09	(8 1 1)
72.20	(4 2 1)
72.30	(1 0 5)
72.55	(9 0 1)
72.93	(4 1 4)
73.67	(3 2 2)
73.79	(2 0 5)
74.87	(6 0 4)
76.25	(3 0 5)
76.65	(5 2 1)
77.00	(8 1 2)
77.11	(4 2 2)
77.23	(8 0 3)
77.36	(5 1 4)
77.45	(9 0 2)
77.76	(7 1 3)
77.87	(1 2 3)
79.33	(2 2 3)
79.66	(4 0 5)
79.70	(0 1 5)
80.18	(1 1 5)
80.24	(10 0 0)
80.38	(6 2 0)
80.43	(9 1 1)
81.20	(7 0 4)
81.47	(5 2 2)
81.63	(2 1 5)
81.74	(3 2 3)
81.83	(10 0 1)
81.98	(6 2 1)
82.68	(6 1 4)

	83.99	(5 0 5)	
	84.02	(3 1 5)	
	84.98	(8 1 3)	
	85.09	(4 2 3)	
	85.19	(9 1 2)	
	85.42	(9 0 3)	
	86.59	(10 0 2)	
	86.73	(6 2 2)	
	87.36	(4 1 5)	
	87.93	(10 1 0)	
	88.19	(7 2 1)	
	88.37	(8 0 4)	
	88.52	(0 2 4)	
	88.88	(7 1 4)	
	88.99	(1 2 4)	
	89.23	(6 0 5)	
	89.38	(5 2 3)	
	89.44	(0 0 6)	
	89.51	(10 1 1)	
	89.91	(1 0 6)	
MgO	37.56	(1 1 1)	A3@1, A3@2
	43.65	(2 0 0)	
	63.44	(2 2 0)	
	76.12	(3 1 1)	
	80.17	(2 2 2)	
$B_2MgNi_{6.7}$	23.79	(2 2 0)	A4@1, A4@2
	27.98	(3 1 1)	
	29.25	(2 2 2)	
	33.90	(4 0 0)	
	37.05	(3 3 1)	
	38.05	(4 2 0)	
	41.84	(4 2 2)	
	44.51	(5 1 1)	
	48.70	(4 4 0)	
	51.08	(5 3 1)	
	51.86	(6 0 0)	
	54.90	(6 2 0)	
	57.10	(5 3 3)	
	57.82	(6 2 2)	
	60.66	(4 4 4)	
	62.73	(7 1 1)	

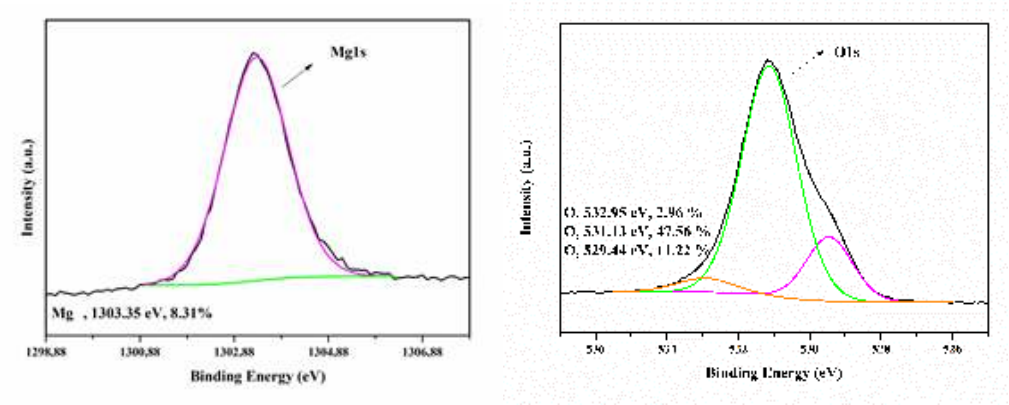

Figure A.4 XPS spectra of Mg1s and O1s for the sample A3@1.

Table A.3 Rate constants obtained for the hydrolysis of $NaBH_4$ for A2@1 at a temperature range of 25–45 °C. (Hydrolysis conditions: 5 mL of 0.2 M $NaBH_4$ containing 10 mmol NaOH in the presence of 20 mg of catalyst).

Temperature (°C)	Time range used to obtain the rate constant (min)	k (mmol ml^{-1} min^{-1})	R^2
25	0–10.0	0.0205	0.9027
30	0–8.5	0.027	0.9924
35	0–7.5	0.0288	0.9517
40	0–5.0	0.0397	0.9774
45	0–3.0	0.0781	0.9972

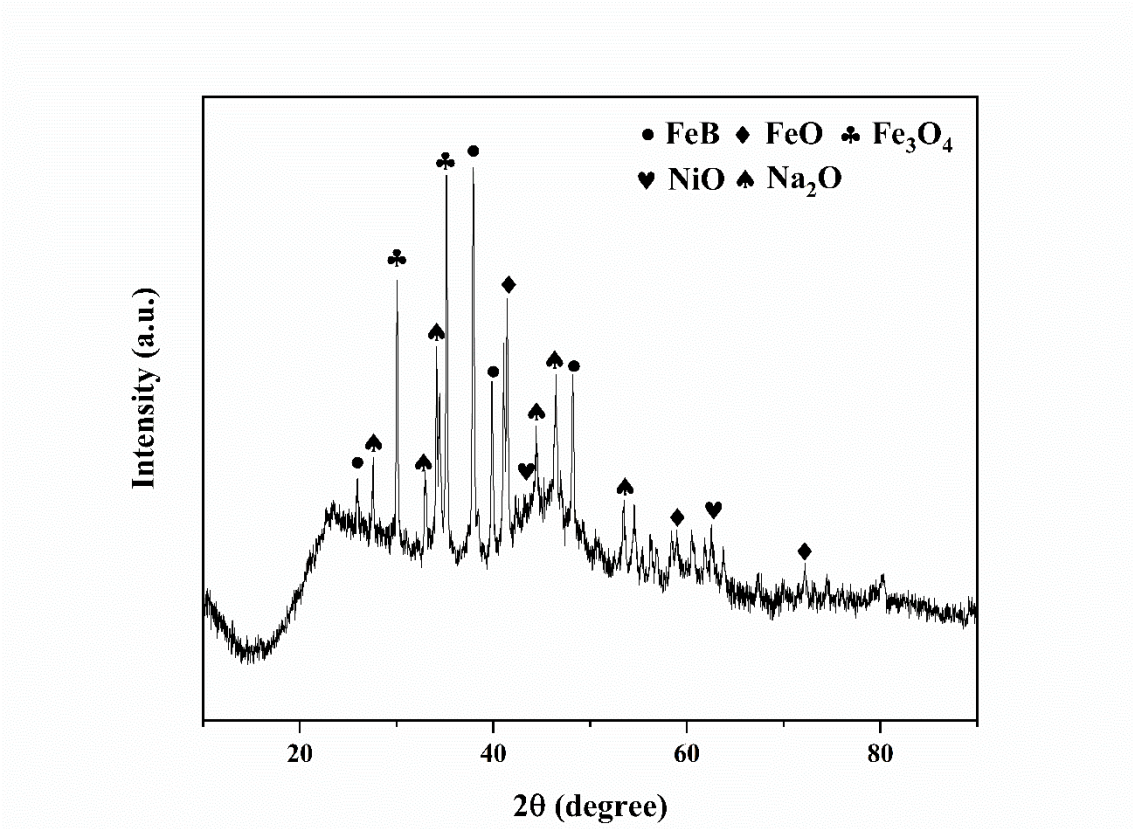

Figure A.5 XRD pattern of the dried A2@1 sample after the fifth cycle of recyclability test.

Table A.4 ICDD Card numbers and theoretical lattice parameters (Å, Angstrom) for the obtained phases.

Phase	Crystal structure	ICDD Card Number	a	b	c
CoB	Orthorhombic	04-003-2122	3.95	5.24	3.04
Co_2B	Tetragonal	00-025-0241	5.01	5.01	4.22
Co_5B_{16}	Orthorhombic	01-082-3072	19.17	2.93	5.49
NiB	Orthorhombic	00-006-0567	2.94	7.38	2.97
Ni_4B_3	Orthorhombic	01-073-2551	11.95	2.98	6.57
Ni_4B_3*	Monoclinic	04-007-1417	6.43	4.88	7.82
$Ni_2(Co_{0.67}B_{0.33})$	Cubic	01-081-3360	11.64	11.64	11.64

Table A.5 The indices for diffraction peaks of the obtained phases in Co–Ni–B system.

Phase	2θ	h k l	Sample Name
CoB	28.273	(1 1 0)	S1@850, S1@900, S2@850, S3@850, S3@900, S4@850, S5@850

	34.175	(0 2 0)	S1@850, S1@900, S4@850, S5@850
	37.325	(1 0 1)	S1@850, S1@900, S3@850, S3@900, S4@850, S5@850
	41.232	(1 1 1)	S1@850, S1@900, S3@850, S3@900, S4@850, S5@850
	45.680	(0 2 1)	S1@850, S1@900, S2@850, S3@850, S3@900, S4@850, S5@850
	49.285	(2 1 0)	S1@850, S1@900, S2@850, S3@850, S3@900, S4@850, S5@850
	51.498	(1 2 1)	S1@850, S1@900, S2@850, S5@850
	57.632	(1 3 0)	S4@850, S5@850
	58.423	(2 1 1)	S1@850, S1@900, S2@850, S3@850, S3@900, S4@850
	60.963	(0 0 2)	S3@850, S3@900, S4@850, S5@850
	76.316	(1 2 2)	S5@850
	79.729	(2 3 1)	S1@850, S1@900, S2@850, S3@850, S3@900, S4@850, S5@850
	82.087	(2 1 2)	S1@850, S1@900, S2@850, S3@850, S3@900, S4@850, S5@850
	88.813	(1 3 2)	S1@900, S2@850, S3@850, S3@900, S4@850, S5@850
NiB	32.902	(1 1 0)	S1@850, S1@900, S2@850, S3@850, S3@900
	38.957	(0 2 1)	S1@850, S1@900, S2@850, S3@850, S3@900
	45.067	(1 1 1)	S1@850, S1@900, S3@850, S3@900
	48.238	(1 3 0)	S1@850, S1@900, S3@850, S3@900
	62.538	(0 0 2)	S1@850, S3@900
$Ni_2Co_{0.67}B_{0.33}$	37.833	(4 2 2)	S2@850
	40.224	(5 1 1)	

	61.102	(5 5 3)	
Co_2B	35.743	(2 0 0)	S1@850
	42.759	(0 0 2)	
	45.715	(2 1 1)	
	56.935	(2 0 2)	
Ni_4B_3	14.810	(2 0 0)	S6@850
	28.152	(1 0 2)	S6@850
	29.876	(4 0 0)	S6@850
	31.043	(2 0 2)	S3@850, S3@900, S4@850, S6@850
	33.834	(1 1 1)	S4@850, S6@850
	35.388	(3 0 2)	S3@850, S3@900, S4@850, S6@850
	36.318	(2 1 1)	S3@850, S4@850, S6@850
	40.163	(3 1 1)	S3@850, S4@850, S6@850
	42.813	(4 1 0)	S6@850
	43.677	(2 1 2)	S3@850, S3@900, S4@850, S6@850
	44.005	(2 0 3)	S3@850, S4@850, S6@850
	45.084	(4 1 1)	S6@850
	47.022	(3 1 2)	S3@900, S4@850, S6@850
	50.852	(5 1 1)	S6@850
	51.422	(4 1 2)	S4@850, S6@850
	52.363	(1 1 3)	S6@850
	55.944	(0 0 4)	S6@850
	60.917	(3 0 4)	S6@850
	62.777	(6 1 2)	S3@850, S3@900, S4@850, S6@850
	64.715	(4 0 4)	S6@850
	70.552	(4 2 0)	S6@850
	74.871	(6 0 4)	S6@850
	77.875	(1 2 3)	S6@850
	80.174	(1 1 5)	S4@850, S6@850
	85.098	(4 2 3)	S6@850
Ni_4B_3*	23.363	(0 0 2)	S6@850
	27.395	(1 1 1)	S6@850
	30.592	($\bar{1}$ 1 2)	S6@850
	32.580	($\bar{2}$ 0 2)	S6@850
	38.726	(0 2 1)	S6@850
	39.663	($\bar{1}$ 1 3)	S6@850
	41.343	(2 0 2)	S6@850
	45.500	(1 1 3)	S6@850
	47.015	($\bar{2}$ 2 1)	S6@850
	51.517	(3 1 1)	S6@850
	56.911	(1 1 4)	S6@850
	58.593	(1 3 0)	S6@850

	59.196	($\bar{1}$ 3 1)	S6@850
	62.301	($\bar{1}$ 1 5)	S6@850
	62.478	($\bar{1}$ 3 2)	S6@850
	64.789	(2 2 3)	S6@850
	67.083	(3 1 3)	S6@850
	70.303	($\bar{3}$ 1 5)	S6@850
	74.959	(2 2 4)	S6@850
	79.510	(0 4 1)	S6@850
	80.142	($\bar{4}$ 2 4)	S6@850
	82.668	(3 3 2)	S6@850
	85.197	($\bar{2}$ 4 1)	S6@850
	85.455	($\bar{2}$ 2 6)	S6@850
Co_5B_{16}	39.555	(4 1 1)	S3@900
	43.429	(6 0 2)	
	51.407	(5 1 2)	

Table A.6 Rate constants obtained for the hydrolysis of $NaBH_4$ for S4@850 at a temperature range of 25–45 °C. (Hydrolysis conditions: 5 mL of 0.2 M $NaBH_4$ containing 10 mmol NaOH in the presence of 20 mg of catalyst)

Temperature (°C)	Time range used to obtain the rate constant (min)	k (mmol ml^{-1} min^{-1})	R^2
25	0–10.0	0.0186	0.9941
30	0–7.5	0.0263	0.9989
35	0–6.0	0.0326	0.9984
40	0–5.0	0.0374	0.9982
45	0–4.5	0.0438	0.9957

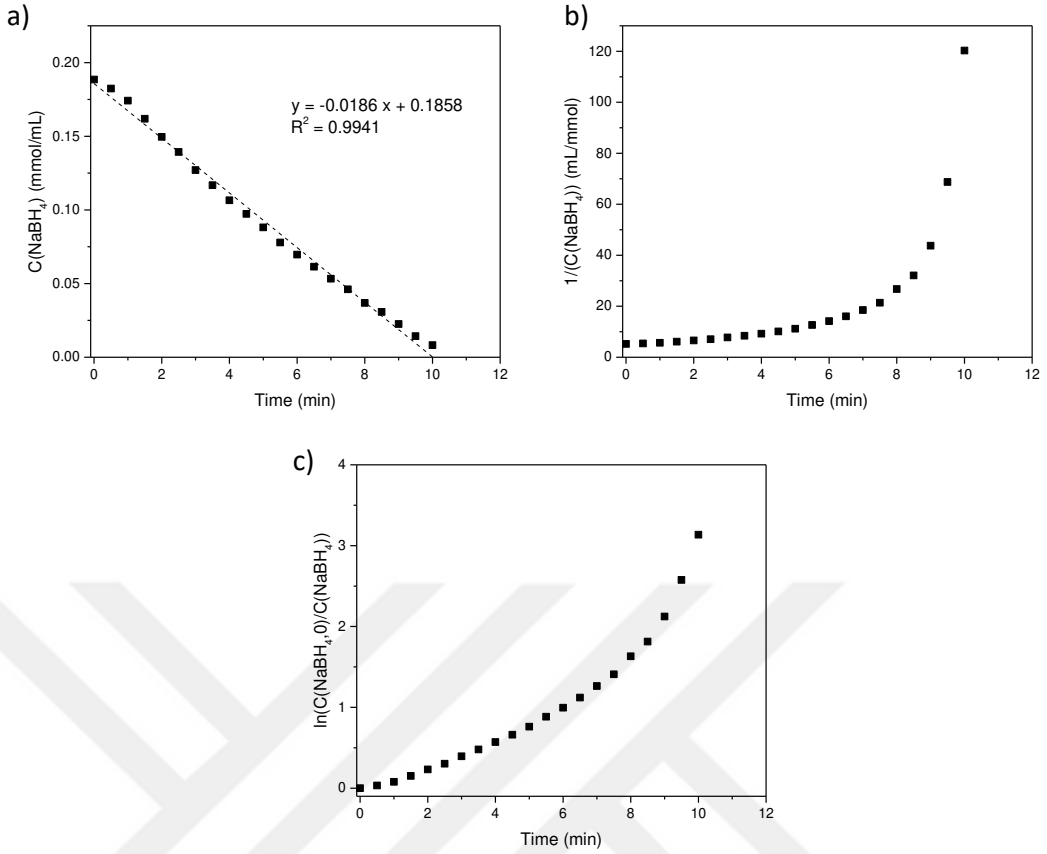

Figure A.6 Determination of the reaction order at 25 °C for S4@850 by investigating the reaction kinetic models for a) zero-order, b) first-order, and c) second-order reactions. (Hydrolysis conditions: 5 mL of 0.2 M $NaBH_4$ containing 10 mmol NaOH in the presence of 20 mg of catalyst).

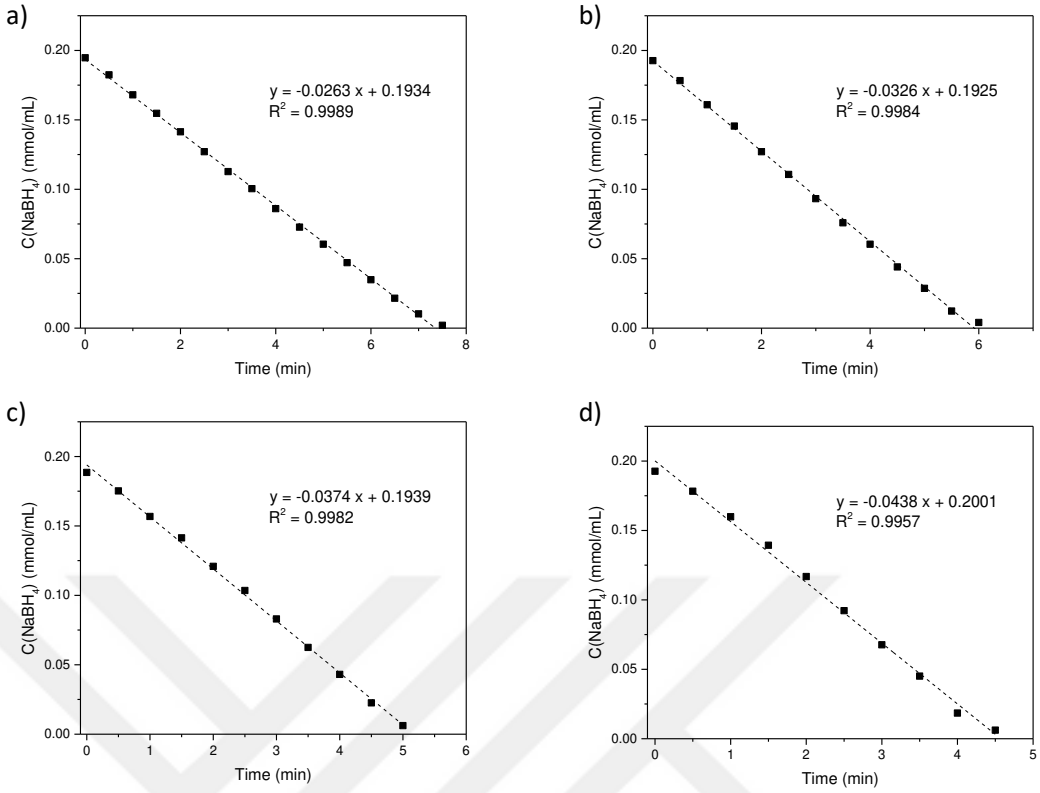

Figure A.7 The zero-order reaction rate plots showing the linear relationship between the concentration of $NaBH_4$ and reaction time for S4@850 at a) 30, b) 35, c) 40, and d) 45 °C. (Hydrolysis conditions: 5 mL of 0.2 M $NaBH_4$ containing 10 mmol NaOH in the presence of 20 mg of catalyst).